

12-2011

## Modeling and Control of a Flexible Ionic Polymer Metal Composite(IPMC) Actuator for Underwater Propulsion

Shivakanth Gutta  
University of Nevada, Las Vegas

Follow this and additional works at: <https://digitalscholarship.unlv.edu/thesesdissertations>



Part of the [Metallurgy Commons](#), [Ocean Engineering Commons](#), and the [Polymer and Organic Materials Commons](#)

---

### Repository Citation

Gutta, Shivakanth, "Modeling and Control of a Flexible Ionic Polymer Metal Composite(IPMC) Actuator for Underwater Propulsion" (2011). *UNLV Theses, Dissertations, Professional Papers, and Capstones*. 1237. <https://digitalscholarship.unlv.edu/thesesdissertations/1237>

This Dissertation is protected by copyright and/or related rights. It has been brought to you by Digital Scholarship@UNLV with permission from the rights-holder(s). You are free to use this Dissertation in any way that is permitted by the copyright and related rights legislation that applies to your use. For other uses you need to obtain permission from the rights-holder(s) directly, unless additional rights are indicated by a Creative Commons license in the record and/or on the work itself.

This Dissertation has been accepted for inclusion in UNLV Theses, Dissertations, Professional Papers, and Capstones by an authorized administrator of Digital Scholarship@UNLV. For more information, please contact [digitalscholarship@unlv.edu](mailto:digitalscholarship@unlv.edu).

Modeling and Control of a Flexible Ionic Polymer Metal Composite(IPMC)

Actuator for Underwater Propulsion

by

Shivakanth Gutta

Master of Science  
Osmania University, India  
2004

A dissertation submitted in partial fulfillment  
of the requirements for the

**Doctor of Philosophy Degree**  
**Department of Mechanical Engineering**  
**College of Engineering**

**Graduate College**  
**University of Nevada, Las Vegas**  
**December 2011**



## **Dissertation Approval**

The Graduate College  
The University of Nevada, Las Vegas

August 8, 2011

This dissertation prepared by

**Shivakanth Gutta**

entitled

**Modeling and Control of a Flexible Ionic Polymer Metal Composite  
(IPMC) Actuator for Underwater Propulsion**

is approved in partial fulfillment of the requirements for the degree of

**Doctor of Philosophy in Mechanical Engineering**

**Dr. Woosoon Yim**  
*Examination Committee Chair*

**Dr. Mohamed B. Trabia**  
*Examination Committee Member*

**Dr. Brendan J. O'Toole**  
*Examination Committee Member*

**Dr. Yitung Chen**  
*Examination Committee Member*

**Dr. Sahjendra N. Singh**  
*Graduate College Faculty Representative*

**Dr. Ronald Smith**  
*Graduate College Dean*

## ABSTRACT

# MODELING AND CONTROL OF A FLEXIBLE IONIC POLYMER METAL COMPOSITE(IPMC) ACTUATOR FOR UNDERWATER PROPULSION

by

Shivakanth Gutta

Woosoon Yim, Examination Committee Chair  
Professor of Mechanical Engineering  
University of Nevada, Las Vegas

The goal of this research is to model and control the underwater vehicle propelled by IPMC actuator. IPMC consists of an ionic membrane sandwiched between two metallic electrodes. When an external voltage is applied, IPMC undergoes large deformation due to transport of ions. Due to its ability to work in aqueous environments, it can be used for developing small scale underwater vehicles.

First, Finite element approach is used to describe the dynamics of the both single and segmented IPMC actuator. In the approach presented, each element is attached with a local coordinate system that undergoes rigid body motion along with the element and the deformation of the element is expressed in local coordinate frame. This large deflection model is combines with Clumped RC model to model the dynamics of the IPMC.

Next, hydrodynamic model for the IPMC driven vehicle is developed. Frictional resistive forces are considered for modeling the interaction with water. The hydrodynamic coefficients are identified using FLUENT CFD analysis. The developed hydrodynamic model is validated using the experimental data. An autonomous IPMC propelled vehicle is developed to overcome the limited applications tethered vehicle developed earlier.

In this research, two kinds of control algorithms based on system identification are developed. A PI controller is designed using simulation data and implemented for controlling speed and orientation of the vehicle. Using the identified linear model, a decoupling control algorithm is developed to eliminate the interactions in tracking speed and orientation (heading angle) of the vehicle. The developed algorithm implemented on original non-linear plant.

A path planning algorithm is presented to control the trajectory of the vehicle in the presence of obstacles. Obstacles are approximated by polygonal shapes that approximate their actual dimensions and the vehicle is approximated by a rectangle that encloses the largest deformation of the oscillating IPMC actuator. To simplify the problem of collision detection, vehicle is shrunk to a line while obstacles are expanded by a half width of the rectangle representing the vehicle. The path generated by the algorithm is discretized with respect to time and controlled simultaneously for the orientation angle and speed of the vehicle.

A model reference adaptive controller (MRAC) is designed for underwater vehicle propelled by the Ionic polymer metal composite (IPMC) actuator. Trajectories of

the vehicle are controlled by simultaneously controlling the bias and amplitude of the sinusoidal voltage applied to the IPMC actuator attached at the rear end of the vehicle. Using Lyapunov stability theory and factorization of the high frequency gain matrix, an adaptive output feedback control is designed for trajectory control of a heading angle and a speed of the vehicle. In the proposed approach, SDU (Square Diagonal and Upper triangular matrix) decomposition of the high frequency gain (HFG) matrix is used. Only signs of the leading principle minors of the HFG matrix are assumed to be known. Simulations results are presented to show that precise trajectory control of the heading and speed is achieved in spite of the coupling between controlled variables.

## ACKNOWLEDGEMENTS

I would like to thank my advisor, Dr. Woosoon Yim for all his help and support in my pursuit of a Doctorate degree. Throughout this process he has provided support and encouragement in my research and my studies. His advice and enthusiasm were critical to the success of this effort. I would also like to thank Dr. Mohamed B. Trabia, Dr. Sahjendra N. Singh and Dr. Yitung Chen for serving on my advisory committee, as well as their help, advice and guidance during my dissertation work.

I would also like to thank Dr. Brenden J. O'Toole for his time in reviewing the prospectus, participation of proposal defense, and counseling of the thesis as the committee member.

I thank Dr. Kwang J. Kim, Chair, Dept. of Mechanical Engineering, UNR for providing IPMC actuators and helping me in gathering required information during my research work. A special thanks to him and his students for their patience to answer my emails. Special thanks to Dr. Joon S. Lee for his suggestions and help.

I would also like to thank my wife, Adityayani Gutta, for her patience, understanding and invaluable support during the process of writing my thesis. Her suggestions and advices have been great help for me.

I would also like to express my heartiest gratitude to my parents for their unconditional support, love, and affection. A special thanks to my friends Venkat Mudupu,

Jagadeep Thota, Bhaskar Gavinolla, Deepak Shankar, Saul Opie, Prashant Reddy, Kumarswamy Karpanan, Nirup Bandaru, Subramanian Ramasamy, Sreenivas Kohir, Srujan Sridharala, Vinod K. Chakka and Hari Kumar for their unrelenting support and motivation throughout this research activity.

The financial support provided by the National Science Foundation (NSF) is thankfully acknowledged.

Finally, I would like to thank Joan Conway, staff of the Mechanical Engineering department, for providing me with all resources for my defence.



## TABLE OF CONTENTS

ABSTRACT .....	iii
ACKNOWLEDGEMENTS .....	vi
LIST OF TABLES .....	xi
LIST OF FIGURES .....	xiv
CHAPTER 1 INTRODUCTION .....	1
1.1 Review of Literature .....	2
1.2 Objective of Research Work .....	7
1.3 Overview of Dissertation .....	8
CHAPTER 2 IPMC ELECTROMECHANICAL MODELING .....	10
2.1 Ionic Polymer Metal Composite Actuator .....	10
2.2 IPMC actuation principle .....	12
2.3 Clumped RC Model .....	13
2.3.1 Relaxation Model .....	15
2.4 Summary .....	18
CHAPTER 3 DYNAMIC MODELING OF THE IPMC ACTUATOR .....	19
3.1 Large deflection modeling .....	19
3.1.1 Finite element modeling .....	21
3.1.2 Energy formulation .....	26
3.2 Electrical Parameter Identification .....	28
3.3 Experimental Results and Comparison with the Proposed Model .....	32
3.4 Model sensitivity study .....	35
3.5 Verification of the proposed model .....	36
3.6 Summary .....	38
CHAPTER 4 HYDRODYNAMIC MODELING OF THE IPMC PROPELLED VE- HICLE .....	41
4.1 Modeling of the IPMC Propelled vehicle .....	41
4.1.1 Finite element modeling .....	42
4.1.2 Energy formulation .....	44
4.2 Vehicle fluid interaction .....	46
4.3 Simulations and Experiments .....	50

4.3.1	Description of the IPMC propelled vehicle . . . . .	50
4.3.2	Identification of hydrodynamic coefficients . . . . .	50
4.3.3	Identification of drag coefficient of vehicle head . . . . .	57
4.3.4	Identification of electrical constants . . . . .	61
4.4	Model validation . . . . .	65
4.5	Autonomous IPMC propelled vehicle . . . . .	66
4.5.1	Design of the vehicle . . . . .	67
4.5.2	Wireless communication and Control . . . . .	68
4.6	Experimental results and comparison with the proposed model . . . .	69
4.7	Summary . . . . .	73
CHAPTER 5 FEEDBACK CONTROL OF IPMC PROPELLED VEHICLE . . . .		74
5.1	Yaw and Speed Control . . . . .	74
5.1.1	Control law . . . . .	75
5.2	Simulation Results . . . . .	81
5.3	Summary . . . . .	81
CHAPTER 6 COMPUTER SIMULATION OF HEADING AND SPEED CON-		
TROL . . . . .		84
6.1	System Identification . . . . .	84
6.1.1	Amplitude and speed model identification . . . . .	85
6.1.2	Bias and speed model identification . . . . .	87
6.1.3	Bias and heading angle model identification . . . . .	88
6.2	Non-interacting closed loop control . . . . .	92
6.3	Simulation Results . . . . .	95
6.4	Proposed experimental setup for validating the designed controller . .	98
6.5	Summary . . . . .	99
CHAPTER 7 PATH PLANNING AND CONTROL . . . . .		101
7.1	Path Planning . . . . .	102
7.1.1	Representation of workspace . . . . .	102
7.1.2	Objective function . . . . .	103
7.2	Illustrative Example . . . . .	107
7.2.1	Path planning . . . . .	107
7.2.2	Tracking control . . . . .	109
7.3	Summary . . . . .	111
CHAPTER 8 MODEL REFERENCE ADAPTIVE CONTROL ALGORITHM . .		114
8.1	Vehicle dynamic model . . . . .	115
8.2	Gain factorization . . . . .	118
8.2.1	LDU decomposition . . . . .	118
8.2.2	SDU decomposition . . . . .	119
8.3	Adaptive control law . . . . .	120
8.4	Simulation results . . . . .	126

8.5 Summary . . . . .	129
CHAPTER 9 CONCLUSIONS . . . . .	130
VITA . . . . .	143

## LIST OF TABLES

3.1	Mechanical Parameters of the IPMC Actuator . . . . .	29
3.2	Moment-Charge Equation Electrical Constants . . . . .	29
3.3	Characteristics of the excitation signal . . . . .	31
3.4	IPMC Electrical Parameters . . . . .	32
3.5	Mechanical Parameters of the IPMC Actuator[1] . . . . .	39
4.1	Vehicle dimensions and parameters . . . . .	52
4.2	IPMC Mechanical Characteristics . . . . .	52
4.3	Identified electrical parameters . . . . .	64
4.4	Autonomous vehicle dimensions and parameters . . . . .	69
7.1	Parameters used in simulation . . . . .	109

## LIST OF FIGURES

2.1	Chemical structure of typical IPMC polymer . . . . .	11
2.2	IPMC actuation principle . . . . .	12
2.3	Clumped R-C model of element $i$ . . . . .	14
3.1	Local coordinate system attached to each element . . . . .	20
3.2	Schematics of IPMC with $n$ -elements . . . . .	21
3.3	Geometric approximation of infinitesimal axial displacement $du$ . . . . .	23
3.4	Definition of local and Global slope angles for three element case . . . . .	25
3.5	Blocking force measurement . . . . .	30
3.6	Blocking force for 4V uniform applied voltage across IPMC . . . . .	30
3.7	Chirp input signal applied to IPMC and measured current . . . . .	31
3.8	Experimental setup for measuring the deflection of IPMC . . . . .	33
3.9	Simulated and Experimental results for IPMC of Table 3.1 when 4 volts are applied uniformly when local reference frame formulation is used . . . . .	33
3.10	Simulation and Experimental results for the IPMC of Table I when 4 volts are applied uniformly without local reference frame formulation[2] . . . . .	34
3.11	Simulated and Experimental results for IPMC tip X-coordinate . . . . .	35
3.12	Simulated and Experimental results for IPMC tip Y-coordinate . . . . .	36
3.13	X-coordinate of the IPMC tip point with respect to time . . . . .	37
3.14	Y-coordinate of the IPMC tip point with respect to time . . . . .	37
3.15	Simulation results of the IPMC of Table 3.5 when input of 2 volts uniformly applied . . . . .	38
3.16	Comparison of simulated tip displacement with that of Fig. 6 in[1] . . . . .	39
4.1	Schematic representation of the IPMC-driven vehicle and coordinate system . . . . .	42
4.2	Hydrodynamic forces acting on the infinitesimal element $ds_i$ of the element $i$ . . . . .	47
4.3	(a)Schematics of the IPMC propelled vehicle. (b) Photo of the IPMC propelled vehicle . . . . .	51
4.4	(a)Physical application of IPMC. (b) two-dimensional computational domain . . . . .	53
4.5	Typical computational domain of IPMC . . . . .	54
4.6	Mesh dependency studies for the drag coefficient . . . . .	55
4.7	Mesh dependency studies for the lift coefficient . . . . .	56
4.8	IPMC configuration and corresponding reference angles . . . . .	57

4.9	Drag coefficient variation with angle of attack . . . . .	58
4.10	Lift coefficient variation with angle of attack . . . . .	58
4.11	Schematic representation of a configuration in bending cycle of IPMC and hydrodynamic friction coefficients . . . . .	59
4.12	Computational domain and geometry of the fish head . . . . .	60
4.13	The computational domain mesh . . . . .	60
4.14	Experimental setup for measuring the drag force on the vehicle head .	62
4.15	Filtered drag force on the vehicle head at $V = 0.01m/sec$ . . . . .	62
4.16	Head drag coefficient variation with respect to speed of the vehicle . .	63
4.17	Step input voltage applied and measured current . . . . .	63
4.18	Measured blocking force . . . . .	64
4.19	IPMC driven vehicle in the tank . . . . .	65
4.20	Comparison of simulated and experimental displacement of the vehicle for 4 and 5 volts sinusoidal inputs . . . . .	66
4.21	Schematics of the IPMC propelled vehicle . . . . .	67
4.22	IPMC propelled vehicle in tank . . . . .	68
4.23	Experimental setup for measuring the position of the IPMC driven vehicle . . . . .	69
4.24	Comparison of simulated and experimental results when sinusoidal input of 6volts applied across IPMC actuator . . . . .	71
4.25	Actuation signal applied to IPMC actuator . . . . .	72
4.26	Experimental and simulated heading angle results . . . . .	72
5.1	Schematic representation of the IPMC driven vehicle . . . . .	75
5.2	Variation of vehicle steady state speed, $v_h$ , with respect to amplitude, A, and bias, B, of voltage input . . . . .	76
5.3	Variation of the steady state speed around the mean value with respect to the change in the input voltage bias . . . . .	77
5.4	(a) Input voltage applied to IPMC ( $V_i$ ) . (b) Change in Yaw angle ( $\Phi_1$ )	77
5.5	Change in vehicle Yaw angle ( $\Phi_1$ ) with respect to input voltage amplitude (A) and bias (B) . . . . .	78
5.6	Relation between steady state speed ( $V_{ref}$ ) and amplitude ( $A_{ss}$ ) . . .	79
5.7	Feedback control of yaw angle and speed of the IPMC driven vehicle .	80
5.8	Simulation results for tracking the yaw angle ( $\phi_1$ ) and speed of the vehicle ( $v_{ref}$ ) . . . . .	82
6.1	Definition of the control input parameters . . . . .	85
6.2	Definition of the output variables . . . . .	86
6.3	Speed of the vehicle with sinusoidal input of 2.5 and 3.5 volts amplitude	87
6.4	Thrust force variation due to bias in the input voltage. . . . .	89
6.5	Change in speed due to bias in input voltage. . . . .	90
6.6	Change in heading angle due to change in bias of input voltage. . . .	91
6.7	Identified plant block diagram . . . . .	92
6.8	Plant with decoupling controller . . . . .	93

6.9	Non-linear plant with decoupling controller . . . . .	96
6.10	Tracking $5e^{-3}$ m/sec speed and $0^\circ$ heading with non-linear dynamic model . . . . .	98
6.11	Tracking $5e^{-3}$ m/sec speed and $10^\circ$ heading with non-linear dynamic model . . . . .	99
6.12	Experimental setup for closed-loop control of IPMC propelled vehicle	100
6.13	Block diagram of closed-loop control of the IPMC propelled vehicle .	100
7.1	Schematics of the vehicle and workspace . . . . .	103
7.2	Schematics of the vehicle search in angular direction at $k^{th}$ time step	104
7.3	Work space used in simulation . . . . .	108
7.4	Path generated by the algorithm . . . . .	110
7.5	Discretized speed and orientation values for the example of Fig. 7.4 .	111
7.6	Comparison of path planning and trajectory control results for the example of Fig. 7.4 . . . . .	112
7.7	Simulation results for following the discretized speed and orientation values for the example of Fig. 7.4 . . . . .	113
8.1	Model reference adaptive control speed (mm/sec) and heading angle (degree) . . . . .	127
8.2	Control input amplitude (v) and bias (v) . . . . .	128
8.3	Estimated parameter norm $\ \Theta\ $ . . . . .	128

## CHAPTER 1

### INTRODUCTION

Ionic Polymer Metal Composite(IPMC) is an electro-active polymer actuator consisting of a perflourinated membrane, typically Nafion, that has been plated on both sides with a conductive metallic electrodes which are usually made up of gold or platinum. When an external voltage is applied, cations inside the membrane carry solvent molecules towards the cathode, which induce bending of the IPMC in the direction of anode. The magnitude of bending is proportional to the voltage applied and large deformations can be generated by applying relatively small voltages. Conversely, mechanical deformation of the material produces a measurable electrical signal. Thus, ionic polymers can be used both as sensors and actuators for applications in motion measurement and control. The advantage of these materials compared to other types of actuators is that, they are materials that operate in a hydrated environment. This has motivated the use of IPMC as biomimetic propulsor.

The advantages of using IPMC materials in such applications are mainly due to their small size, noise free operation and ability to work in aqueous environments. It functions as an embedded actuator that responds to the electrical pulses and generates deformation and forces. These advantages are even more significant in the design of small scale underwater vehicle. In this case, IPMC obsoletes the use of servomo-



tors, hydraulic systems etc. The conventional electrical and hydraulic actuators used in the development of the underwater vehicles occupy considerable volume which otherwise can be used for embedding additional electronic components and increase the functionality of the vehicle.

The goal of this research is to develop small scale underwater vehicle using IPMC as actuator. The vehicle possesses the capability to be remotely controlled and transmit the data collected in proposed application such as underwater monitoring, pipe inspection etc.

## 1.1 Review of Literature

Previous electro-mechanical modeling efforts for ionic polymer materials can generally be separated into empirical models or models based on first principles. Models of electromechanical impedance were developed for the purpose of relating applied voltage to current [3]. Early work on these materials utilized a linear model of actuation to estimate the relationship between applied field and mechanical deformation [4]. Both of these models utilized curve fits of experimental data to model electromechanical coupling. Two port electromechanical model [5] that accounted for both sensing and actuation within the material. This model was also based on curve fits of experimental data. Models based on first principles have also been developed in [6] through [7]. These models are based on the interaction of electrostatic and hydraulic forces within the polymer membrane. Modeling strategy adopted in [8, 9] places more emphasis on the electrostatic interaction while the models by [10, 7, 8] are based on

the relationship between solvent flux and pressure gradients.

Various researchers developed models to describe the deformation of IPMCs. The first trend is to use a continuous model. The work of [6] is one of the earliest efforts in this area. The proposed model, which describes the bending response of water-saturated IPMC in air, is more suited for small deformations. Several researchers developed models along this line. The following is a survey of recent efforts in developing continuous models. The model used in [11] is based on a linear electromechanical coupling. This model has functional similarity to the equivalent circuit models of piezoelectric elements. An experimental method for estimating the general time-dependent elastic moduli of IPMCs is proposed in [12]. This experimental procedure is combined with a viscoelastic model. The modeling scheme of [13] is able to model nonuniform large deformations of IPMCs but fails to address the dynamic behavior of the actuator. The distributed model proposed in [14] describes the nonuniform bending of the IPMC by finding the curvature of any point along the length of the IPMC. This model, however, did not consider the mechanical parameters of the IPMC. The model of [15] is open to model reduction and control design while capturing the basic physics of the IPMC. These models work for orthogonal boundaries only. The authors of [16] produced a model for describing the behavior of IPMC actuators immersed in viscous fluids. This model uses the concepts of electromechanical transduction and hydrodynamic function. The dynamic models proposed in the works reviewed above are limited to the cases of limited bending of a single-segment uniform IPMC.

Finite element models have the advantage of describing the behavior of actuators

with various discontinuities. The following is a review of most relevant works in this area. Lee et al[17] used commercial software to model a cantilever-type IPMC. Since the software used did not support the electromechanical coupling analysis, a thermal analogy technique was used to simulate the electromechanical coupling effect in the finite element model. A two-dimensional finite element formulation based on the Galerkin method was conducted for the basic field equations governing the response of IPMC beams with two pairs of electrodes[18]. A three dimensional finite element analysis modeled the deformation of IPMC beams due to water redistribution in the beams associated with the electrochemical response. Yim et al[2] presented a first attempt to approach this problem using a finite element modeling approach to describe the dynamics of a segmented IPMC based on the large deflection beam theory. In this work, a model that accommodates large deformation of IPMCs is used to describe the motion of the actuator. However, this model is restricted by its inability to accurately describe the large deflection of the IPMC due to its coordinate system not considering rigid body rotation of each element. Pugal et al[19, 1] used continuum mechanics equations to describe the three-dimensional bending of the IPMC actuators. This model also includes the mass transfer and the electrostatic effects in the base polymer (Nafion). However, the exclusion of nonlinear terms in the kinematic equations restricts the model to be used only during the small deformation case of the IPMC. Commercial finite element analysis software was used to investigate the actuation performance as well as the natural frequencies of the IPMC diaphragm and the flap valve of a micropump[20]. With the exception of[2] the discussion of the

dynamics of an IPMC undergoing large deformations is missing.

Lately, there is a significant increase in modeling and development of Autonomous underwater vehicles (AUVs) due to potential applications such as surveillance, search and rescue and underwater inspection[21, 22]. Over millions of years of evolution, aquatic creatures such as fishes, eels etc have achieved optimized body designs, increasing the swimming efficiency and maneuverability. This inspired the development of Biologically-inspired (or Biomimetic) Autonomous Underwater Vehicles (BAUV). Study conducted on real fishes by Sfakiotakis *et.al*[23] offers key design ideas to develop BAUV. Waving plate theory and elongated body theories developed in[24, 25] provide classical approach of fish swimming mechanics. Dynamic model of the oscillating foil for planar propulsion is discussed in[26], where, optimal spring constants are found to reduce energy consumption in driving the foil. In[27, 28], an experimental setup is built to study the carangiform locomotion and compared with the hydrodynamic model of the carangiform. The maneuvering control of an aquatic vehicle using oscillating foil propulsion is discussed in[29]. The system is non-minimum phase and under actuated with four degrees of freedom and two actuators. Therefore, trajectory of the vehicle is controlled by offline motion planning and online feedback tracking. Because of using traditional actuator systems such as servos and hydraulics, BAUVs discussed above are big and noisy. This lead to the interest in developing small scale autonomous vehicles which can operate quietly and consume less power.

In recent years, there has been increase in the number of small scale underwater water vehicles, which use IPMC actuators for propulsion[30, 31, 32], and this can

be attributed to the fact that IPMC actuators are noise-free unlike conventional propulsion systems and the driving voltage is relatively small[33, 34]. The compact nature of the autonomous vehicles driven by IPMC actuator can be extremely useful in applications like pipe inspection and underwater sampling etc[35, 36]. Zhang et al.[37] developed a fish-like micro robot that can swim, walk and float using IPMC actuators. The use of these vehicles can be further improved provided that they can maneuver efficiently through obstacles. The following is a brief survey of research in this area. Domenici and Blake[38] reviewed the kinematics of escape responses and feeding strikes of a fish. Shin et al.[39] proposed an algorithm for obstacle detection based on simplified models of obstacles of a robotic fish. Neuro-fuzzy inferences were used to recognize the features of an obstacle to avoid collision. Chao et al.[40] developed a miniature robotic fish propelled by oscillating caudal fin driven by servo. They used infrared sensors to implement online obstacle detection and photosensitive sensors for light source searching. Yu et al.[41] developed an algorithm to achieve different turning gaits for a multi-link fish-like robot. This idea was further incorporated in an algorithm for obstacle avoidance[42].

A well designed control algorithm is inevitable for successful tracking of the reference trajectory. In [43, 44], a model reference adaptive controller was designed to control the position of the IPMC during underwater application. Using MRAC, successful tracking was achieved in the presence of parametric uncertainties and environmental conditions affecting the performance of the IPMC actuator. In [45] adaptive controller has been derived for control of MIMO submersible system using adaptive

back stepping design approach. In order to avoid singularity in the control law during the adaptation process, SDU decomposition of the high frequency gain matrix has been used[45]. But, for the synthesis of the control law, all the state variables must be measured. However, the synthesis of the controllers using fewer sensors is extremely important from the practical point of view.

## 1.2 Objective of Research Work

This research work focuses on the development and control of miniature biomimetic underwater vehicle propelled by Ionic Polymer Metal Composite(IPMC) actuator. Small size, low operating voltage and large deformation capabilities provide the additional advantages of minimizing the size of the vehicle, where the traditional actuating systems like servos, hydraulics and pneumatics are not used.

The specific objectives of this research work are:

- to model the large deformation bending of the IPMC actuator.
- to model the dynamics of IPMC propelled vehicle.
- to develop the IPMC propelled vehicle and validate the hydrodynamic model.
- to design control algorithm and to implement in closed loop control of the IPMC driven vehicle.

### 1.3 Overview of Dissertation

This dissertation is organized as follows to present the details of IPMC dynamic modeling, hydrodynamic modeling of IPMC propelled vehicle and experimental validation, design of control algorithm and development of autonomous IPMC propelled vehicle.

Chapter 2 provides an introduction to the IPMc actuator followed by electro-mechanical modeling of the actuator.

Chapter 3 presents the large deflection bending model of the IPMC actuator. Finite element modeling and energy formulation are used for modeling the dynamics of the actuator. Simulation results are validated using experimental data.

Chapter 4 discusses the hydrodynamic modeling of the vehicle driven by IPMC actuator. Hydrodynamic coefficients are identified using FLUENT CFD analysis and validated using experimental data.

Chapter 5 presents the feedback control of the vehicle using system identification procedure.

Chapter 6 provides decoupling control algorithm for controlling the speed and heading of the IPMc propelled vehicle. The controller transfer functions are obtained using desired closed loop transfer functions.

Chapter 7 presents the path planning for the IPMC driven vehicle in the presence of obstacles approximated by polygonal shapes. The path generate by path planning algorithm is discretized with respect to time and controlled using the feedback controller developed in chapter 5.

Chapter 8 presents the model reference adaptive control of speed and heading of the IPMC driven vehicle. It is assumed that the system parameters as well as high frequency gain matrix are unknown. Using Lyapunov stability theory and factorization of the high frequency gain matrix, an adaptive output feedback control is designed for trajectory control of a heading angle and a speed of the vehicle.



## CHAPTER 2

### IPMC ELECTROMECHANICAL MODELING

In this chapter, modeling of the electromechanical coupling in IPMC is discussed. Relation between voltage applied to the IPMC and the moment generated due to transport of ions is discussed. RC representation of the IPMC is combined with first order bending moment model to describe electromechanical coupling. The dynamic model of the IPMC is developed by combining the clumped RC model with large deflection bending model to be discussed in Chapter 3

#### 2.1 Ionic Polymer Metal Composite Actuator

Ionic polymer metallic composite (IPMC) is a class of the electro active polymers that have shown potential for practical applications. This Ionic actuator is electro-less plated electro active polymer (EAP) material that bends when subjected to voltage across its thickness. Ionic actuator has several attractive EAP characteristics that include:

- Low drive voltage is from 1.0 -5.0 V
- Soft material ( $E = 2.2 \times 10^8$  Pa)
- Possible to miniaturize ( $\leq 1\text{mm}$ )

- Can be activated in water or in a wet condition.

IPMC actuators show large deformation in the presence of low applied voltage and exhibit low impedance. They operate best in a humid environment and can be made as self-contained encapsulated actuators to operate in dry environments as well. They provide an attractive means of actuation as artificial muscles for biomechanics and biomimetics applications. The IPMC actuator used in our investigation is composed of a per fluorinated ion exchange membrane (IEM), which is chemically composed with a noble metal such as gold or platinum. A typical chemical structure of one of the ionic polymers used in our research is shown in Fig. 2.1. Where  $n$  is such that

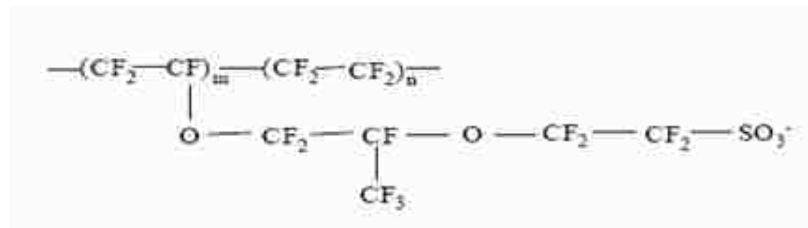


Figure 2.1: Chemical structure of typical IPMC polymer

$5 < n < 11$  and  $m \sim 1$ , and  $M^+$  is the counter ion ( $H^+$ ,  $Li^+$  or  $Na^+$ ). One of the interesting properties of this material is its ability to absorb large amounts of polar solvents, i.e. water. Platinum, Pt, metal ions, which are dispersed through out the hydrophilic regions of the polymer, are subsequently reduced to the corresponding

metal atoms. This results in the formation of a dendritic type electrode. When the polymer is hydrated, the positively charged ions associated with the  $SO_3^-$  groups become mobile, allowing the polymer to conduct cations. This ion mobility is believed to be directly responsible for the electromechanical transduction in ionic polymer transducers. The discussion of the early history of these materials and their use as biomimetic transducers is referred in[46].

## 2.2 IPMC actuation principle

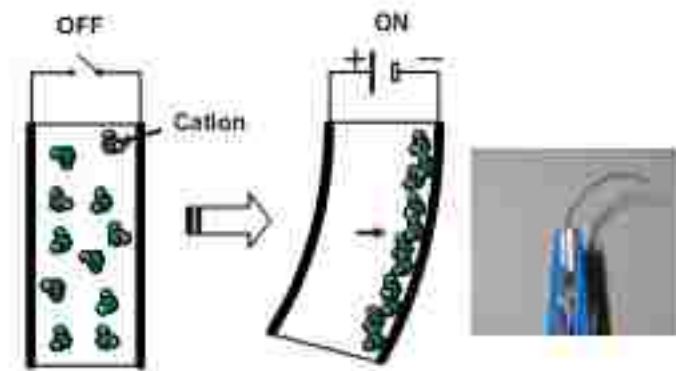


Figure 2.2: IPMC actuation principle

The theory for actuation of the Ionic Polymer Metal Composite (IPMC) is attributed to the unique nature of the base polymer membrane for the IPMC, the ionomer. The ionomer is specially designed and synthesized to selectively allow dif-

fusion of mobile cations as well as solvent (typically polar solvents, such as water, through nano size pores and channels of the polymer matrix while the anions that are covalently bonded to the fixed polymer matrix). The basic actuation principle is illustrated in Fig. 2.2. By applying an electric field to neutral IPMC, a solvent flux of hydrated cations as well as free water is created with direction towards the cathode. It is this solvent flux that creates an electro-osmotic pressure differential resulting in a bending motion towards the anode side of the IPMC.

### 2.3 Clumped RC Model

The clumped RC model relates the input voltage applied to the Ionic actuator strip to the charge. It has been shown that the IPMC often exhibits a slow relaxation towards cathode after a quick bending towards anode. From the description of IPMC in section 2.1, the Ionic actuator has two parallel electrodes and electrolyte between the electrodes. Double-layer capacitors are formed at the interfaces of two electrodes and the electrolyte. The electrolyte between the electrodes may introduce as internal resistance. This series circuit of C-R-C can be simplified to R-C circuit as shown in Fig. 2.3[2, 47].

The relation between the voltage,  $V_i$ , electric charge,  $Q_i$ , the Capacitance  $C_i$  and current  $I_i$  of an element  $i$  can be represented as

$$\frac{Q_i}{V_i} = \frac{C}{R_1 C s + 1} \quad (2.1)$$

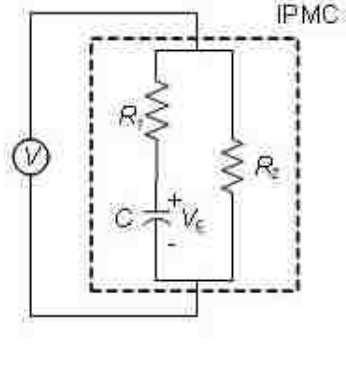


Figure 2.3: Clumped R-C model of element  $i$

$$\frac{I_i}{V_i} = \frac{C(R_1 + R_2)s + 1}{R_1 R_2 C s + R_2} \quad (2.2)$$

where  $s$  is a Laplace variable.

Under a step input voltage, the IPMC strip shows a bending towards anode due to cation migration towards cathode in the polymer network. The bending moment  $u_i$  generated due to applied voltage to element  $i$  is modeled using a first order model as

$$\frac{u_i}{Q_i} = \frac{K_{u_i}}{\tau_{u_i} s + 1} \quad (2.3)$$

where,  $K_{u_i} = K/p$  and  $\tau_{u_i} = 1/p$  are the gain and time constant of element  $i$  respectively.  $K_{u_i}$  and  $\tau_{u_i}$  characterize the speed of bending moment generated from freshly

moving charge across the thickness of the IPMC.

The RC model can be combined with a bending moment model to form the following linear model that relates the input voltage  $V_i$  and bending moment  $u_i$  of element  $i$  as,

$$\frac{u_i}{V_i} = \frac{K_{u_i} C_i}{\tau_{Q_i} \tau_{u_i} s^2 + (\tau_{Q_i} + \tau_{u_i}) s + 1} = \frac{b_{i0}}{s^2 + a_{i1} s + a_{i0}} \quad (2.4)$$

where,  $\tau_{Q_i} = R_1 C$  and  $b_{ij}$ ,  $a_{ij}$  are determined from the experimental data and appropriate system identification toolbox.

### 2.3.1 Relaxation Model

Studies indicate that the response of the Ionic actuator strongly depends on its backbone polymer and ionic content [1, 2], especially the counter ion. And counter ions can be divided to two categories based on the cation size.

- Small cation such as Li+, Na+ and K+.
- Large cation such as alkyl ammonium ions.

The Ionic actuator with small cation has quick response to the applied voltage and slow back relaxation. The Ionic actuator with large cation responds slowly to applied voltage but with no relaxation. It is believed that the small cations move easier over the polymer backbone. The fast movement of the cations towards cathode together with associated water molecules results in an initial quick bending toward to the anode. This response is followed with a relaxation that may be caused by water leakage resulting from a high pressure layer near the cathode toward to the anode

through channels in the polymer backbone. The relaxation process stops when water equilibrium is established. On the contrary, large cations migrate significantly slower and present slow reaction to the electric field. Thus, there no relaxation for Ionic actuator with large cations.

Since Ionic actuator with small cations under a step input voltage shows a slow relaxation towards cathode after a quick bending towards anode, this phenomenon was considered and modeled by adding one zero to Equation 2.3 that relates the charge  $Q_i$  and the bending moment  $u_i$  by a lead network, given by:

$$\frac{u_i}{Q_i} = K_{u_i} \frac{\tau_{u_{i2}}s + 1}{\tau_{u_i}s + 1} \quad (2.5)$$

where,  $\tau_{u_{i2}}$  is a relaxation time constant and the magnitude of  $1/\tau_{u_{i2}}$  reflects the bending effects of the charge in the equilibrium state. Considering the fact that the bending effect due to freshly moving charge is larger than the one in the equilibrium state, the magnitude of  $\tau_{u_{i2}}$  is larger than  $\tau_{u_i}$ . Therefore, Equation 2.4 can be further generalized to include relaxation phenomenon and represented as:

$$\frac{u_i}{V_i} = \frac{K_{u_i} C_i (\tau_{u_{i2}}s + 1)}{\tau_{Q_i} \tau_{u_i} s^2 + (\tau_{Q_i} + \tau_{u_i})s + 1} = \frac{b_{i1}s + b_{i0}}{s^2 + a_{i1}s + a_{i0}} \quad (2.6)$$

Considering the IPMC of  $n$  elements, Equation 2.6 can be represented in a state-space form as

$$\ddot{u}_i + a_{i1}\dot{u}_i + a_{i0}u_i = b_{i1}\dot{V}_i + b_{i0}V_i, \quad i = \dots n \quad (2.7)$$

By introducing two new state variables,  $Z_{i1}$  and  $Z_{i2}$  for element  $i$ , Equation 2.4 can be written as

$$\frac{u_i}{V_i} = \frac{(b_{i1}s + b_{i0})z_{i1}}{(s^2 + a_{i1}s + a_{i0})z_{i1}} \quad (2.8)$$

and

$$\begin{aligned} \dot{z}_{i1} &= z_{i2} \\ \dot{z}_{i2} &= -a_{i1}z_{i2} - a_{i0}z_{i1} + V_i \end{aligned} \quad (2.9)$$

Using Equation 2.8,  $u_i$  can be expressed in terms of new variables  $z_{i1}$  and  $z_{i2}$  as

$$\dot{u}_i = b_{i0}z_{i1} + b_{i1}z_{i2}, \quad i = 1 \cdots n \quad (2.10)$$

Equation 2.9 can be expressed for entire IPMC of  $n$  elements as

$$\begin{aligned} \dot{Z} &= \begin{bmatrix} 0_{n \times n} & & & I_{n \times n} & & \\ -a_{10} & 0 & 0 & -a_{11} & 0 & 0 \\ 0 & \ddots & 0 & 0 & \ddots & 0 \\ 0 & 0 & -a_{n0} & 0 & 0 & -a_{n1} \end{bmatrix} Z + \begin{bmatrix} 0_{n \times n} \\ I_{n \times n} \end{bmatrix} V \\ &\equiv A_z Z + B_v V \end{aligned} \quad (2.11)$$

where,  $Z = \{z_{11} \ z_{21} \ \cdots \ z_{n1}, \ z_{12} \ z_{22} \ \cdots \ z_{n2}\}^T \in \mathfrak{R}^{2n}$  and  $V = \{V_1 \ V_2 \ \cdots \ V_n\}^T \in \mathfrak{R}^n$  is an input voltage vector. Equation 2.10 can also be expanded



for the input voltage vector  $u$  using  $Z$  as

$$u = \begin{Bmatrix} u_1 \\ \vdots \\ u_n \end{Bmatrix} = \begin{bmatrix} b_{10} & 0 & 0 & b_{11} & 0 & 0 \\ 0 & \ddots & 0 & 0 & \ddots & 0 \\ 0 & 0 & b_{n0} & 0 & 0 & b_{n1} \end{bmatrix} Z \equiv B_u Z \quad (2.12)$$

Using Equation 2.11 and 2.12, the relation between the bending moment,  $u$  generated due to the voltage,  $V$  applied to  $n$  segment IPMC can be expressed in state-space form as:

$$\begin{aligned} \dot{Z} &= A_z Z + B_v V \\ u &= B_u Z \end{aligned} \quad (2.13)$$

State-space representation of electro-mechanical coupling is extremely useful in designing closed loop control algorithm for segmented IPMC actuator.

## 2.4 Summary

In this chapter, electro-mechanical coupling of the IPMC is modeled using RC circuit. This model also incorporates the relaxation phenomenon seen in most of the IPMCs. Relation between the applied voltage and bending moment is obtained by combining induced charge and bending moment equations. State-space representation of the electro-mechanical model is derived and can be used for controller implementation.

## CHAPTER 3

### DYNAMIC MODELING OF THE IPMC ACTUATOR

In this chapter, a variation of the large deflection beam bending theory and RC model[48, 47] are combined to develop the dynamic model of the IPMC actuator. First, the equations governing dynamics of beam bending under applied moment are developed using the finite element method and energy formulation. This model is integrated with the lumped RC model of chapter 2 to establish a relation between applied voltage and beam deflection of the IPMC. The electrical parameters used in the developing electro-mechanical model are identified using the experimental data.

#### 3.1 Large deflection modeling

In this section, a dynamic model for the IPMC undergoing large deformation is discussed. Finite element approach is used to describe the dynamics of the both single and segmented IPMC actuator, which considered to be composed of finite elements satisfying Euler-Bernoulli's theorem. Energy approach is used to formulate the equations of motion. The bending moment applied to each segment is determined from the RC electrical model developed in chapter 2.

Figure 3.1 shows an  $n$ -segment actuator consisting of Nafion (Ionomeric polymer) passive substrate layer of thickness  $h_b$  where two layers of metallic electrode (Gold)

of thickness  $h_g$  are placed on both sides. The electrodes for each segment are wired independently from the others and by selectively activating each segment, varying curvature along the length may be obtained. The magnitude of curvature can be controlled by adjusting the voltage level applied across each segment. By controlling the curvature of the actuator along the length, it is possible to use this actuator for various robotic applications. In the following analysis of the IPMC, axial extensional and shearing deformations are not considered. These assumptions can be justified considering the geometry of the IPMC and the types of loading they are subjected to.

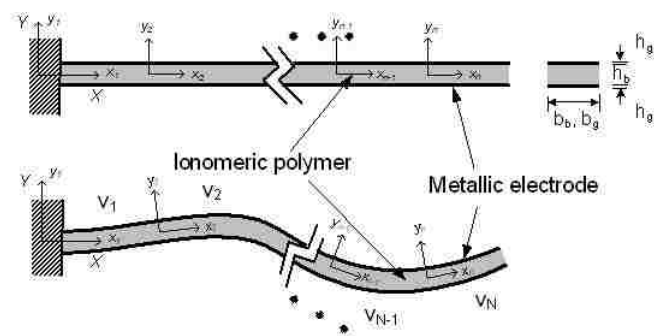


Figure 3.1: Local coordinate system attached to each element

### 3.1.1 Finite element modeling

The analysis in this section is based on the assumption that the IPMC is composed of  $n$  elements as shown in Fig. 3.1 and Fig. 3.2. An element  $i$  is bounded between two node  $i$  and node  $i+1$ . This element is described using a local coordinate frame,  $i$ , which is fixed at node  $i$ . This frame has the same orientation as slope of node  $i$ . The displacement of any point along the neutral axis of element  $i$  is described in terms of the local nodal displacements and slopes of nodes  $i$  and  $i+1$ . Nodes  $i$  and  $i+1$  are labeled 1 and 2 in the remainder of this section to simplify the equations. The lateral displacement at a distance  $x_i$  on element expressed in the local coordinate frame  $i$  becomes:

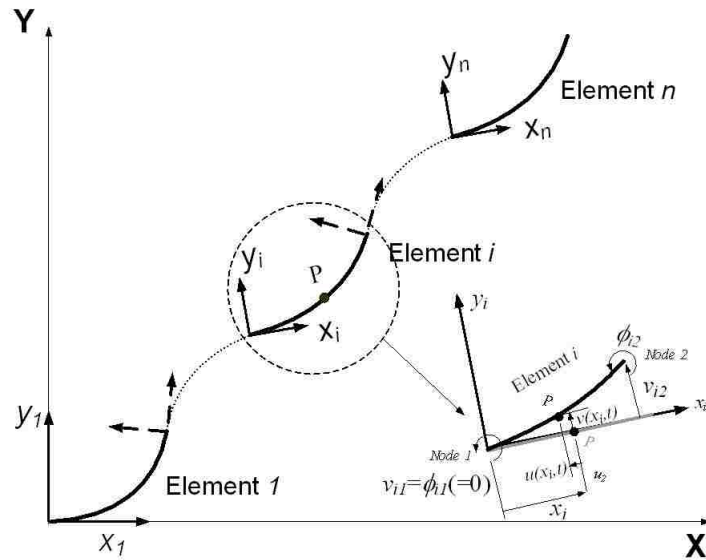


Figure 3.2: Schematics of IPMC with n-elements

$$v_i(x_i, t) = N(x_i)q_i(t) \quad (3.1)$$

where,  $N$  is a row vector consisting of  $N = [N_1(x_i) \ N_2(x_i) \ N_3(x_i) \ N_4(x_i)]$ , and  $q_i(t) = [v_{i1}(t) \ \phi_{i1}(t) \ v_{i2}(t) \ \phi_{i2}(t)]$  where  $v_{i1}(= 0)$  and  $\phi_{i1}(= 0)$  denote nodal displacement and slopes of the first node of element  $i$ , and  $v_{i2}$  and  $\phi_{i2}$  denote nodal displacement and slope of the second node in the local coordinate system as shown in Fig. 3.2.  $N$  is a row vector with shape functions  $N_i(x)$  defined as [49].

$$\begin{aligned} N_1 &= \frac{2x^2 - 3x^2L_i + L_i^3}{L_i^3} \\ N_2 &= \frac{x^3L_i - 2x^2L_i^2 + xL_i^3}{L_i^3} \\ N_3 &= \frac{-2x^3 + 3x^3L_i}{L_i^3} \\ N_4 &= \frac{x^3L_i - x^2L_i^2}{L_i^3} \end{aligned} \quad (3.2)$$

Generally, an IPMC do not experience axial loadings. Therefore, any axial deformation is caused by the lateral deformation. As shown in Fig. 3.3, an infinitesimal deformation  $du$  in the opposite axial direction can be expressed as,  $du = -(ds - dx)$  where,  $ds$  is the length of a differential element that can be approximated as,

$$ds = \sqrt{(dv)^2 + (dx)^2} \quad (3.3)$$

Noticing that  $du = -(ds - dx)$  and using Equation 3.3,  $du/dx$  can be expressed as:

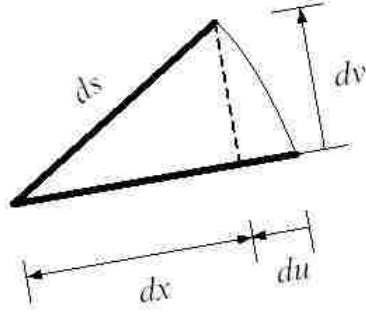


Figure 3.3: Geometric approximation of infinitesimal axial displacement  $du$

$$\frac{du}{dx} = 1 - \sqrt{\left(\frac{dv}{dx}\right)^2 + 1} \quad (3.4)$$

Noticing that  $(a + 1)^g \approx ga + 1$  if  $a$  is small enough, Equation 3.4 simplifies to:

$$\frac{du}{dx} = -\frac{1}{2}\left(\frac{dv}{dx}\right)^2 \quad (3.5)$$

Integrating Equation 3.5 and substituting Equation 3.1, an axial deformation at a distance  $x_i$  of the element  $i$  can be expressed as:

$$\begin{aligned} u_i(x_i, t) &= -\frac{1}{2} \int_0^{x_i} \left(\frac{dv(x_i, t)}{dx}\right)^2 dx \\ &= q_i^T \left[-\frac{1}{2} \int_0^{x_i} N'(x)^T N'(x) dx\right] q_i \\ &= q_i^T N_s(x_i) q_i \end{aligned} \quad (3.6)$$

where,  $N'(x) = \frac{dN(x)}{dx}$ .  $N_s(x_i)$  is a  $4 \times 4$  matrix, which is defined as,

$$N_s(x_i) = -\frac{1}{2} \int_0^{x_i} N'(x)^T N'(x) dx \quad (3.7)$$

The axial displacement at node 2 of element  $i$  can be expressed as,

$$\begin{aligned} u_{i2}(t) &= u_i(L_i, t) \\ &= q_i^T \left[ -\frac{1}{2} \int_0^{L_i} N'(x)^T N'(x) dx \right] q_i \\ &= q_i^T N_s(L_i) q_i \end{aligned} \quad (3.8)$$

using Equation 3.8, the position vector of any point  $P$  at a distance  $x_i$  on the element  $i$  in the global reference frame is expressed as,  ${}^i r_p$ ,

$$\begin{aligned} {}^i r_p &= \sum_{j=1}^{i-1} \left[ T_{\Phi_j} \begin{Bmatrix} L_j + q_j^T N_s(L_j) q_j \\ N(L_j) q_j(t) \end{Bmatrix} \right] + T_{\Phi_i} \begin{Bmatrix} x_i + q_i^T N_s(x_i) q_i \\ N(x_i) q_i(t) \end{Bmatrix} \\ i &= 1 \cdots n \end{aligned} \quad (3.9)$$

where,

$$\begin{aligned} T_{\Phi_i} &= \begin{bmatrix} \cos \Phi_i & -\sin \Phi_i \\ \sin \Phi_i & \cos \Phi_i \end{bmatrix} \\ \Phi_i &= \sum_{k=1}^{i-1} \phi_{k2}, \quad i = 2 \cdots n \quad \text{and} \quad \Phi_1 = 0 \end{aligned} \quad (3.10)$$

and  $L_j$  is the length of each element. It should be noted that  $\phi_{k2}$  is the slope angle of the node 2 of the element  $k$  in its local coordinate, and  $i$  is the node 2 slope angle of element  $(i-1)$  in the global frame defined at the node 1 of the element 1 as shown

in Fig. 3.4. Differentiating Equation 3.9 with respect to time, the velocity of a point P can be expressed as follows:

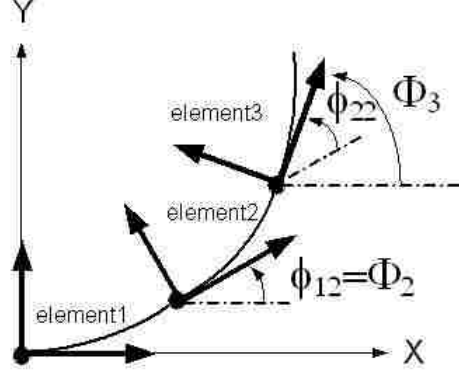


Figure 3.4: Definition of local and Global slope angles for three element case

$$\begin{aligned}
 {}^i \dot{r}_p &= \sum_{j=1}^{i-1} \left[ \dot{T}_{\Phi_j} \begin{Bmatrix} L_j + q_j^T N_s(L_j) q_j \\ N(L_j) q_j(t) \end{Bmatrix} + T_{\Phi_j} \begin{Bmatrix} 2q_j^T N_s(L_j) \dot{q}_j \\ N(L_j) \dot{q}_j(t) \end{Bmatrix} \right] \\
 &+ \dot{T}_{\Phi_i} \begin{Bmatrix} x_i + q_i^T N_s(x_i) q_i \\ N(x_i) q_i(t) \end{Bmatrix} + T_{\Phi_i} \begin{Bmatrix} 2q_i^T N_s(x_i) \dot{q}_i \\ N(x_i) \dot{q}_i(t) \end{Bmatrix} \quad (3.11) \\
 &\triangleq P_i \dot{\xi}_i
 \end{aligned}$$

where,

$$\dot{T}_{\Phi_j} = \sum_{k=1}^{j-1} \frac{\partial T_{\Phi_j}}{\partial \phi_{k2}} \dot{\phi}_{k2} \quad (3.12)$$

$P_i \in \mathfrak{R}^{2 \times 4i}$  and  $\dot{\xi}_i = [q_1^T \ \cdots \ q_i^T] \in \mathfrak{R}^{4i}$  which is defined by nodal vectors  $\dot{q}_i$  for each element.



### 3.1.2 Energy formulation

Based on the results of the previous section and using Equation 3.11, the kinetic energy of  $i^{th}$  element can be expressed as,

$$T_i = \frac{\rho}{2} \int \dot{r}_p^{Ti} \dot{r}_p dx_i = \frac{\rho}{2} \dot{\xi}_i^T \left( \int P_i^T P_i dx_i \right) \dot{\xi}_i = \frac{1}{2} \dot{\xi}_i^T M_i \dot{\xi}_i \quad (3.13)$$

where,  $M_i = \rho \int P_i^T P_i dx_i \in \mathfrak{R}^{4i \times 4i}$  is a mass matrix for  $i^{th}$  element and  $\rho$  is a combined density of the IPMC per unit length. The potential energy of the element  $i$  including the bending moment,  $u_i$ , induced by an externally applied voltage, can be expressed as:

$$U_i = \frac{1}{2} \int_0^{L_i} \frac{1}{EI} \left( EI \frac{\partial^2 v(x_i, t)}{\partial x_i^2} + u_i \right)^2 dx_i \quad (3.14)$$

where  $v(x_i, t)$  is the deflection at point P on element  $i$  in the local frame and  $EI$  is the product of Young's modulus of elasticity by the cross-sectional area moment of inertia. Therefore, the stiffness matrix,  $K_i$ , of the element  $i$  is defined as:

$$K_i = EI \int_0^{L_i} \left[ \frac{\partial^2 N(x_i)}{\partial x_i^2} \right]^T \left[ \frac{\partial^2 N(x_i)}{\partial x_i^2} \right] dx_i \quad (3.15)$$

Unlike the kinetic energy term shown in Equation 3.13, the potential energy of the element  $i$  depends only on its own nodal coordinates,  $q_i(t)$ . Both  $M_i$  and  $K_i$  need to be expanded to the entire length of the actuator with  $n$  elements. These expanded

matrices become

$$M_{ei} = \begin{bmatrix} M_i & 0_{4i \times 4(n-1)} \\ 0_{4(n-i) \times 4i} & 0_{4(n-i) \times 4(n-i)} \end{bmatrix} \in \mathfrak{R}^{4n \times 4n} \quad (3.16)$$

$$K_{ei} = \begin{bmatrix} 0_{4(i-1) \times 4(i-1)} & 0_{4(i-1) \times 4i} & 0_{4(i-1) \times 4(n-i)} \\ 0_{4i \times 4(i-1)} & K_i & 0_{4i \times 4(n-i)} \\ 0_{4(n-i) \times 4(i-1)} & 0_{4(n-i) \times 4i} & 0_{4(n-i) \times 4(n-i)} \end{bmatrix} \in \mathfrak{R}^{4n \times 4n} \quad (3.17)$$

Using the Lagrangian dynamics, the equations of motion for an element  $i$  can be determined as,

$$M_{ei}\ddot{\xi}_i + K_{ei}\xi_i = B_{ei}u_i(t) \quad (i = 1 \cdots n) \quad (3.18)$$

where,  $B_{ei} = [0_{4(i-1)} \ 0 \ 0 \ 0 \ 1 \ 0_{4(n-1)}]^T \in \mathfrak{R}^{4n}$  is a control input vector for the bending moment applied at the second node of the element as the first node is fixed in the local coordinate frame. It should be noted that the nodal coordinates corresponding to node 1 of each element, i.e.,  $(v_{11}, \phi_{11}, v_{21}, \phi_{21}, \cdots, v_{n2}, \phi_{n2})$  are eliminated from the generalized coordinate,  $\xi_i$ , due to zero boundary conditions in the local coordinate frame. Therefore, the reduced form of the generalized coordinate,  $\xi_e$  is expressed as  $\xi_e = [v_{12} \ \phi_{12} \ v_{22} \ \phi_{22} \ \cdots \ v_{n2} \ \phi_{n2}]^T \in \mathfrak{R}^{2n}$ . Equation 3.18 can be assembled for the entire  $n$  segments using the reduced coordinate,  $\xi_e$  and represented as:

$$M_e\ddot{\xi}_e + K_e\xi_e = B_e u \quad (3.19)$$

where,  $u = [u_1 \ u_2 \ \cdots \ u_n] \in \mathfrak{R}^n$  is moment applied to  $n$  elements,  $M_e = \sum_{i=1}^n M_{ei}^* \in \mathfrak{R}^{2n \times 2n}$ ,  $K_e = \sum_{i=1}^n K_{ei}^* \in \mathfrak{R}^{2n \times 2n}$  and  $M_{ei}^*$  and  $K_{ei}^*$  are reduced form of  $M_{ei}$  and  $K_{ei}$ , respectively.  $u \in \mathfrak{R}^n$  is an input moment vector and  $B_e \in \mathfrak{R}^{2n \times n}$  is an input control matrix for  $u$  in the reduced form of  $[B_{e1}^* \ \cdots \ B_{en}^*]$ .

The dynamics model of the IPMC actuator undergoing large deformation due to voltage  $V = \{V_1 \ V_2 \ \cdots \ V_n\}^T \in \mathfrak{R}^n$  applied across  $n$  elements is obtained by combining large deformation bending model of the IPMC given in Equation 3.19 with the electrical model given by Equations 2.11 and 2.12. The combined dynamic equation can be written in state-space form as,

$$\begin{aligned}
M_e \ddot{\xi}_i + K_e \xi_i &= B_e u \\
&= B_e B_u Z \\
\dot{Z} &= A_z Z + B_v V
\end{aligned} \tag{3.20}$$

In Equation 3.20, the electrical constants used for modeling electro-mechanical coupling are identified using the experimental data. The identification procedure is discussed in next section.

### 3.2 Electrical Parameter Identification

The first step in the identification process is to identify the constants relating the induced charge to the bending moment as described in Equation 2.3. For this purpose, an experiment is done using an IPMC of length  $L$  and measuring the blocking force at its tip,  $f$ . The moment,  $u$ , generated due to the charge is related to the blocking

Table 3.1: Mechanical Parameters of the IPMC Actuator

Variable	Value
$\rho_p$ (density of electrode(Au)[53], $\frac{Kg}{m^3}$ )	19300
$\rho_g$ (density of Nafion)[53], $\frac{Kg}{m^3}$ )	2600
$L$ (length of the IPMC actuator, m)	0.045
$b$ (width of the IPMC actuator, m)	0.005
$h_b$ (thickness of Nafion), m)	0.00028
$h_g$ (thickness of electrode(Au)), m)	0.000002
$E_b$ (Young's modulus of elasticity for Nafion, Pa)	$5e^7$
$E_g$ (Young's modulus of elasticity for electrode (Au)[53],Pa)	$71e^9$

Table 3.2: Moment-Charge Equation Electrical Constants

Variable	Value
$\tau_u$ , sec	2.371
$K_u$ , N/C	$3.6e^{-04}$

force,  $f$ , using the following equation [50, 51].

$$u = \frac{2L}{3}f \quad (3.21)$$

As shown in the Fig. 3.5, the blocking force is measured by positioning a force transducer at the tip of a 4.5 cm IPMC actuator. Mechanical parameters of the IPMC used in the experiments are given Table 3.1. The measured blocking force for a 4 volts uniformly applied voltage is shown in Fig. 3.6. MATLAB System Identification Toolbox (V 7.4.0),[52], is used to determine the values of  $\tau_u$  and  $K_u$  as shown in Table 3.2.

Similarly, MATLAB System Identification Toolbox (V 7.4.0),[52], is used to iden-

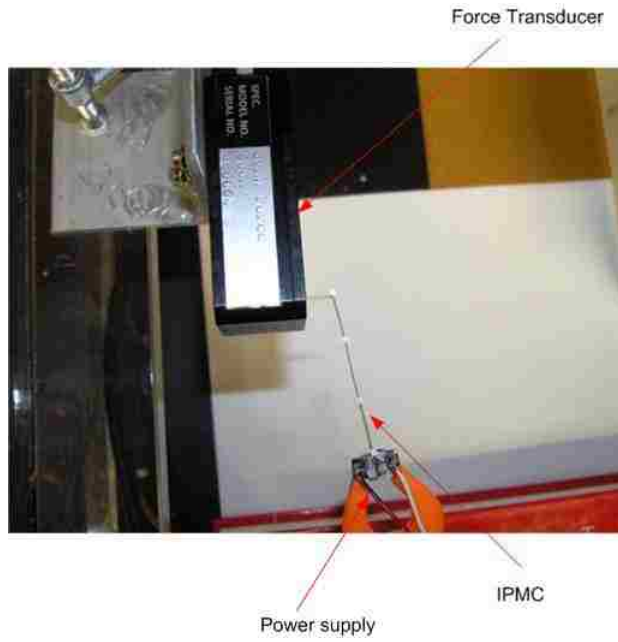


Figure 3.5: Blocking force measurement

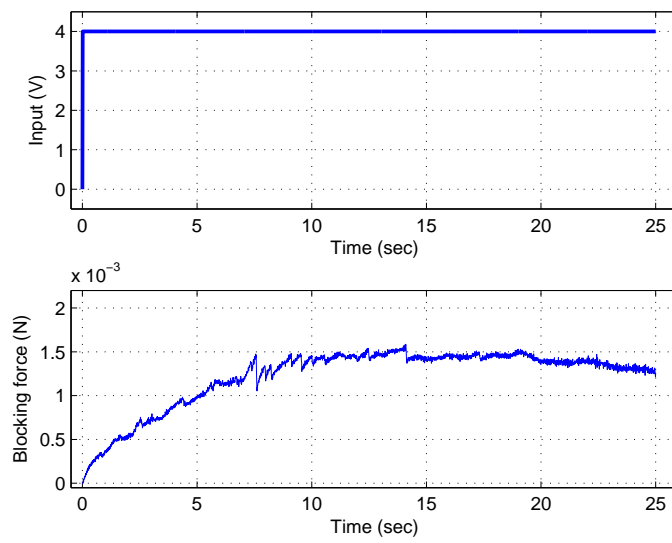


Figure 3.6: Blocking force for 4V uniformly applied voltage across IPMC

tify the constants of the RC electrical model. The following chirp input signal defined by Equation 3.22 and Table 3.3 is applied to the IPMC. The measured current is

Table 3.3: Characteristics of the excitation signal

Variable	Value
$A$ (amplitude, Volt)	750
$f_0$ (initial frequency, Hz)	0.01
$f_1$ (target frequency, Hz)	10
$T$ (target time, sec)	1000

shown in the Fig. 3.7. The electrical parameters obtained from system identification procedure are shown in Table 3.4.

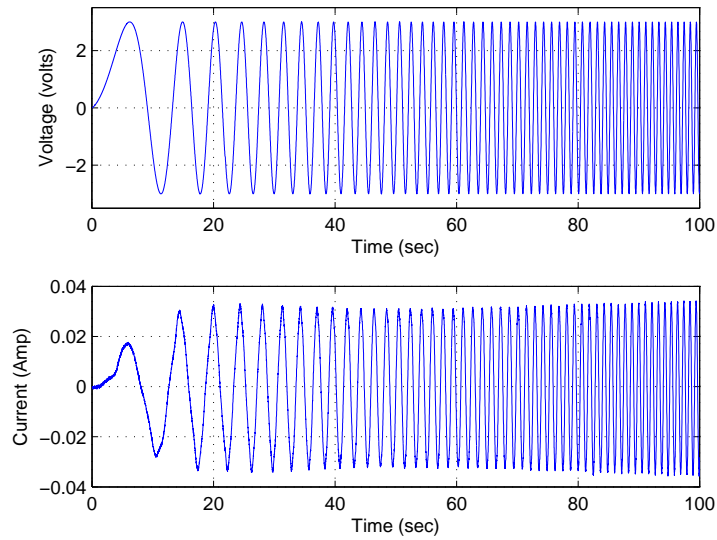


Figure 3.7: Chirp input signal applied to IPMC and measured current

$$y = A \sin(2\pi(f(t))t) \quad (3.22)$$

Table 3.4: IPMC Electrical Parameters

Variable	Value
$R_2, \Omega$	78
$C, \text{F}$	$1.382e^{-2}$
$\tau_Q(= RC), \text{sec}$	0.0106

where

$$f(t) = f_0 + \left(\frac{f_1 - f_0}{T}\right) t$$

### 3.3 Experimental Results and Comparison with the Proposed Model

Computer simulations and experimental results are presented to assess the performance of the proposed modeling approach. Table 3.1 lists the mechanical parameters of the IPMC, which is completely fixed at (0, 0) and is aligned with the positive *x-axis*. All experiments were conducted at room temperature 22.1°C with relative humidity of 19.3%.

To validate the proposed model, experiment is done using the setup shown in the Fig. 3.8. The inputs and outputs of the system are controlled and monitored using a LabVIEW program. The control signals generated by the SCB-68 I/O board are amplified using the bi-polar amplifier. A video capturing system (2 frames/sec) is used to record the position of IPMC by tracing the selected four equally spaced points on its edge.

The same experiment is simulated using the proposed model and four equal-length

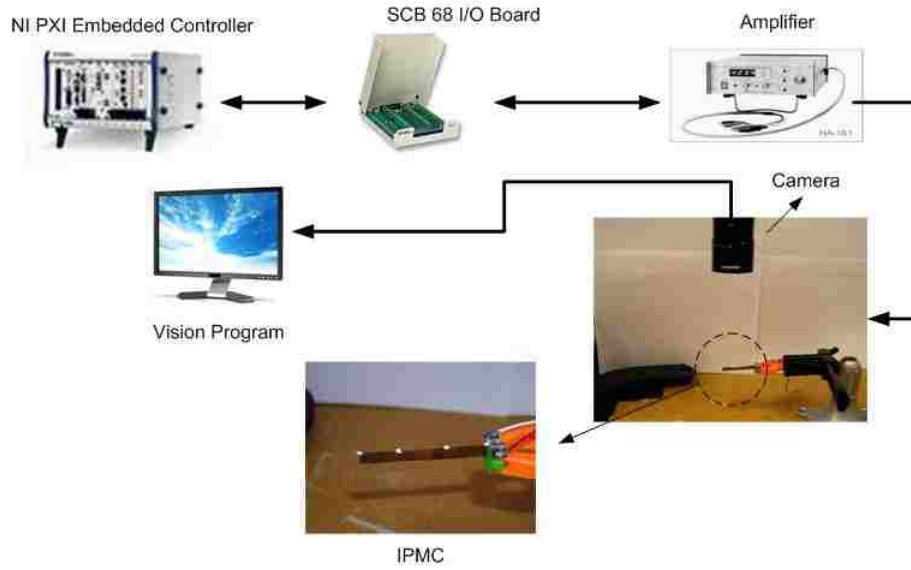


Figure 3.8: Experimental setup for measuring the deflection of IPMC

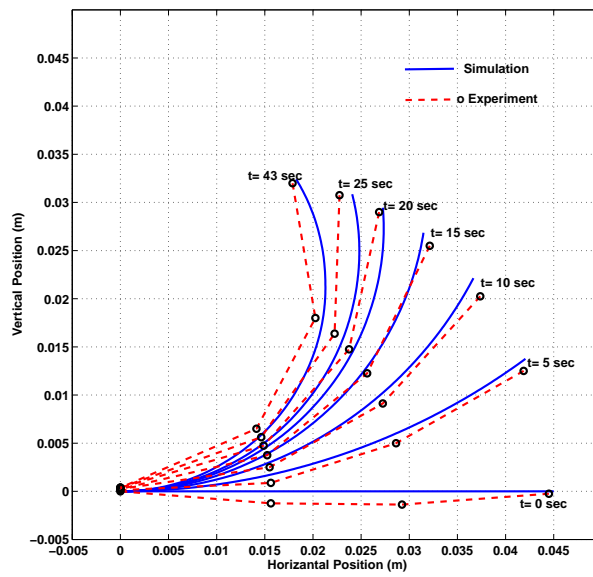


Figure 3.9: Simulated and Experimental results for IPMC of Table 3.1 when 4 volts are applied uniformly when local reference frame formulation is used

elements. Fig. 3.9 shows a comparison between simulation and experimental results of the IPMC deflection when a 4-volt uniform signal is applied. Results show a close



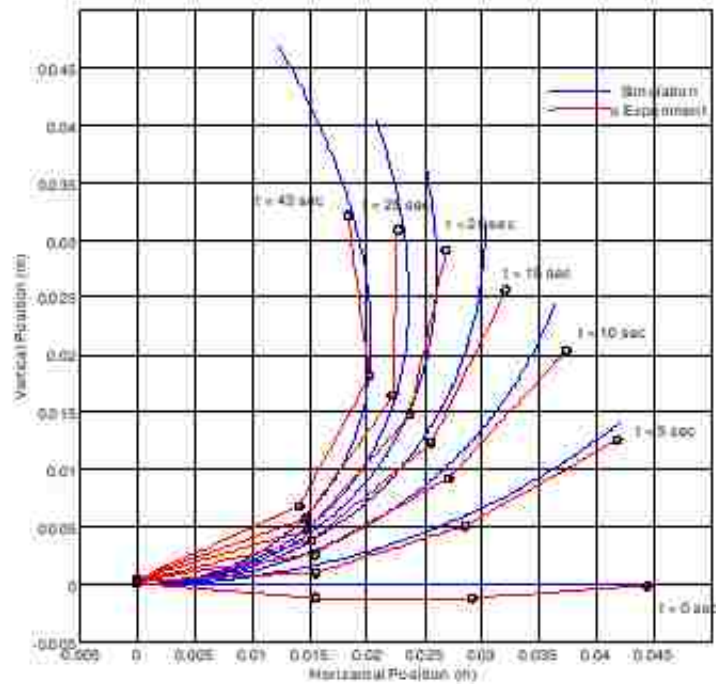


Figure 3.10: Simulation and Experimental results for the IPMC of Table I when 4 volts are applied uniformly without local reference frame formulation[2]

matching between the proposed model and experimental data. It is useful to compare these results with those in Fig. 3.10, which show the deflection of the same IPMC without local reference frame formulation[2]. This model results in an undesirable extension of elements, especially as time progresses.

Figure 3.11 and 3.12 show the simulation and experimental results of the IPMC tip X, Y coordinates respectively. It can be observed that the results of the proposed model are close to experimental results, especially in the first 20 seconds. Some deviation is experienced in the X direction, which may be due to simplification of the

axial deformation.

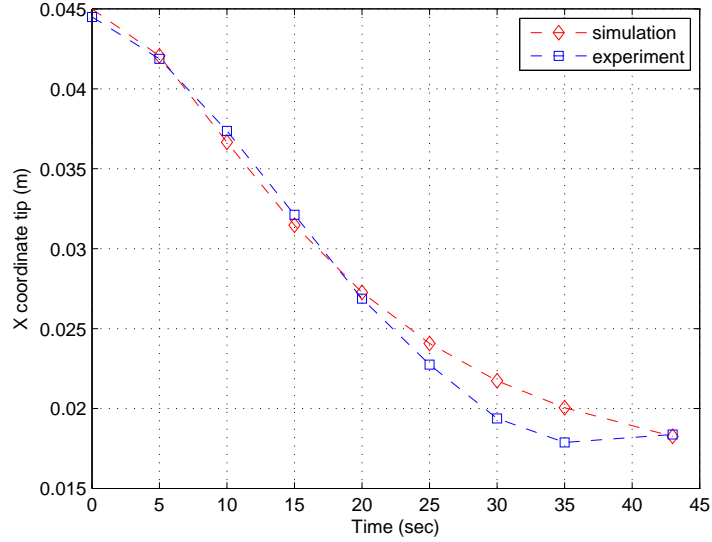


Figure 3.11: Simulated and Experimental results for IPMC tip X-coordinate

### 3.4 Model sensitivity study

This section addresses the sensitivity of the proposed model to the number of elements used in finite element formulation. Three cases are considered with number of elements,  $n = 2, 3$  and  $4$ . Fig. 3.13 and Fig. 3.14 show the tip position of the IPMC of Table 3.1 with respect to time. It is apparent that the results converge as the number of elements increase. Results also show that using four elements instead of three does not contribute significantly to the accuracy of the solution while increasing computational load by approximately six times. It is therefore recommended to use

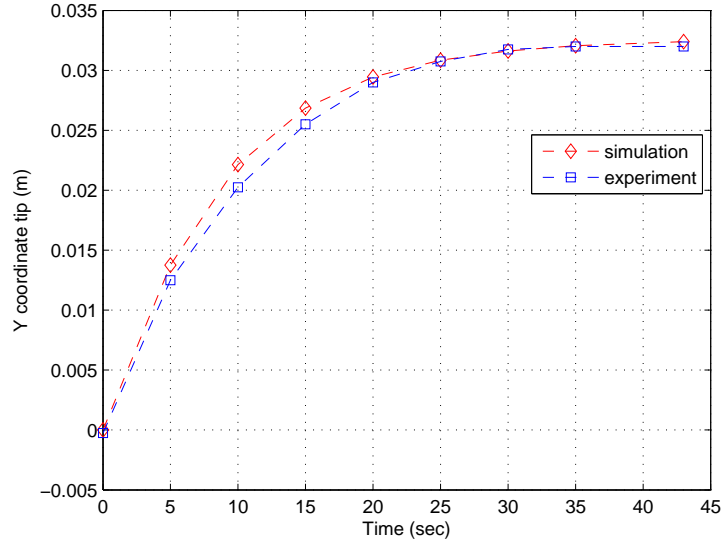


Figure 3.12: Simulated and Experimental results for IPMC tip Y-coordinate

three elements when modeling an IPMC of comparable dimensions and characteristics.

### 3.5 Verification of the proposed model

To evaluate the performance of the proposed model, simulations are conducted using the mechanical and electrical parameters taken from [1]. The significant parameters affecting the electromechanical coupling of the IPMC are capacitance,  $C$ , and time constant  $\tau_u$ , of the Equations 2.1 and 2.3 respectively. The capacitance is given as  $3.8e-05$  F/m and the time constant  $\tau_u = 0.05$  sec, is found from the tip displacement and time curve as shown in Fig. 6 of [1]. The mechanical parameters of the IPMC taken from [1] are given in Table 3.5. The width of IPMC,  $b$ , is assumed to be 0.004 m. Figure 3.15 shows the simulation results when input of 2 volts uniformly

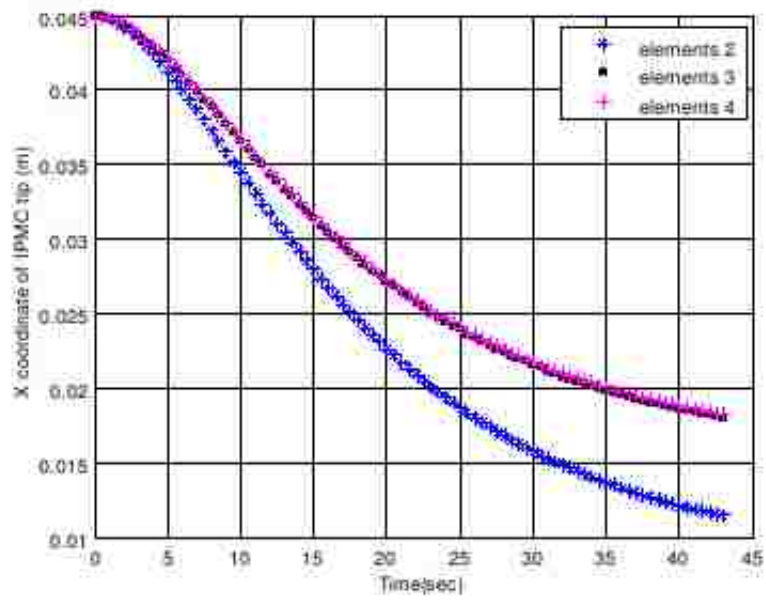


Figure 3.13: X-coordinate of the IPMC tip point with respect to time

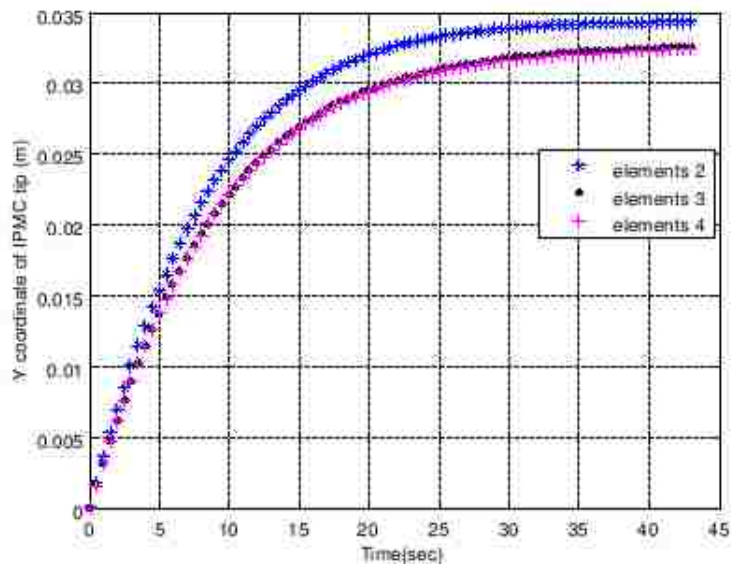


Figure 3.14: Y-coordinate of the IPMC tip point with respect to time

applied across the length of the IPMC. Four elements were used in this case. In comparison with Fig. 5 of [1], X displacement is clearly seen in Fig. 3.15, which is the result of approximating horizontal displacement using Eqn. 3.8. The local coordinate frame approach used in this model reduces the error induced due to approximation. Figure 3.16 shows the comparison of simulated tip displacement with that of Fig. 6 in [1].

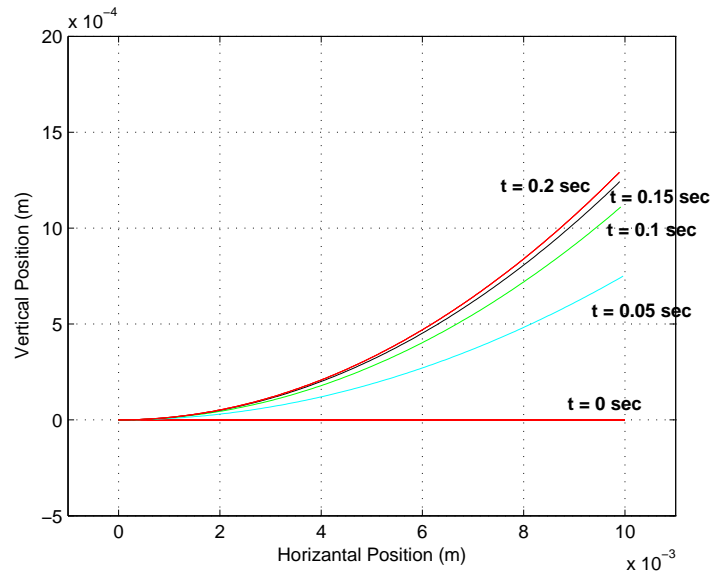


Figure 3.15: Simulation results of the IPMC of Table 3.5 when input of 2 volts uniformly applied

### 3.6 Summary

In this chapter, a novel finite element modeling technique for deriving the dynamic model of an IPMC actuator is proposed. In the proposed approach, each element has

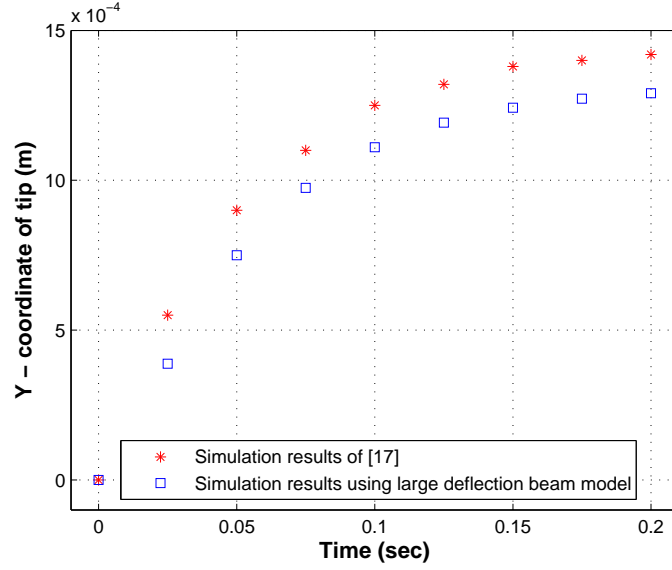


Figure 3.16: Comparison of simulated tip displacement with that of Fig. 6 in[1]

Table 3.5: Mechanical Parameters of the IPMC Actuator[1]

Variable	Value
$\rho_p$ (density of electrode(Pt)[53], $\frac{Kg}{m^3}$ )	21500
$\rho_g$ (density of Nafion)[53], $\frac{Kg}{m^3}$ )	2600
$L$ (length of the IPMC actuator, m)	0.01
$b$ (width of the IPMC actuator, m)	0.004
$h_b$ (thickness of Nafion), m)	0.00020
$h_g$ (thickness of electrode(Pt)), m)	0.000007
$E_b$ (Young's modulus of elasticity for Nafion, Pa)	$5e^7$
$E_g$ (Young's modulus of elasticity for electrode (Pt)[53],Pa)	$169e^9$

a local coordinate frame attached to its first node. Instead of using the traditional modeling approach which does not have local coordinate frames fixed at each element, the proposed approach has local frames aligned along the tangential direction of node 1 at each element. according to the rotation of the first node. All kinematic formulations are performed in this local frame and eventually expressed in terms of

a global one. Due to the localized description of each element, axial motion of the element due to large rotations can be described more accurately. RC model developed in chapter 2 is combined with the finite element method to formulate the dynamic equations of IPMC. Results of the simulation are compared with the corresponding experimental results. Electrical characteristics of the IPMC used in the simulation are determined experimentally. Comparison between simulation and experimental results shows the accuracy of the proposed approach. This model is also compared to an earlier one[2] to show its advantages. Sensitivity of the proposed model to the number of elements is also discussed. It is shown that using three elements is sufficient to adequately describe the dynamics of the IPMC considered in this study.

## CHAPTER 4

### HYDRODYNAMIC MODELING OF THE IPMC PROPELLED VEHICLE

In this chapter, a finite element-based dynamic model is developed for a miniature underwater vehicle propelled by Ionic Polymer Metal Composite (IPMC) actuator. The large deflection beam model developed in chapter 3, combined with electro-mechanical model of chapter 2 is used to describe the deformation of the IPMC in water. Hydrodynamic forces including frictional effects are also considered. The hydrodynamic force coefficients are identified based on the results of extensive computational fluid dynamics (CFD) simulations and validated using experimental data.

#### 4.1 Modeling of the IPMC Propelled vehicle

In this section, analytical model describing the dynamics of the IPMC-propelled underwater vehicle is developed. We utilize the large deflection beam model presented in chapter 3 to describe the dynamics of the IPMC deflection. First, dynamic equations of the vehicle are developed using the finite element method and energy formulation, and combined with the hydrodynamic model to describe the fluid interaction with the actuator.



### 4.1.1 Finite element modeling

The vehicle is attached to an IPMC as shown in the Fig. 4.1. The IPMC is divided into several elements and each has a local coordinate system attached to it. This coordinate system undergoes the rigid body motion along with the element. Using Equations 3.1 through 3.8, the position vector of any point  $P$  on an element  $i$  is described in terms of nodal displacements and slopes as:

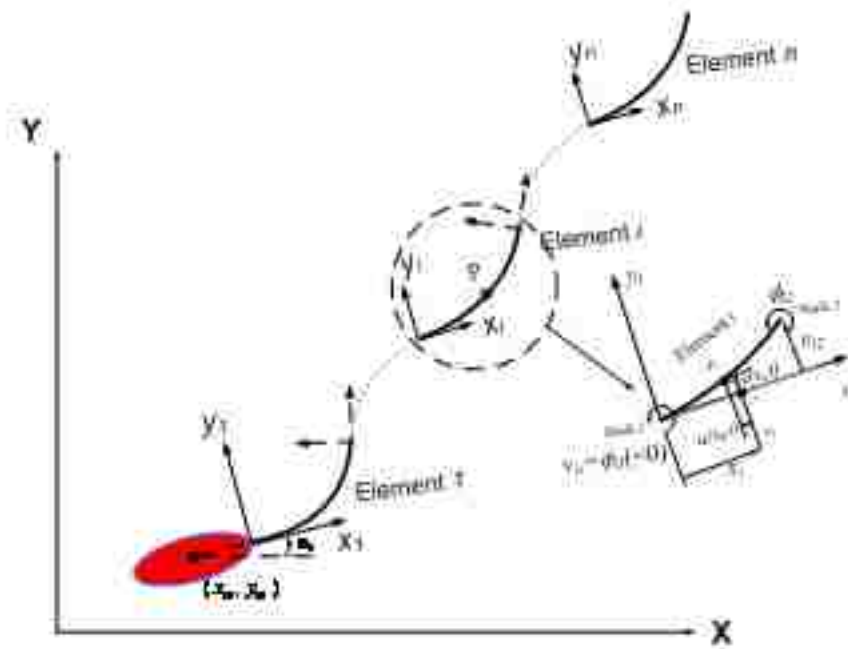


Figure 4.1: Schematic representation of the IPMC-driven vehicle and coordinate system

$$\begin{aligned}
{}^i r_p &= \begin{Bmatrix} x_m \\ y_m \end{Bmatrix} + \sum_{j=1}^{i-1} \left[ T_{\Phi_j} \begin{Bmatrix} L_j + q_j^T N_s(L_j) q_j \\ N(L_j) q_j(t) \end{Bmatrix} \right] + T_{\Phi_i} \begin{Bmatrix} x_i + q_i^T N_s(x_i) q_i \\ N(x_i) q_i(t) \end{Bmatrix} \\
i &= 1 \cdots n
\end{aligned} \tag{4.1}$$

where,

$$\begin{aligned}
T_{\Phi_i} &= \begin{bmatrix} \cos \Phi_i & -\sin \Phi_i \\ \sin \Phi_i & \cos \Phi_i \end{bmatrix} \\
\Phi_i &= \Phi_1 + \sum_{k=1}^{i-1} \phi_{k2}.
\end{aligned} \tag{4.2}$$

$x_m, y_m$  are coordinates of the center of mass of the head,  $\Phi_1$  is the rotation angle of the head and  $L_j$  is the length of each element. It should be noted that  $\phi_{k2}$  is the slope angle of the node 2 of the element  $k$  in its local coordinate frame, and  $\Phi_i$  is node  $i$  slope angle  $i$  global coordinate frame as shown in Fig. 3.4. Differentiating Equation 4.1 with respect to time, the velocity of a point  $P$  can be expressed as

follows:

$$\begin{aligned}
{}^i\dot{r}_p &= \begin{Bmatrix} \dot{x}_m \\ \dot{y}_m \end{Bmatrix} + \begin{Bmatrix} r_o \cos(\Phi_1) \\ r_o \sin(\Phi_1) \end{Bmatrix} \dot{\Phi}_1 \\
&+ \sum_{j=1}^{i-1} \left[ \dot{T}_{\Phi_j} \begin{Bmatrix} L_j + q_j^T N_s(L_j) q_j \\ N(L_j) q_j(t) \end{Bmatrix} + T_{\Phi_j} \begin{Bmatrix} 2q_j^T N_s(L_j) \dot{q}_j \\ N(L_j) \dot{q}_j(t) \end{Bmatrix} \right] \\
&+ \dot{T}_{\Phi_i} \begin{Bmatrix} x_i + q_i^T N_s(x_i) q_i \\ N(x_i) q_i(t) \end{Bmatrix} + T_{\Phi_i} \begin{Bmatrix} 2q_i^T N_s(x_i) \dot{q}_i \\ N(x_i) \dot{q}_i(t) \end{Bmatrix} \\
&\stackrel{\Delta}{=} P_i \dot{\xi}_i
\end{aligned} \tag{4.3}$$

where,  $\dot{T}_{\Phi_j} = \frac{\partial T_{\Phi_1}}{\partial \Phi_1} \dot{\Phi}_1 + \sum_{k=1}^{j-1} \frac{\partial T_{\Phi_j}}{\partial \phi_{k2}} \dot{\phi}_{k2}$ ,  $P_i \in \mathfrak{R}^{2 \times 4i+3}$  and

$\dot{\xi}_i = [\dot{x}_m \ \dot{y}_m \ \dot{\Phi}_1 \ \dot{q}_1^T \ \cdots \ \dot{q}_i^T] \in \mathfrak{R}^{4i+3}$  which is defined by coordinates associated with head and nodal vectors  $\dot{q}_i$  for each element.

#### 4.1.2 Energy formulation

Kinetic energy of the vehicle is sum of the kinetic energy of the head and kinetic energy of an IPMC. The kinetic energy of the head is given by,

$$T_h = \frac{1}{2} \dot{q}_h^T M_h \dot{q}_h \tag{4.4}$$

where,

$$M_h = \begin{bmatrix} m_h & 0 & 0 \\ 0 & m_h & 0 \\ 0 & 0 & I_h \end{bmatrix}$$

$$\dot{q}_h = [\dot{x}_h \ \dot{y}_h \ \dot{\Phi}_1]^T$$

Mass matrix of the head after expanding to the dimension of generalized coordinate,  $\xi_i$ , that includes nodal displacements and slopes of the IPMC, is expressed as:

$$M_{he} = \begin{bmatrix} M_h & 0_{3 \times 4n} \\ 0_{3 \times 4n} & 0_{4n \times 4n} \end{bmatrix} \in \mathfrak{R}^{(3+4n) \times (3+4n)} \quad (4.5)$$

Using mass and stiffness matrices of IPMC given in Equation 3.16 and 3.17, after expanding to the dimension vehicle with  $n$  elements, mass and stiffness matrices of element  $i$  are given by:

$$M_{ei} = \begin{bmatrix} M_i & 0_{(4i+3) \times 4(n-i)} \\ 0_{4(n-i) \times (4i+3)} & 0_{4(n-i) \times 4(n-i)} \end{bmatrix} \in \mathfrak{R}^{(4n+3) \times (4n+3)} \quad (4.6)$$

$$K_{ei} = \begin{bmatrix} 0_{(4(i-1)+3) \times (4(i-1)+3)} & 0_{4(i-1) \times 4i} & 0_{4(i-1) \times 4(n-i)} \\ 0_{4i \times 4(i-1)} & K_i & 0_{4i \times 4(n-i)} \\ 0_{4(n-i) \times 4(i-1)} & 0_{4(n-i) \times 4i} & 0_{4(n-i) \times 4(n-i)} \end{bmatrix} \in \mathfrak{R}^{(4n+3) \times (4n+3)} \quad (4.7)$$

Using the Lagrangian dynamics, the equations of motion for an element  $i$  can be determined as,

$$M_{ei}\ddot{\xi}_i + K_{ei}\xi_i = B_{ei}u_i(t) \quad (i = 1 \cdots 4n + 3) \quad (4.8)$$

Using equations 4.5 and 4.8, equations of motion of  $n$  element IPMC driven vehicle is given by:

$$M_e\ddot{\xi}_e + K_e\xi_e = B_e u \quad (4.9)$$

where,  $M_e = M_{he}^* + \sum_{i=1}^n M_{ei}^* \in \mathfrak{R}^{(2n+3) \times (2n+3)}$ ,  $K_e = \sum_{i=1}^n K_{ei}^* \in \mathfrak{R}^{(2n+3) \times (2n+3)}$ ,  $\xi_e = [x_m \ y_m \ \Phi_1 \ v_{12} \ \phi_{12} \cdots v_{n2} \ \phi_{n2}]^T \in \mathfrak{R}^{2n+3}$ , and  $M_{ei}^*$ ,  $M_{he}^*$  and  $K_{ei}^*$  are reduced form of  $M_{ei}$ ,  $M_{he}$  and  $K_{ei}$ , respectively.  $u \in \mathfrak{R}^n$  is an input moment vector and  $B_e \in \mathfrak{R}^{(2n+3) \times n}$  is an input control matrix for  $u$  in the reduced form of  $[B_{e1}^* \cdots B_{en}^*]$ .

## 4.2 Vehicle fluid interaction

Understanding the dynamic interaction between the surrounding fluid and both the vehicle and the IPMC flexible actuator is necessary for proper propulsion of the vehicle within fluid. It is planned to initially use the IPMC-driven vehicle in stationary water. Therefore, it is assumed that the vehicle will experience low Reynolds numbers, with only viscous forces namely, skin friction and form force acting on the IPMC. Based on this assumption, forces due to cross flow of the fluid are not considered. Figure 4.2 shows the skin friction ( $dF_t$ , tangential force) and form force ( $dF_n$ , normal force) acting over infinitesimal length  $ds$  on an element  $i$ .

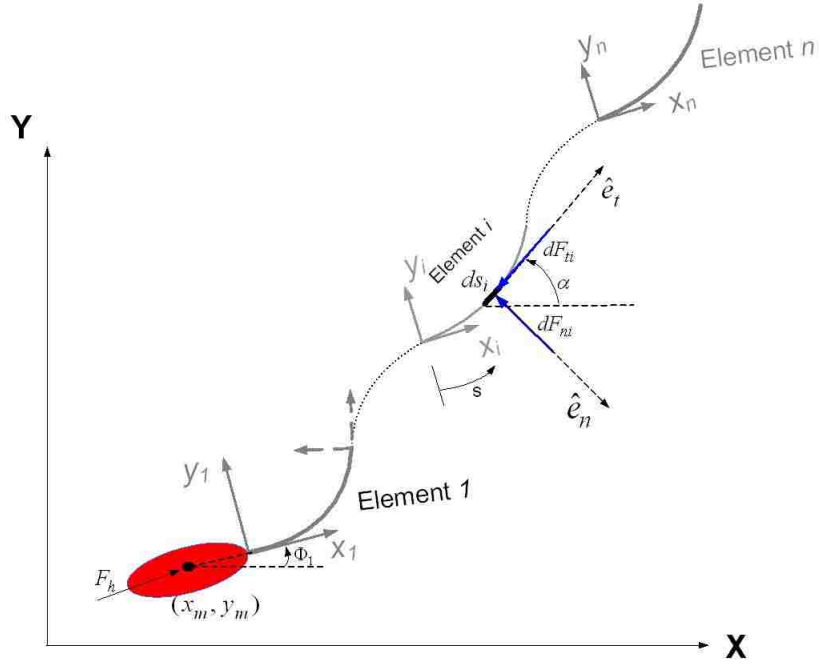


Figure 4.2: Hydrodynamic forces acting on the infinitesimal element  $ds_i$  of the element  $i$

The infinitesimal element of length  $ds_i$  has two velocity components namely, normal component,  ${}^i\dot{r}_\perp$  and tangential component,  ${}^i\dot{r}_\parallel$ . In both the normal and tangential directions, surrounding water exerts the resistive forces  $df_{ni}$ ,  $df_{ti}$  respectively on the element  $ds_i$ . The force equations presented in this section are based on [54, 55].

The tangential force,  $df_{ti}$ , is generated by the resistance of the fluid to shearing. This viscous force is proportional to the square tangential component of the velocity and is expressed as,

$$dF_{ti} = -\frac{1}{2}\rho_w C_t {}^i\dot{r}_\parallel \parallel {}^i\dot{r}_\parallel \parallel ds_i \quad (4.10)$$

where,  $\rho_w$  is density of water,  $C_t$  is coefficient associated with tangential force and  $b$  is width of the IPMC.

The form force is generated due to pressure difference caused by bending of the IPMC. It varies with the square of the normal component of velocity and is expressed as,

$$dF_{ni} = -\frac{1}{2}\rho_w C_n \dot{r}_\perp \|\dot{r}_\perp\| ds_i \quad (4.11)$$

where,  $C_n$  coefficient associated with form force.

The hydrodynamic force,  $dF_i = dF_{ti} + dF_{ni}$ , exerted on the element  $ds_i$  can be included in equations of motion of the element, 4.9, using the principle of virtual work. By noting that the position vector  ${}^i r_p$  of any point  $p$  on element  $i$  is a function of generalized coordinate,  $\xi_e = [x_m \ y_m \ \Phi_1 \ v_{12} \ \phi_{12} \ \cdots v_{n2} \ \phi_{n2}] \in \mathfrak{R}^{2n+3}$ , virtual work done by  $dF_i$  can be expressed as,

$$\delta W_i = dF_i^T \delta {}^i r_p = \sum_{k=1}^{2n+3} \left[ dF_i \frac{\delta {}^i r_p}{\delta \xi_{e,k}} \right] \delta \xi_{e,k} \triangleq \sum_{k=1}^{2n+3} dQ_{k,i} \delta \xi_{e,k} \quad (4.12)$$

where,  $dQ_{k,i}$  is the generalized force associated with the hydrodynamic force  $dF_i$  for the element  $ds_i$  located on element  $i$ . The generalized force associated with the total hydrodynamic force acting along the entire  $n$  elements is obtained by integrating along the length of each element and summing up all the element contributions and expressed as,

$$Q_k = \sum_{i=1}^n \int_0^{L_i} dQ_{k,i} dx_i \quad (4.13)$$

Similarly, the drag force acting on the head is calculated using the following Equation[56],

$$F_d = \frac{C_{dh}\rho_w V_h \| V_h \| S}{2} \quad (4.14)$$

where,  $C_{dh}, V_h, S$  are the drag coefficient, velocity and wet surface area of the vehicle head respectively. The hydrodynamic force,  $F_d$  acts along the global x, y axes and is concentrated at the center of mass of the head. The coefficients of tangential force, form force, and drag are to be found from the CFD studies. These coefficients are also verified by comparing the CFD results with experimental data and available literature.

The generalized hydrodynamic force,  $Q_k$  acting on the IPMC and drag force,  $F_d$ , acting on the head are added to the equations of motion given by Equation 4.9, and the augmented dynamic equation can be written as,

$$M_e \ddot{\xi}_i + K_e \xi_i = B_e u + Q + F_{de} \quad (4.15)$$

where,  $Q = [Q_1, Q_2, \dots, Q_{2n+3}]^T$ .  $F_{de} = [F_d^T, 0_{2n+1}]^T$ , is the drag force acting on the head and expanded to the dimension of generalized coordinate.

The dynamic model of underwater vehicle given in Equation 4.15 combined with the electrical model given by Equations 2.11 and 2.12. The combined dynamic



equation can be written in state-space form as,

$$\begin{aligned}
M_e \ddot{\xi}_i + K_e \xi_i &= B_e u + Q + F_{de} \\
&= B_e B_u Z + Q + F_{de} \\
\dot{Z} &= A_z Z + B_v V
\end{aligned} \tag{4.16}$$

### 4.3 Simulations and Experiments

To identify the parameters and validate the proposed model, two different types of the simulations and experiments are carried out. The first set of simulations and experiments deal with the identification of the coefficients used in the hydrodynamic model, followed by experimental electrical parameter identification.

#### 4.3.1 Description of the IPMC propelled vehicle

The IPMC-propelled vehicle used in the present study is shown in Fig. 4.3. It consists of rigid body and an IPMC to propel the vehicle. The vehicle, which is created in a rapid prototyping machine, is made up of ABS (Acrylonitrile Butadiene Styrene) plastic. The vehicle is powered externally. The vehicle's dimension and parameters are given in Table 4.1. Table 4.2 lists the mechanical characteristics of the IPMC.

#### 4.3.2 Identification of hydrodynamic coefficients

The objective of this section is to identify coefficients of the hydrodynamic forces used in Equations 4.10 and 4.11. These coefficients are obtained from the results

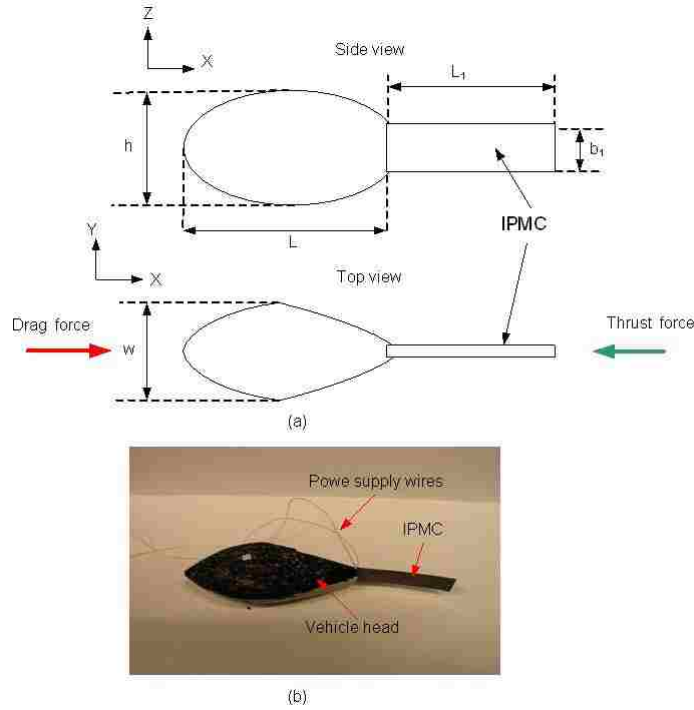


Figure 4.3: (a)Schematics of the IPMC propelled vehicle. (b) Photo of the IPMC propelled vehicle

of the simulations that are conducted using FLUENT, computational fluid dynamic software[57]. Assumptions related to swimming with low Reynolds number environment are based on [58, 59]. The fluid surrounding the IPMC is assumed to be incompressible. This observation allows the use of individual configuration of the IPMC in bending cycle in the CFD modeling.

The pre-processing for the CFD analysis is carried in GAMBIT, a modeling meshing software [60]. After creating the IPMC geometry and boundaries, meshing of the entire region is done. The boundaries are selected in such a way that they do not influence the flow field around the IPMC. Figure 4.4. shows a typical application of the IPMC where the vehicle is moving in stationary water. In CFD modeling, IPMC

Table 4.1: Vehicle dimensions and parameters

Variable	Value
$L$ (Length, m)	0.070
$h$ (height, m)	0.023
$w$ (width, m)	0.028
$m$ (mass, kg)	0.020
$S$ (wetted surface area, $m^2$ )	2.571e-03

Table 4.2: IPMC Mechanical Characteristics

Variable	Value
$\rho_p$ (density of electrode(Pt)[53], $\frac{Kg}{m^3}$ )	21500
$\rho_g$ (density of Nafion)[53], $\frac{Kg}{m^3}$ )	2600
$L$ (length of the IPMC actuator, m)	0.043
$b$ (width of the IPMC actuator, m)	0.011
$h_b$ (thickness of Nafion), m)	0.00028
$h_g$ (thickness of electrode(Au)), m)	0.000002
$E_b$ (Young's modulus of elasticity for Nafion, Pa)	$5e^7$
$E_g$ (Young's modulus of elasticity for electrode (Pt)[53],Pa)	$144e^7$

is assumed to be stationary with water flowing opposite to propulsion direction. The boundary condition for the inlet is steady uniform flow at a velocity typical for the IPMC actuated vehicle. The downstream boundary is modeled as constant pressure outlet, while the sides are modeled as slip walls. The IPMC is modeled as a smooth no slip wall. General modeling assumptions suggested in [61] are used in the study.

Figure 4.5. shows a typical computational domain for a bent IPMC. The mesh resolution in the vicinity of the IPMC is finer to account for the smaller changes in the flow properties. Mesh resolution becomes coarser as the far field boundaries are approached since the flow gradients approach zero as the Fig. 4.5 shows.

FLUENT CFD code is used to model the flow field around the IPMC actuator by solving the two-dimensional form of the incompressible Navier-Stokes and continuity equations. The Navier-Stokes momentum equations are discretized using first order upwind scheme. While pressure is interpolated using the standard discretization scheme, the SIMPLE (Semi-implicit method for pressure linked equations) algorithm is used for pressure velocity coupling of the continuity equation.

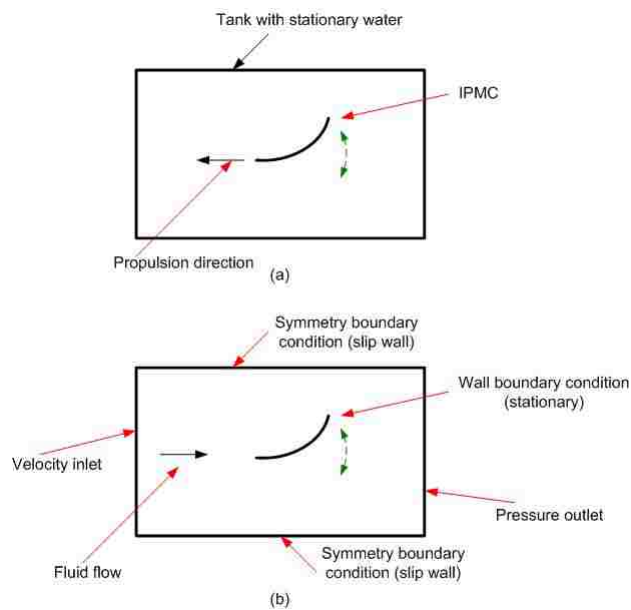


Figure 4.4: (a)Physical application of IPMC. (b) two-dimensional computational domain

To check the mesh dependency of the CFD results, simulations are carried out using three different mesh sizes and the results are shown in Fig. 4.6 and 4.7. Simulations are run using two flow speeds, 0.0075 m/s and 0.015 m/s. The drag coefficient,  $C_D$ , and lift coefficient,  $C_L$ , are calculated in both  $x$  and  $y$  directions re-

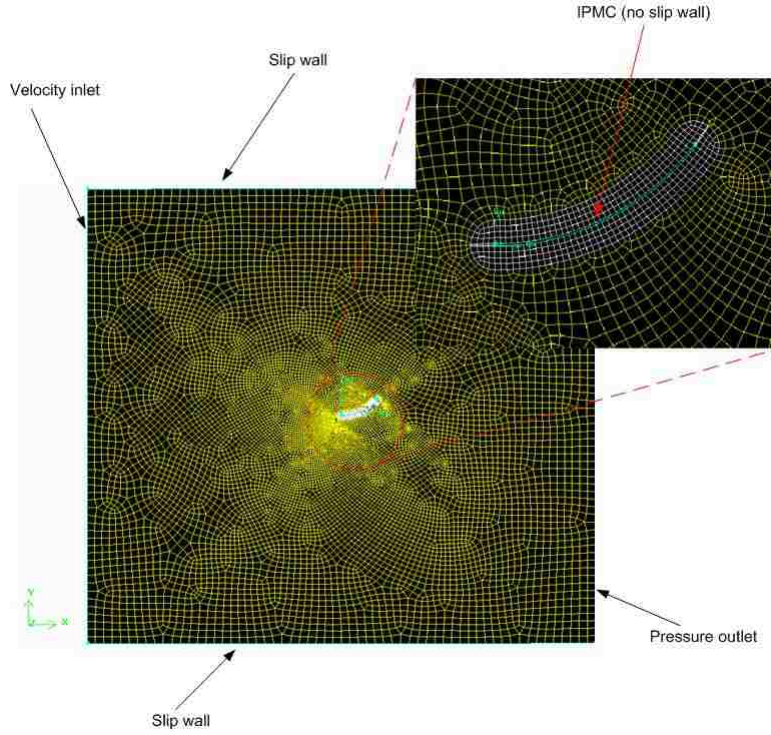


Figure 4.5: Typical computational domain of IPMC

spectively. These two figures show that the values of  $C_D$  and  $C_L$  are stable. Selected values of these coefficients are shown on the Fig. 4.6 and 4.6. The shape of the curve and the location of the end point are based on experimental verification as shown in Fig. 4.8. Figures 4.9 and 4.10 show the variation of selected  $C_D$  and  $C_L$  values with an angle of attack and a flow speed respectively. Due to very small variation of lift and drag coefficients with the flow speed, average values are taken and curve fitting is done to obtain the relation between the angle of attack and  $C_L, C_D$  values. The calculated lift and drag coefficients are found to be close to those of a flat plate with infinite aspect ratio and varying angles of attack at low Reynolds number ( $Re = 300$ ) [62]. The polynomial fits for the average  $C_D, C_L$  values are given below.

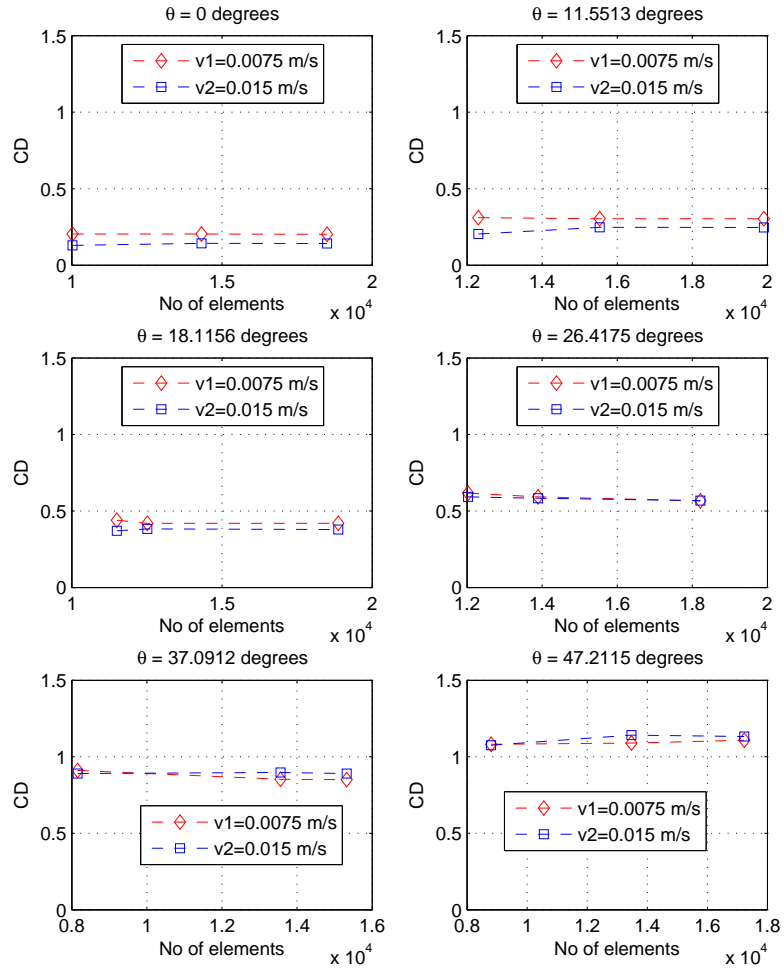


Figure 4.6: Mesh dependency studies for the drag coefficient

$$C_D(\theta) = 3.8106\theta^4 - 7.3106\theta^3 + 5.2602\theta^2 - 0.3276\theta + 0.1793 \quad (4.17)$$

$$C_L(\theta) = -1.1744\theta^4 - 6.1386\theta^3 - 10.8746\theta^2 + 6.7958\theta + 0.0035 \quad (4.18)$$

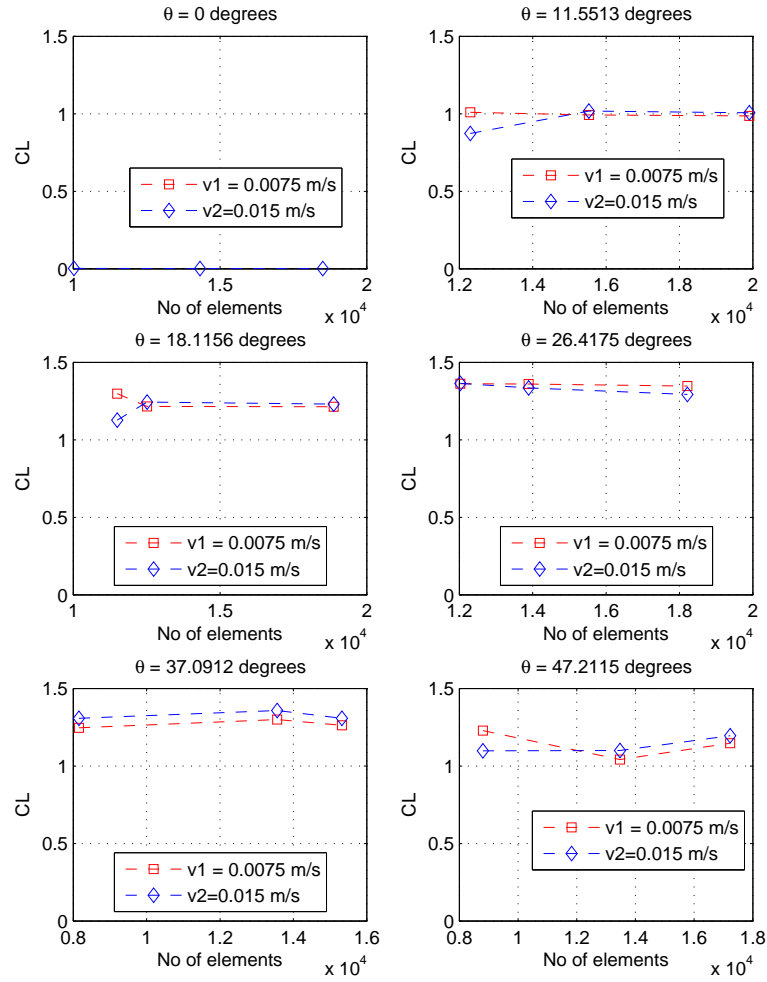


Figure 4.7: Mesh dependency studies for the lift coefficient

where,  $\theta$  is in radians and  $0 \leq \theta \leq 0.9$ .

The next step is to transform drag and lift coefficients from global to local frames. Figure 4.11 shows the relation between these two frames for the IPMC undergoing bending. As explained earlier, the drag and lift coefficients,  $C_D$  and  $C_L$  respectively, are found for each configuration and expressed as functions of  $\theta$ . These variables are

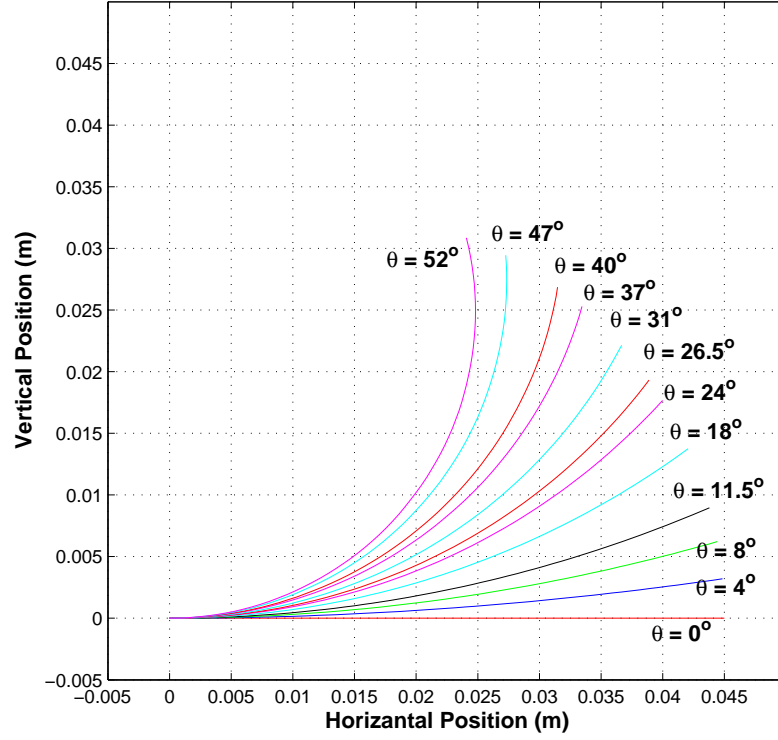


Figure 4.8: IPMC configuration and corresponding reference angles

transformed to  $C_n$  and  $C_t$  as given in the equation below.

$$\begin{aligned}
 C_t(\theta_n) &= C_d(\theta_n) \cos(\theta_n) + C_L(\theta_n) \sin(\theta_n) \\
 C_n(\theta_n) &= -C_d(\theta_n) \sin(\theta_n) + C_L(\theta_n) \cos(\theta_n)
 \end{aligned}
 \tag{4.19}$$

### 4.3.3 Identification of drag coefficient of vehicle head

It is necessary to have an estimate of the vehicle head drag force to fully understand the motion of the vehicle. It is proposed to use CFD to calculate the drag coefficients on the head. A three-dimensional computational domain, Fig. 4.12, is used to study



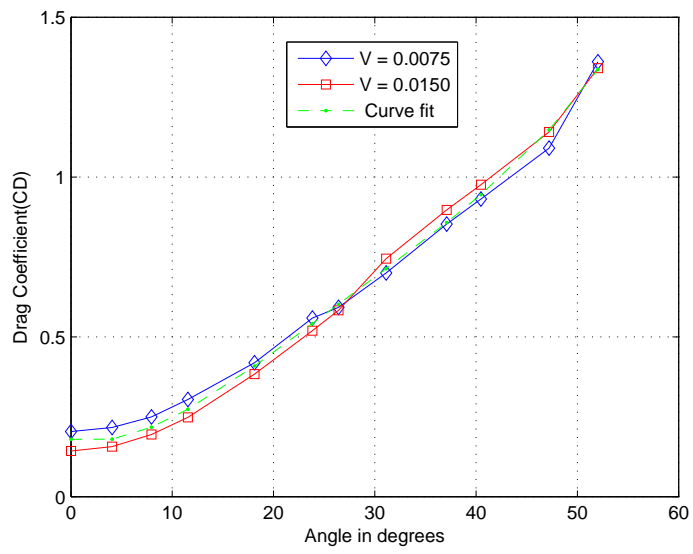


Figure 4.9: Drag coefficient variation with angle of attack

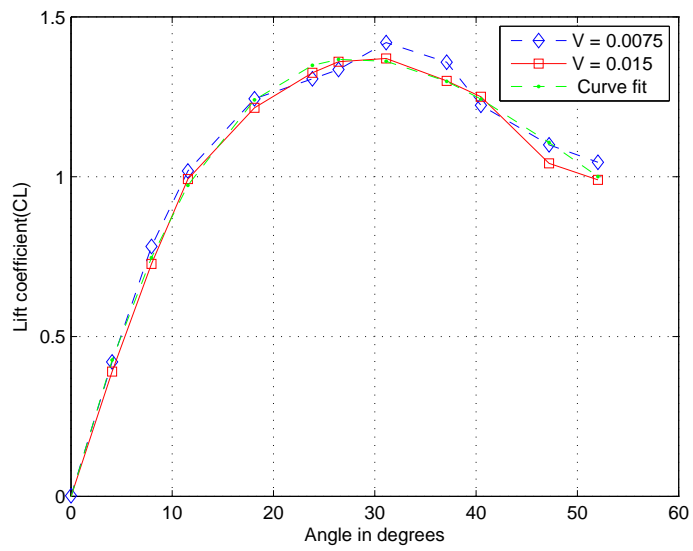


Figure 4.10: Lift coefficient variation with angle of attack

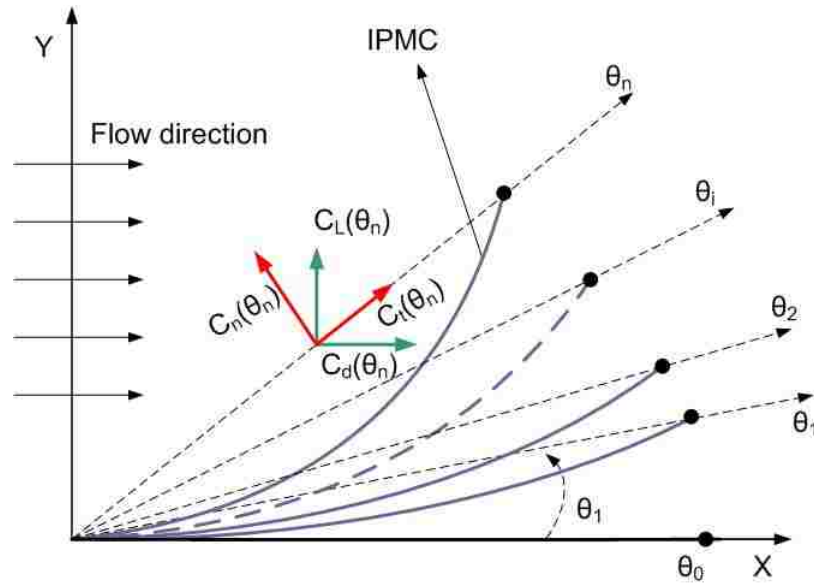


Figure 4.11: Schematic representation of a configuration in bending cycle of IPMC and hydrodynamic friction coefficients

the variation of head drag coefficients with the speed of the vehicle. This CFD model is symmetric about the  $y - z$  plane, and it is assumed that only half of the vehicle is in water. The solution procedure is similar to the one described earlier in this section except:

- Three-dimensional form of Navier-Stokes and continuity equations are used
- The angle of attack of the vehicle head is maintained to be zero as the vehicle head is assumed to be moving along the  $z$ -direction.
- Oscillations of the head about the  $z$ -axis are negligible

The meshed computational domain is shown in Fig. 4.13. Simulation results for the variation of drag coefficient of on the head with respect to vehicle speed are shown

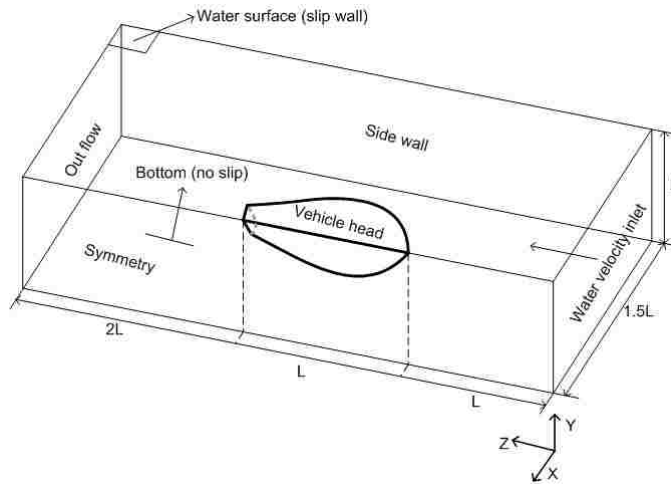


Figure 4.12: Computational domain and geometry of the fish head

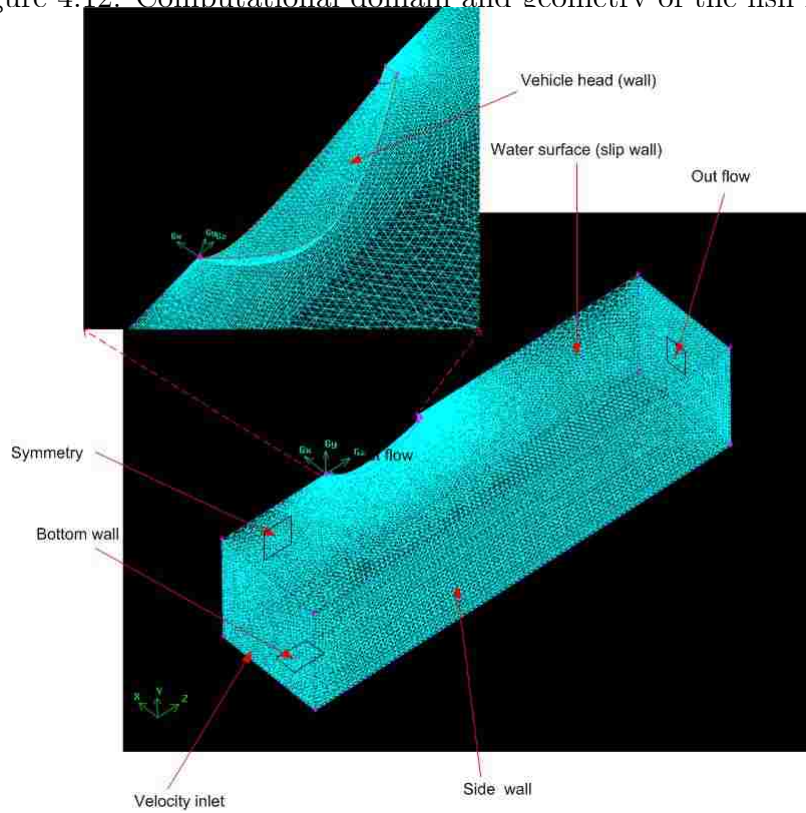


Figure 4.13: The computational domain mesh

in Fig. 4.16. The relation between the speed of the vehicle and drag coefficients are fitted as,

$$C_{dh}(V_h) = (6.6436V_h^4 - 0.6399V_h^3 + 0.0227V_h^2 - 0.3725 \times 10^{-3}V_h + 0.003 \times 10^{-3}V_h)10^5 \quad (4.20)$$

The CFD results are validated by measuring the drag force using the experimental setup shown in Fig. 4.14. The drag force on the vehicle head is measured by pivoting it to an axle through a rigid arm. The Ball bearing shown Fig. 4.14 significantly reduces the friction between the axle and housing. To further reduce the noise in the load signal, the whole setup is kept stationary and the water tank is moved with different velocities using a linear slide driven by a stepper motor. The measured drag force at velocity of 0.01 m/sec is shown in Fig. 4.15. Equation 4.14 is used to find the drag coefficient from the drag force and velocity data obtained from this experimental setup.

A comparison of simulation and experimental results for the variation of drag coefficient of the head with respect to vehicle speed is shown in Fig. 4.16. The error bars in Fig. 4.16 show the variation of the drag coefficient due to variation of the drag force from the mean value.

#### 4.3.4 Identification of electrical constants

The constants of the electrical model given in Equation 2.1 are found by applying step input voltage to the IPMC and measuring the resulting current as shown

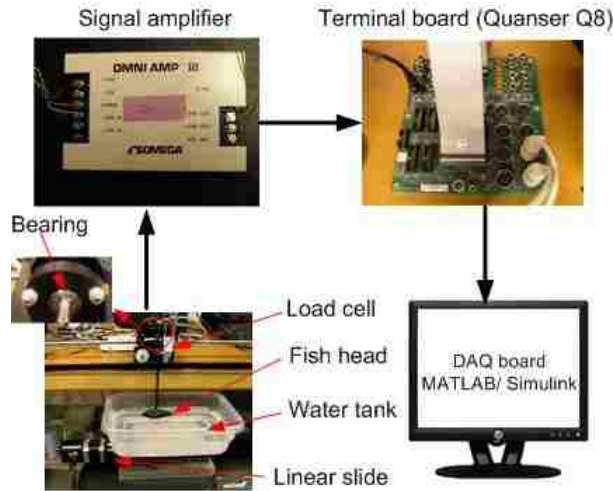


Figure 4.14: Experimental setup for measuring the drag force on the vehicle head

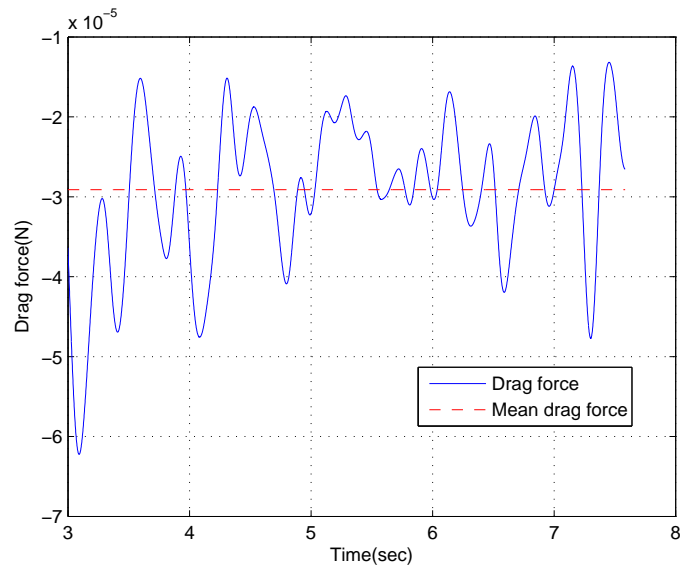


Figure 4.15: Filtered drag force on the vehicle head at  $V = 0.01m/sec$

in Fig. 4.17. MATLAB System identification toolbox used for this purpose. The electrical parameters obtained from the system identification procedure are shown in Table 4.3.

The constants  $\tau_u$  and  $K_u$  in the first order model of the Equation 2.3 are found

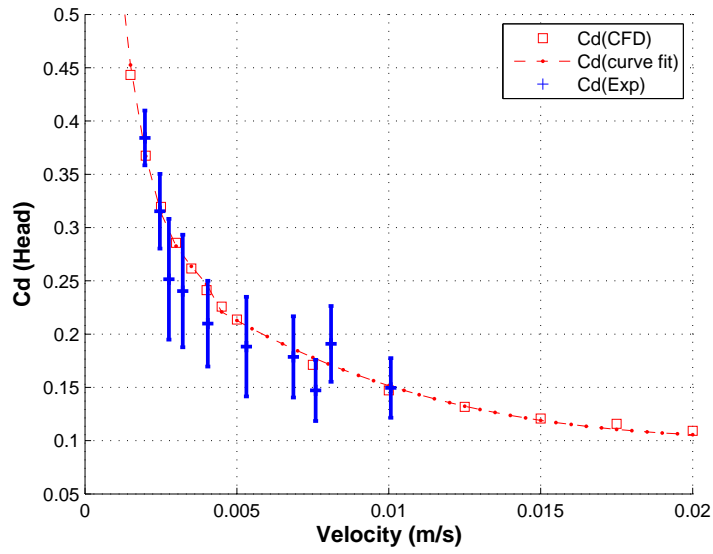


Figure 4.16: Head drag coefficient variation with respect to speed of the vehicle

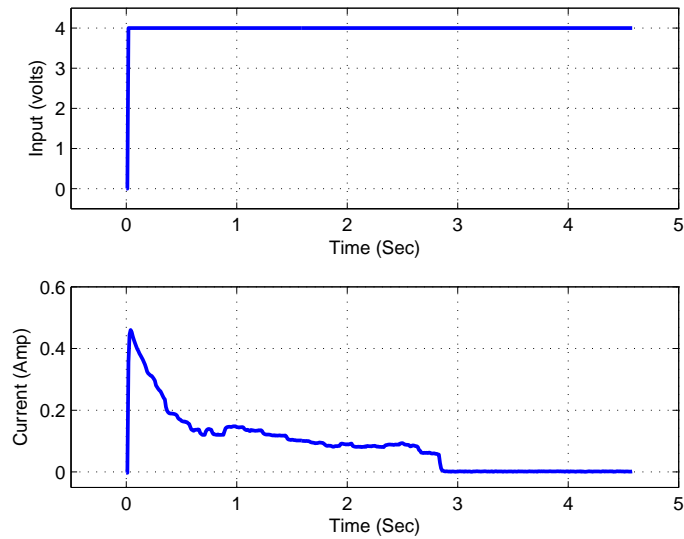


Figure 4.17: Step input voltage applied and measured current

by applying step input of 4 volts to the IPMC and measuring the the corresponding moment generated at the free end. Moment is determined by measuring the blocking force using the the experimental setup shown in Fig. 3.5. The measured blocking force

Table 4.3: Identified electrical parameters

Variable	Value
$R_2, \Omega$	145
C, F	0.15562
$\tau_q (= R_1 C)$ , sec	1.5251
$\tau_{u1}$ , sec	1.5129
$K_u$	3.3012e-04
$\tau_{u2}$ , sec	57.3786

is shown in Fig. 4.18. MATLAB System identification Toolbox is used to identify the first order relation between the charge induced and the moment generated. The identified parameters are shown in Table 4.3.

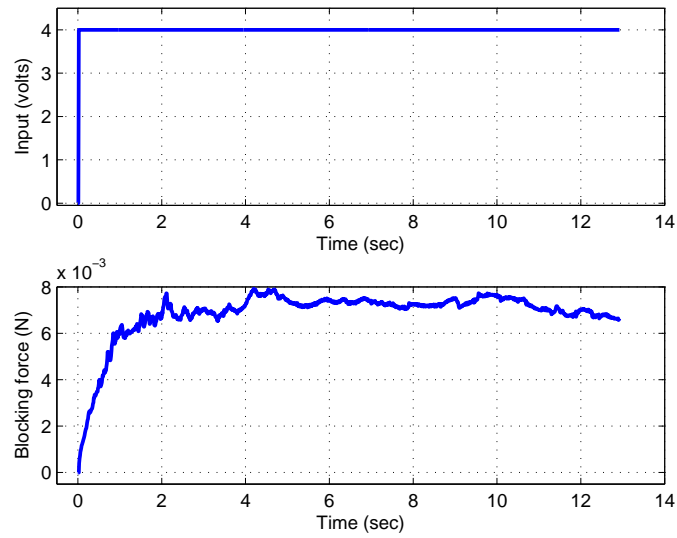


Figure 4.18: Measured blocking force

#### 4.4 Model validation

To validate the proposed modeling technique, simulations are conducted using the parameters of the vehicle given in Table 4.1 and 4.2. Considering the small deformations of IPMC for high frequency input signal, and based on earlier experience[63], it is decided to use two elements to model the IPMC deformation. The hydrodynamic coefficients, electrical constants identified in Chapter 2 are used in the simulations. Figure 4.19 shows the experimental setup for measuring the displacement of the vehicle. The vehicle position is recorded by placing a grid sheet at the bottom of the tank. The images are recorded by a camera that is placed above the setup. Figure 4.20 shows the simulated and experimental displacement of the vehicle for actuation signal of amplitude 4 and 5 volts respectively at a frequency of 2Hz.

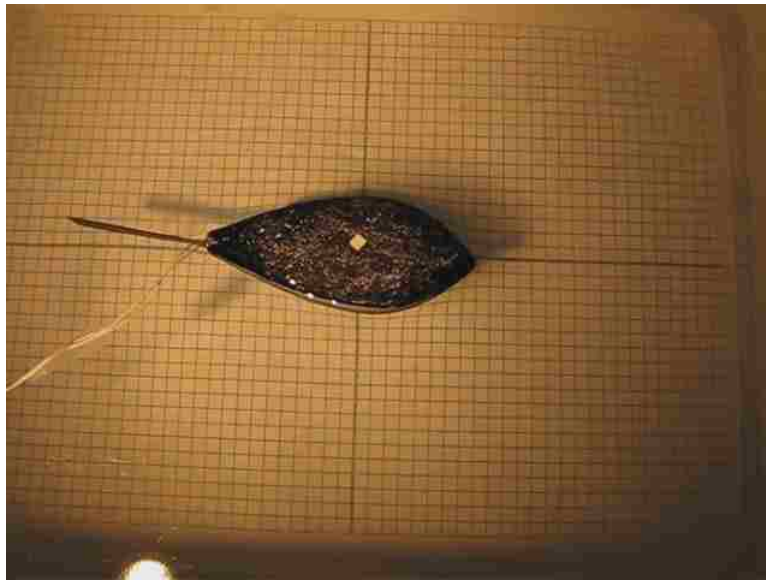


Figure 4.19: IPMC driven vehicle in the tank



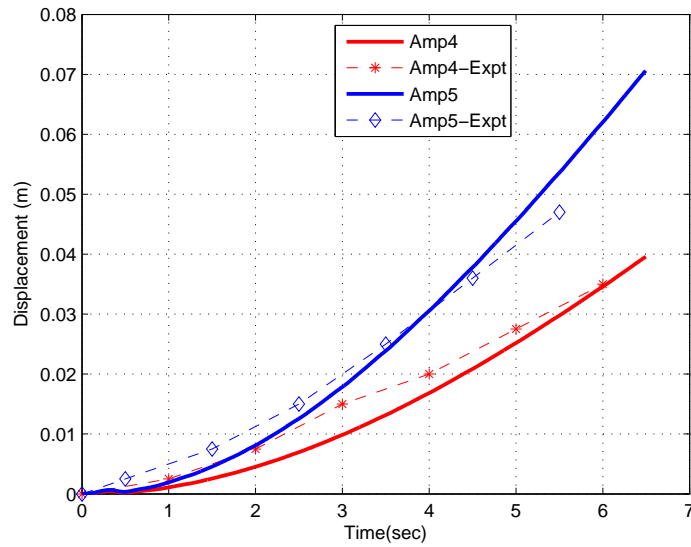


Figure 4.20: Comparison of simulated and experimental displacement of the vehicle for 4 and 5 volts sinusoidal inputs

#### 4.5 Autonomous IPMC propelled vehicle

The IPMC propelled vehicle developed in section 4.3.1 uses external power for actuating IPMC. Due to tethered power supply, it has limited mobility and fewer applications. To overcome this difficulty, autonomous IPMC propelled vehicle is developed using on board batteries for power supply and a micro controller for generating actuation signal. In present application, 8 bit AVR microcontroller [64] is selected for interfacing IPMC actuator. Compact size, serial interface capability and low supply voltage makes it suitable to use in miniature robotic vehicles. The micro controller has only digital outputs and can not generate analog sinusoidal voltage required to drive IPMC actuator. However, using PWM with variable duty cycle one can ap-

proximate the sine wave. Two LEDs are used to track the position and orientation of the vehicle. Two 3 volt batteries are used for power supply. It is also equipped with a wireless communication module to facilitate remote control.

#### 4.5.1 Design of the vehicle

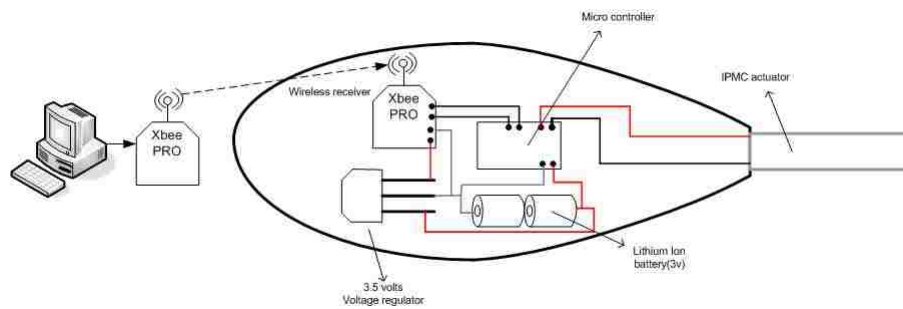


Figure 4.21: Schematics of the IPMC propelled vehicle

Figure 4.21 illustrates the overall design of the vehicle. Vehicle is designed as hollow shell using SolidWorks modeling software and printed on rapid prototyping machine. ABS plastic was used because of its light weight and water proof qualities. **Xbee** wireless module is used to send and receive instructions from a PC. Microcontroller coordinates the multiple essential operations related to communication and control. As shown in figure 4.22, body houses all the electronics and propelled by IPMC actuator attached at the end. Two LEDs mounted on the top of the vehicle are used for tracking purpose.

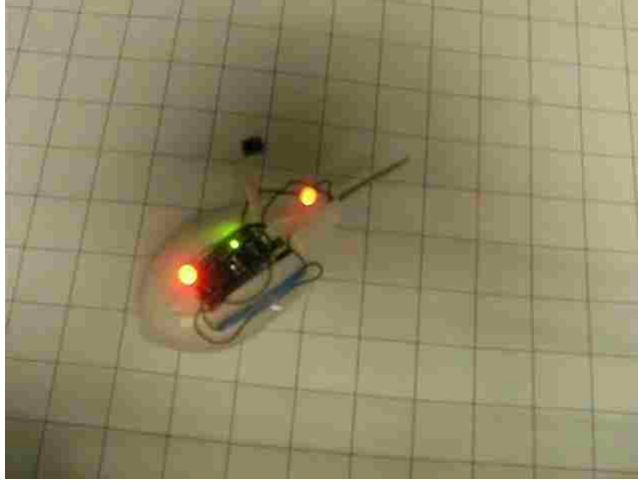


Figure 4.22: IPMC propelled vehicle in tank

#### 4.5.2 Wireless communication and Control

Two **Xbee PRO<sup>TM</sup>** modules from the *DIGI International Inc.* are used for wireless communication between the PC and the IPMC propelled vehicle. One module is connected to the PC through serial port and one to the vehicle. Two **Xbee** modules use **ZigBee** wireless communication protocol. Compared to other wireless communication protocols such as *Bluetooth<sup>TM</sup>* or *Wi-Fi<sup>TM</sup>*, it has advantages such as low power consumption, large transmission range (over 100 m) and capability of mesh networking. A microcontroller (ATMEL ATmega168/328 [64]) used for coordinating between wireless module and IPMC actuator. Through serial interface with **Xbee** module, the microcontroller establishes communication with the PC.

Table 4.4: Autonomous vehicle dimensions and parameters

Variable	Value
$L$ (Length, m)	0.110
$h$ (height, m)	0.050
$w$ (width, m)	0.070
$m$ (mass, kg)	0.070
$S$ (wetted surface area, $m^2$ )	4.91e-03

#### 4.6 Experimental results and comparison with the proposed model

The experimental setup for measuring the position of the autonomous IPMC driven vehicle is shown in the Fig.4.23. Vehicle dimensions and parameters are given

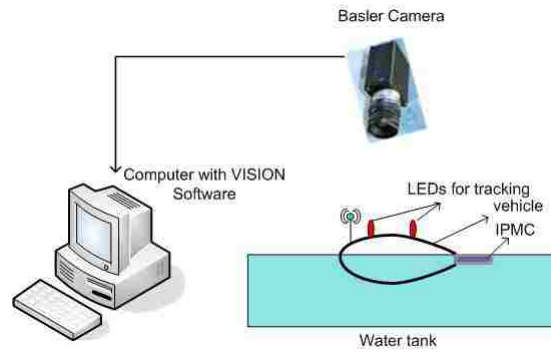


Figure 4.23: Experimental setup for measuring the position of the IPMC driven vehicle

in Table4.4. Two separate experiments were conducted to record speed and heading of the vehicle. It should be noted that heading of the vehicle is measured with respect to inertial frame as shown in the Fig.4.1. Frequency of the input voltage is maintained at 2Hz as it falls near the natural frequency of the IPMC. Position of the

vehicle is recorded using the LEDs mounted on the vehicle. A video capturing system recording  $3 \text{ frames/sec}$  is used to record the position of the vehicle by tracing the two LEDs mounted on the vehicle. Figure 4.24 shows a comparison between the simulated and experimental results of the vehicle position and speed. Results show close match between the proposed model and the experimental data. The observed discrepancy between the simulations and experiments is due to the disturbance forces resulting from the fluid interaction with the tank boundaries. Eventually, as the vehicle speed approaches the steady state, there is a good agreement between the simulated and the experimental results.

The same experimental procedure is repeated to measure the heading angle of the vehicle. In the experiment above, actuation signal was symmetric about the x-axis. However, as shown in the Fig. 4.25, the actuation signal applied to IPMC in the heading angle experiment is biased. Due to asymmetric oscillations of the IPMC actuator, in addition to thrust force, constant moment acts on the vehicle and thus the constant rotation of the vehicle. As shown in the Fig 4.26, the heading angle increases constantly due to constant moment about the center of mass of the vehicle and there is a good agreement between the experimental and simulated results. Results can be improved further by considering the resistance due to angular velocity of the vehicle.

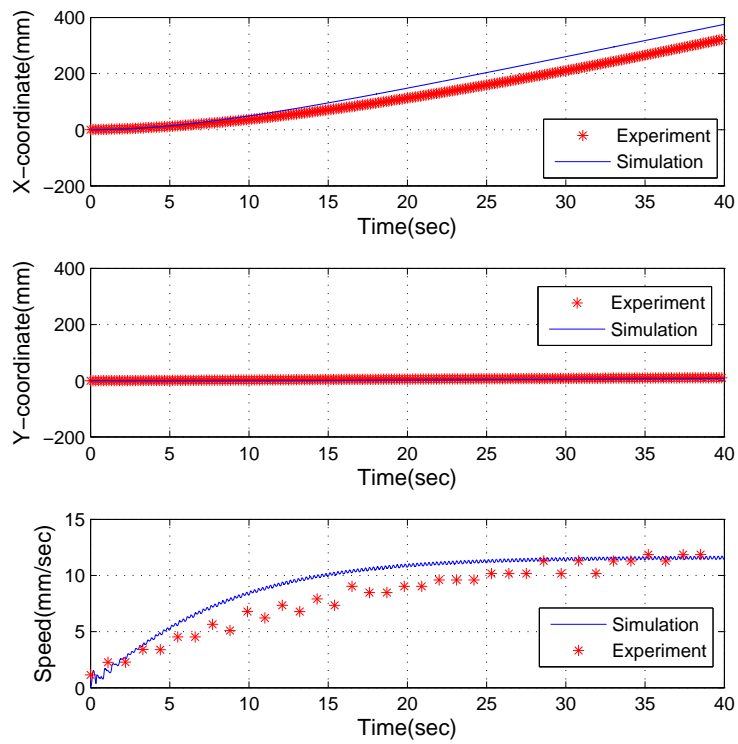


Figure 4.24: Comparison of simulated and experimental results when sinusoidal input of 6volts applied across IPMC actuator

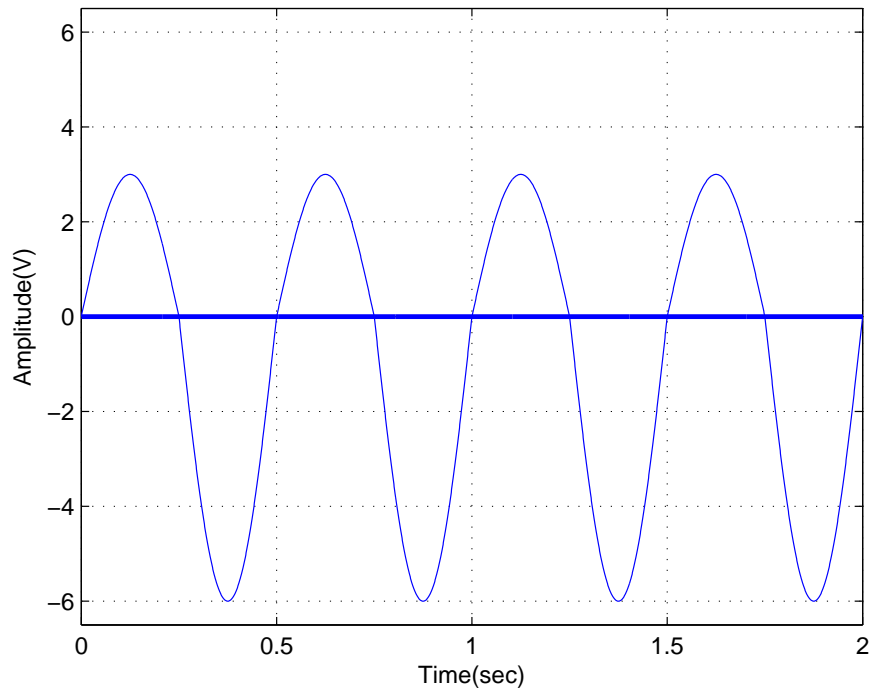


Figure 4.25: Actuation signal applied to IPMC actuator

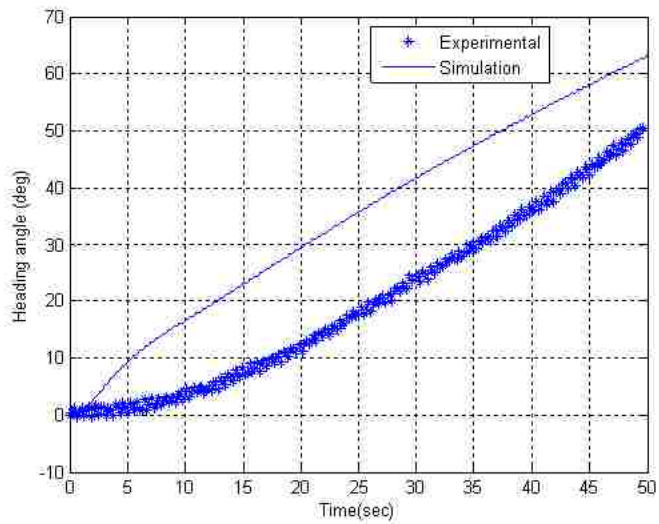


Figure 4.26: Experimental and simulated heading angle results

## 4.7 Summary

In this chapter, a dynamic model of small scale underwater vehicle driven by the IPMC propulsor is developed. Finite element method is used to model a soft IPMC actuator interacting with fluid medium. Large deflection beam model developed in chapter 3 is used to describe the dynamic deflections of the IPMC. The large deflection beam model is combined with RC electrical model of chapter 2 to develop the equations of motion. The proposed model includes the hydrodynamic resistive forces that are applied along the normal and tangential directions of the flexible actuator surface. The hydrodynamic coefficients are found by interpreting extensive set of CFD numerical simulations. Similarly, CFD is used to calculate the head drag coefficient over range of velocity values. Experimental approach is used to identify the variables of the RC electrical model. The proposed modelling technique is validated through computer simulations and experiments. Results show that accurate results can be obtained with limited number of elements. The observed disparity between the simulated and experimental results can be partially attributed to the fact that a tethered power supply used in the experiments. To overcome this difficulty, an autonomous IPMC propelled vehicle is developed, which uses on-board power supply and electronics for actuating IPMC. Experiments were conducted to validate the dynamic model.



## CHAPTER 5

### FEEDBACK CONTROL OF IPMC PROPELLED VEHICLE

In this chapter, a closed-loop feedback controller is developed for underwater vehicle propelled by ionic polymer metal composite actuator (IPMC). Simulation data of the dynamic model developed in chapter 4 is used in this study. The path of the vehicle is controlled by simultaneously controlling the yaw angle and speed of the vehicle using the proportional controllers. Simulation data is utilized to find the relation between control input parameters namely, amplitude and bias of the voltage applied to the IPMC, and yaw angle and speed of the vehicle. In the simulations, frequency of the control input is assumed to be fixed around the natural frequency of the IPMC actuator, 2Hz. Simulation results show that the proposed controller can be effectively used to steer the underwater vehicle propelled by IPMC.

#### 5.1 Yaw and Speed Control

In the proposed control scheme, the trajectory of the vehicle is controlled by tracking the yaw angle (orientation) and speed of the vehicle. As shown in the Fig. 4.2 and 5.1, yaw angle,  $\Phi_1$ , is described as the angle between the *x-axis* of a coordinate frame attached to center of mass of the vehicle and global X-axis. Speed of the vehicle is described as the absolute velocity of the center of mass of the vehicle

as,

$$v_h = \sqrt{\dot{x}_m^2 + \dot{y}_m^2} \quad (5.1)$$

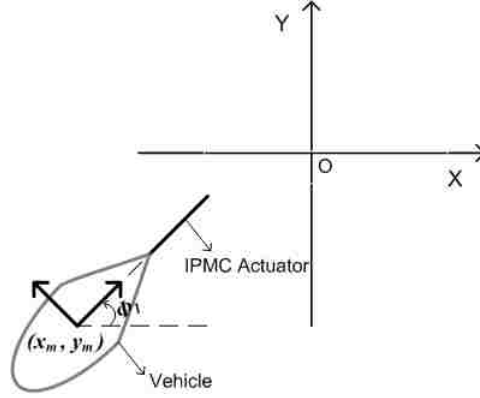


Figure 5.1: Schematic representation of the IPMC driven vehicle

### 5.1.1 Control law

As described earlier, the vehicle is driven by applying a sinusoidal voltage to IPMC actuator. Simulation data is used to find the dependency of the desired output variables namely, yaw angle, speed of the vehicle and the control input parameters, amplitude and bias of the voltage applied to the IPMC actuator. The frequency of the sinusoidal input is assumed to be fixed at 2 Hz. Figure 5.2 shows the variation of vehicle's average steady state speed with respect to amplitude and bias of the applied voltage. it's apparent from the Fig.5.2 that the bias in the control input has

little effect on the steady state speed of the vehicle. However, as the bias increases, oscillations increase around the average speed value as shown in Fig. 5.3. Compared to the magnitude of the average speed, these oscillations can be considered negligible. Therefore, the speed of the vehicle is directly related to the amplitude of the voltage applied to the IPMC actuator

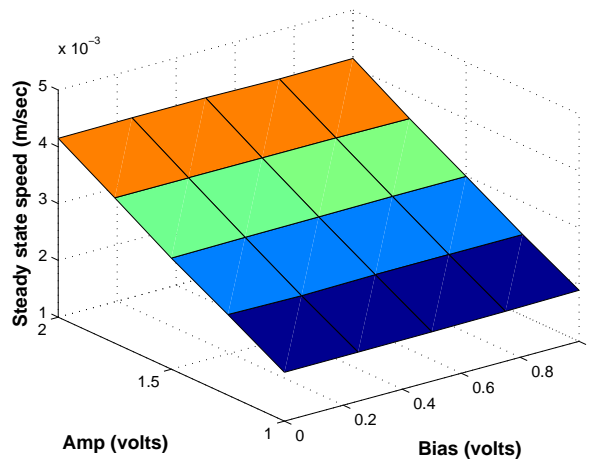


Figure 5.2: Variation of vehicle steady state speed,  $v_h$ , with respect to amplitude,  $A$ , and bias,  $B$ , of voltage input

To assess the effect of the input voltage amplitude and bias on the orientation (yaw angle) of the vehicle, simulations are done by varying the amplitude and bias of the input voltage and observing the resulting change in the yaw angle of the vehicle. As shown in Fig. 5.4(a), bias added to the input voltage at  $t = 10$  sec for  $0.5$ sec. The resulting change in the yaw angle is shown in the Fig. 5.4(b). Figure 5.5 shows the average change in the yaw angle with respect to amplitude and bias. It's clear

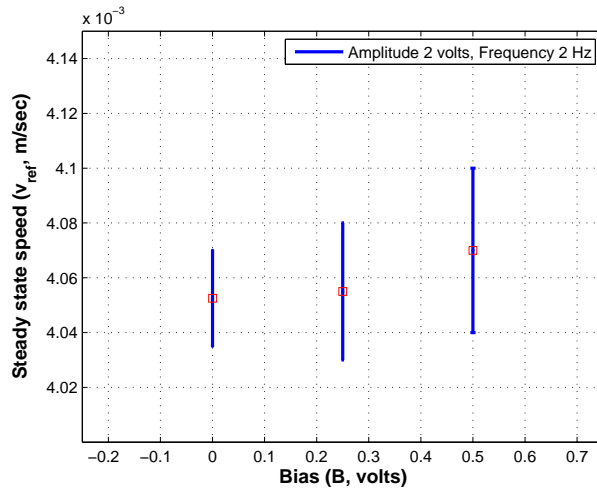


Figure 5.3: Variation of the steady state speed around the mean value with respect to the change in the input voltage bias

from Fig. 5.5 that the amplitude has little effect on the change in orientation of the vehicle when bias is applied. Therefore, Yaw angle is directly related to the bias of the voltage applied to the IPMC actuator.

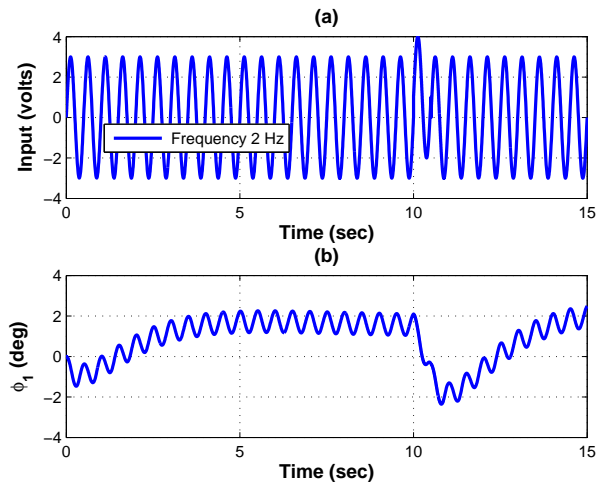


Figure 5.4: (a) Input voltage applied to IPMC ( $V_i$ ) . (b) Change in Yaw angle ( $\Phi_1$ )

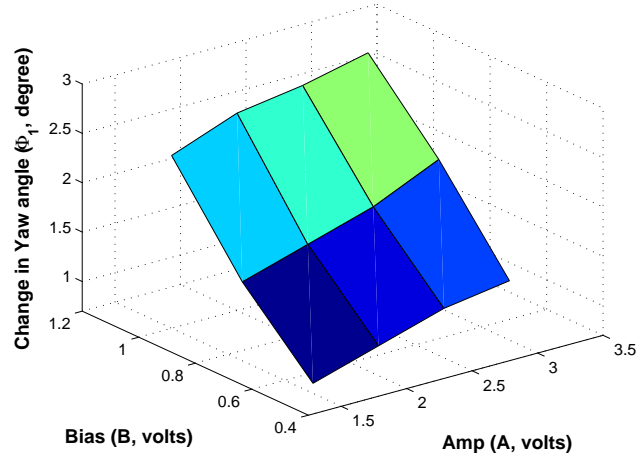


Figure 5.5: Change in vehicle Yaw angle ( $\Phi_1$ ) with respect to input voltage amplitude (A) and bias (B)

A possible control law for tracking the command speed of the vehicle may be expressed as:

$$A = K_v e_v + A_{ss} \quad (5.2)$$

where,  $A$  is the amplitude of control input voltage,  $K_v$  is the proportional gain for the speed tracking error,  $e_v$  is a tracking speed error, and  $A_{ss}$  is the constant voltage needed to maintain the desired steady state speed,  $v_{ref}$ . To assess the values of  $A_{ss}$  needed to reach reference steady state speeds for the vehicle ( $v_{ref}$ ), a series of simulations were conducted. The results of these simulations are shown in Fig. 5.6. Based on these results, the relation between  $A_{ss}$  and  $v_{ref}$  can be expressed in the

following polynomial form:

$$A_{ss} = 1.4718 \times 10^6 v_{ref}^3 - 3.396 \times 10^4 v_{ref}^2 + 6.09 \times 10^2 v_{ref} - 0.037 \quad (5.3)$$

where,  $1.86 \times 10^{-3} \leq v_{ref} \leq 10.6 \times 10^{-3}$ .

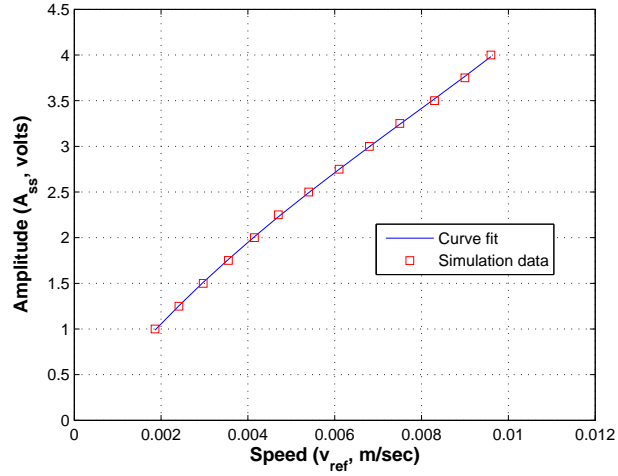


Figure 5.6: Relation between steady state speed ( $V_{ref}$ ) and amplitude ( $A_{ss}$ )

The control law for tracking the yaw angle is given by the equation,

$$B = -K_{\phi} e_{\phi} \quad (5.4)$$

where,  $B$  is the bias applied to the input voltage,  $K_{\phi}$  is the gain corresponding to the yaw angle tracking and  $e_{\phi}$  is error in tracking yaw angle.

Using Equations 5.2 and 5.4, control law is given by the equation

$$V_i = -K_\phi e_\phi + (A_{ss} + K_v e_v) \sin(2\pi ft) \quad (5.5)$$

where,  $V_i$  is voltage applied to the  $i^{th}$  element and  $f$  is the frequency of the control input fixed at 2Hz. The gains  $K_\phi$  and  $K_v$  are found on trial and error basis using the simulation results. The closed loop block diagram of the proposed controller is shown in Fig. 5.7. Considering the practical limitations on the magnitude of the voltage applied to IPMC and to limit the bending of the IPMC, voltage applied to the IPMC is saturated between 5 V.

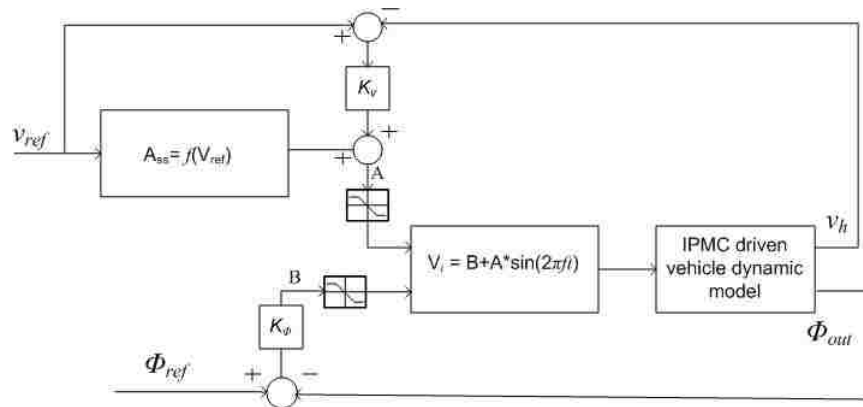


Figure 5.7: Feedback control of yaw angle and speed of the IPMC driven vehicle

## 5.2 Simulation Results

Computer simulations are conducted to assess the performance of the proposed feedback control scheme. The dimensions of the vehicle and the parameters of the IPMC used in the simulations are given in Table 3.1 and Table 4.1 respectively. The proportional gain values  $K_\phi$  and  $K_v$  are set to 50 and 1100 respectively. Figure 5.8 shows the simulation results for tracking the command yaw angle and speed using the selected  $K_\phi$ ,  $K_v$  values. Figure 5.8(a) shows that vehicle speed reaches the command speed in within 6 sec. The small deviations from the command speed observed at  $t = 15$  sec and  $t = 50$  sec are due to change in command yaw angle at that sampling instances. The steady state tracking error in speed is found to be less than 0.6%. As shown in the Fig. 5.8(b), vehicle reaches the command yaw angle in less than 1sec. The steady state error in tracking the yaw angle varies from 12 to 15% depending on the amplitude of the control input. The error in tracking yaw angle can be reduced by controlling the frequency of the control input.

## 5.3 Summary

In this chapter, a feedback controller was developed for tracking the speed and yaw angle of the IPMC driven vehicle developed in chapter 4. Vehicle trajectory is controlled by tracking the yaw angle (orientation) and speed of the vehicle simultaneously. Using the simulation data, speed of the vehicle is related to the amplitude of the voltage input applied of the IPMC and yaw angle is related to the bias in the input voltage. Frequency assumed to be fixed at 2Hz. Simulations show that



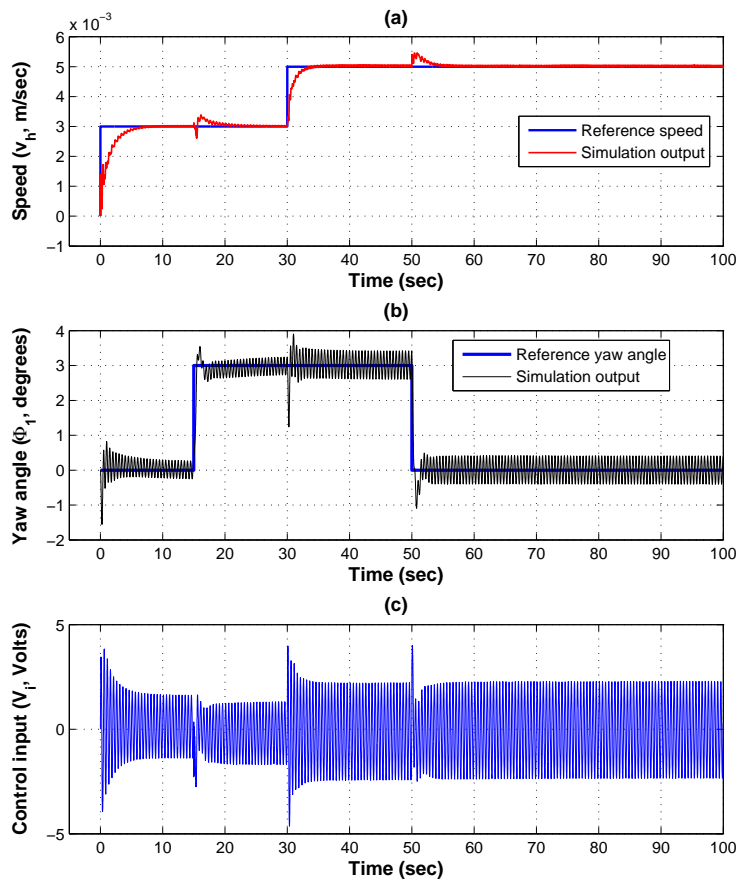


Figure 5.8: Simulation results for tracking the yaw angle ( $\phi_1$ ) and speed of the vehicle ( $v_{ref}$ )

the proposed control technique successfully tracks the command speed and yaw angle with very small steady state error.

## CHAPTER 6

### COMPUTER SIMULATION OF HEADING AND SPEED CONTROL

In this chapter, decoupling control algorithm is designed to control the speed and the heading angle of the IPMC propelled vehicle using the linear models. Here, the linear model is determined by simulating the non-linear model derived in chapter 4. This approach is used due to computational complexity of simulating non-linear model which includes hydrodynamic model of the vehicle and IPMC actuator. First, the computer simulation data from the non-linear dynamic model is used to find the transfer function between the vehicle motion and the control input to the IPMC actuator. The control input includes an amplitude and a bias voltage and the outputs are speed and heading angle of the vehicle. Next, decoupling controller transfer functions satisfying the desired closed loop response are found and the closed loop simulation is done using a full-scale dynamic model derived in Chapter4. In the control voltage applied to IPMC, the frequency is fixed at 2Hz which falls near natural frequency of the IPMC.

#### 6.1 System Identification

In this section, a linear relation is established between the output variables, speed,  $v_h(t)$ , heading angle,  $\phi(t)$ , and the control input parameters, amplitude,  $A(t)$ ,

and bias,  $B(t)$ . The definitions of input and output variables are shown in Fig. 6.1 and 6.2 respectively.

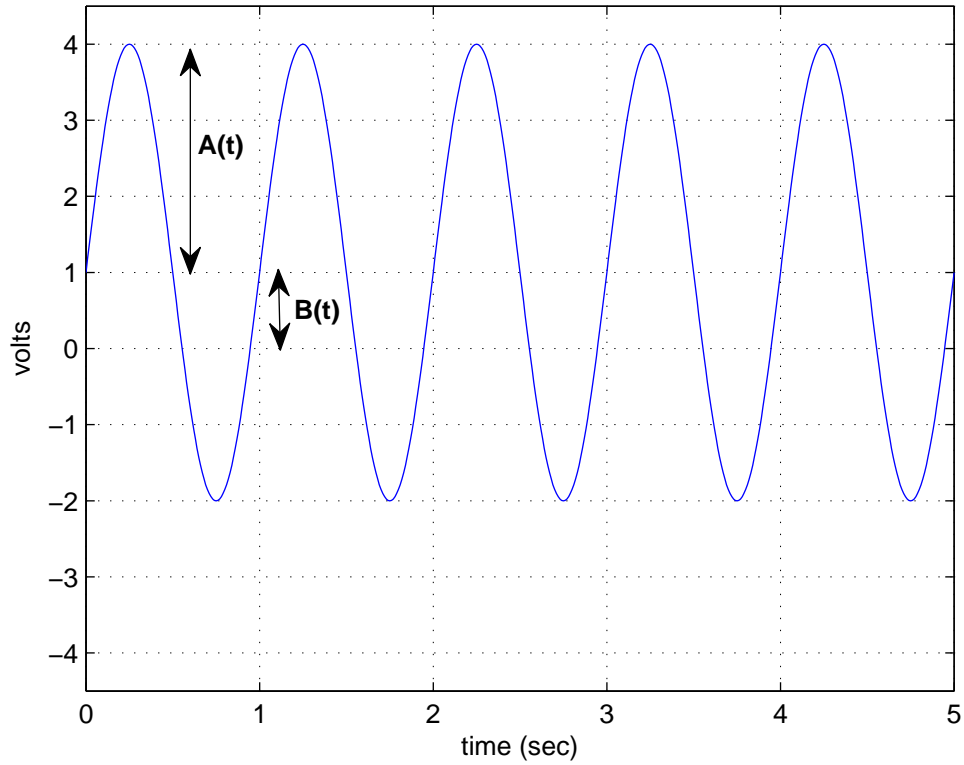


Figure 6.1: Definition of the control input parameters

### 6.1.1 Amplitude and speed model identification

The relation between the speed  $v_h(t)$  of the vehicle and the amplitude  $A(t)$  of the sinusoidal input voltage applied to IPMC is identified by fitting a linear model to the data collected from simulating non-linear dynamic system. Figure 6.3 shows the

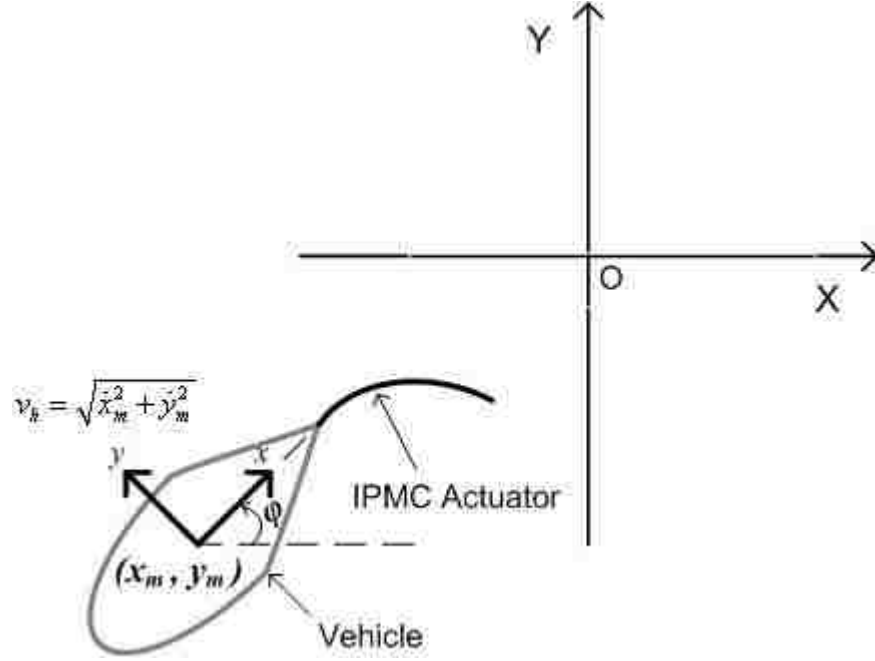


Figure 6.2: Definition of the output variables

speed of the vehicle for 2.5 and 3.5 *volts* amplitude of the sinusoidal wave applied to the actuator. It should be noted that the bias is set to zero in this simulation. The respective linear models,  $(G_{11})^{2.5}$  and  $(G_{11})^{3.5}$ , identified using MATLAB System Identification Toolbox (V 7.4.0)[52], are given by the following equations

$$(G_{11})^{2.5} = \frac{V(s)}{A(s)} = \frac{0.002176}{12.3s^2 + 7.8955s + 1} \quad (6.1)$$

$$(G_{11})^{3.5} = \frac{V(s)}{A(s)} = \frac{0.0023827}{0.005s^2 + 5.03s + 1} \quad (6.2)$$

From the above equations, the steady state gain corresponding to 2.5 *volts* of amplitude is 0.002176 and that of 3.5 *volts* is 0.0023827. As the gains are close to each other, linear model assumption is valid in steady state and therefore, the identified

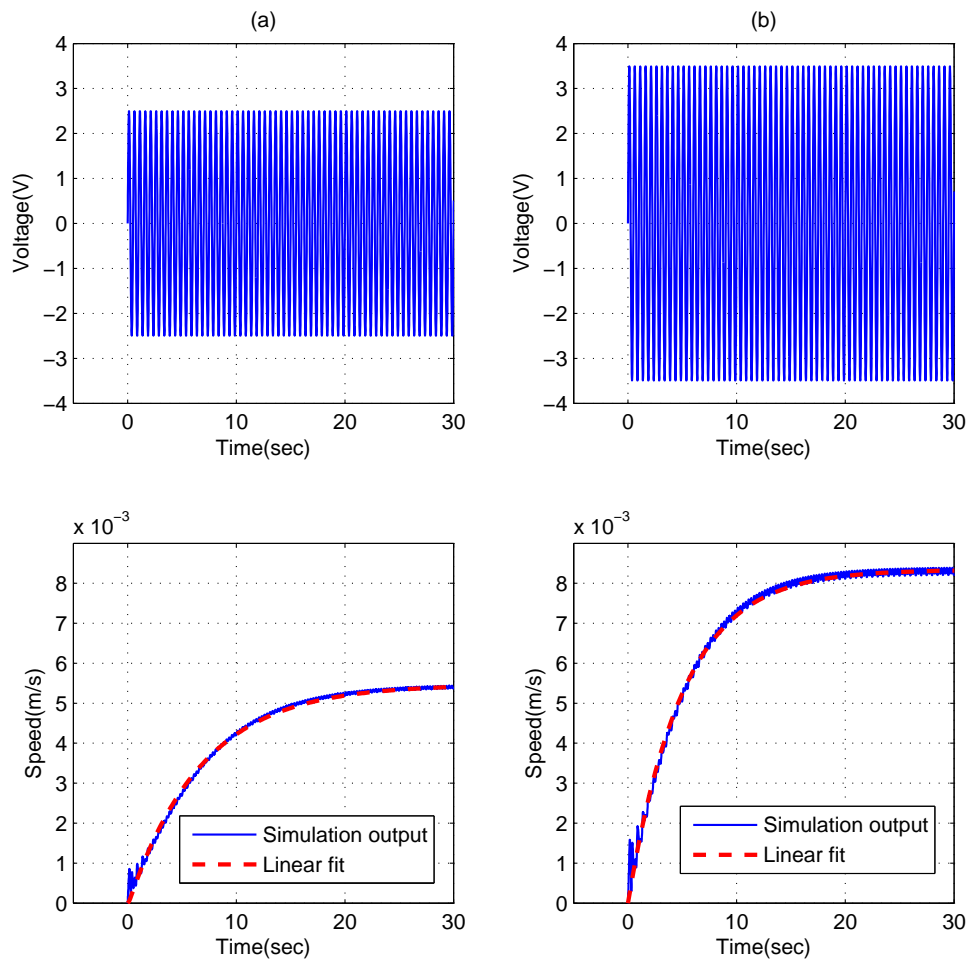


Figure 6.3: Speed of the vehicle with sinusoidal input of 2.5 and 3.5 volts amplitude

linear model can be used in controller design.

### 6.1.2 Bias and speed model identification

A sudden change in bias,  $B(t)$  in the input voltage applied to the IPMC actuator causes the actuator to oscillate assymmetrically about the vertical plane passing through chord of the vehicle. These asymmetric oscillations result in small perturbations

in the thrust force due to interaction of the fin with water as shown in Fig. 6.4, which leads to the perturbation of the vehicle speed as shown in Fig. 6.5. It's also observed that there is a little influence of bias on the mean speed of the vehicle. The transfer function,  $G_{12}$ , relating the bias and the change in vehicle speed is given by the following equation:

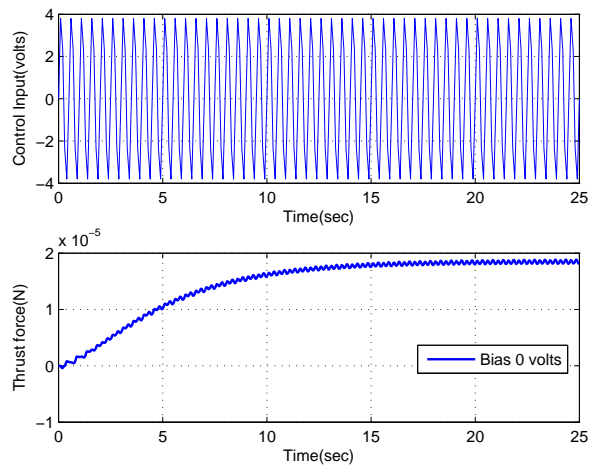
$$G_{12} = \frac{V(s)}{B(s)} = \frac{-0.00094248s}{s^2 + 0.5s + 0.3948} \quad (6.3)$$

Using the final value theorem, it can be shown that the steady state speed due to a step change of the bias voltage,  $B$ , becomes zero :

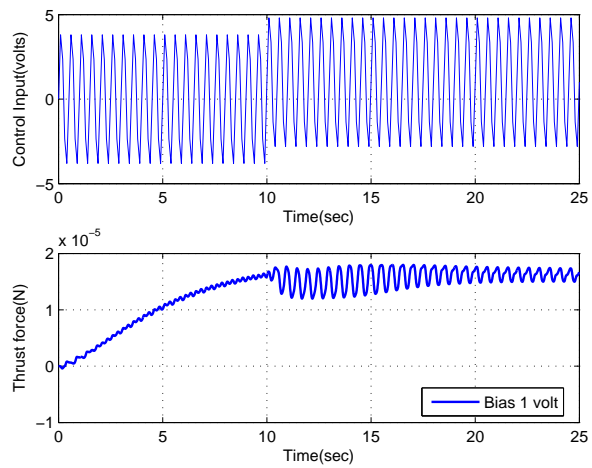
$$V_{ss} = \lim_{s \rightarrow 0} sG_{12} \frac{B}{s} = 0 \quad (6.4)$$

### 6.1.3 Bias and heading angle model identification

The direction of the vehicle can be controlled by controlling the heading angle  $\phi(t)$ , of the vehicle. Figure 6.6 shows the change in heading angle when the input voltages with bias of 0.5 volts and 1 volt are applied to the IPMC actuator. In both the cases, amplitude of the sinusoidal voltage applied to IPMC is kept constant at *3volts*. A step change in bias of the input voltage applied to the IPMC generates a moment about the vertical axis passing through the center of mass of the vehicle and changes the orientation of the vehicle. As shown in Fig. 6.6, due to a constant moment acting



(a) Thrust force without bias in input voltage.

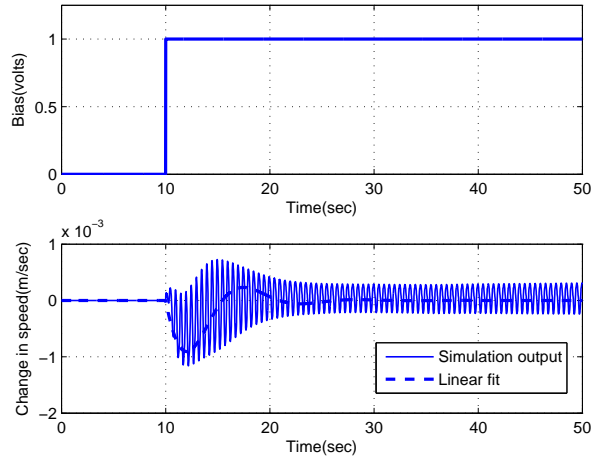


(b) Thrust force with bias in input voltage.

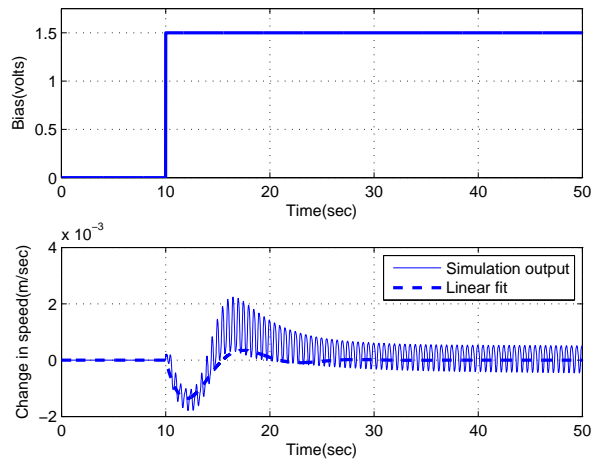
Figure 6.4: Thrust force variation due to bias in the input voltage.

on the vehicle, heading angle of the non-linear dynamic model maintains constant slope in steady state. Using MATLAB System Identification Toolbox (V 7.4.0),[52], the linear model identified between unit change in bias and the corresponding change





(a) Change in speed with unit step change in bias.



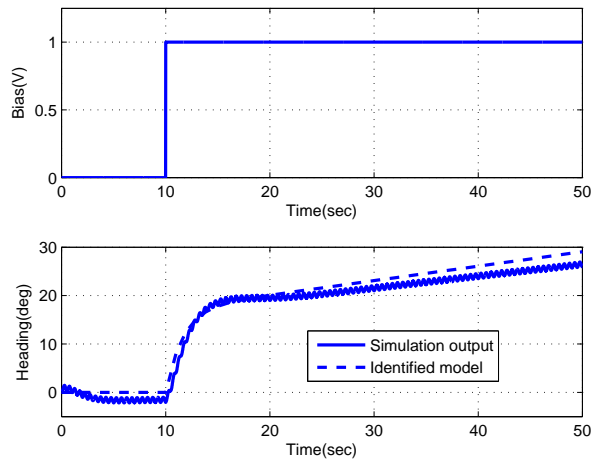
(b) Change in speed with 0.5 volts step change in bias.

Figure 6.5: Change in speed due to bias in input voltage.

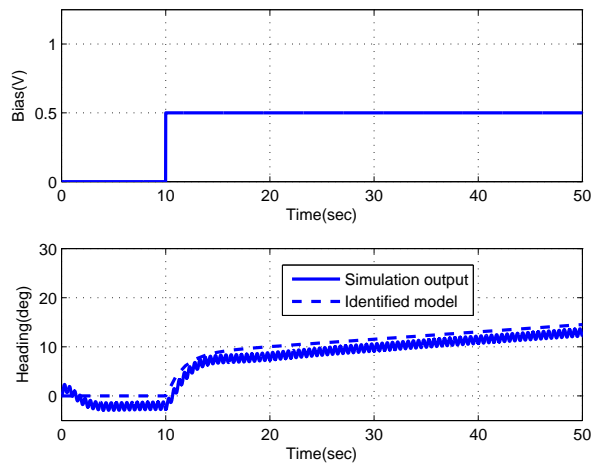
in heading angle is expressed as:

$$G_{22} = \frac{\phi(s)}{B(s)} = \frac{(0.1098s + 0.03278)}{s^2 + 0.5738s + 0.08212} \quad (6.5)$$

The identified linear model of 6.5 is validated by applying bias of 0.5 volt and



(a) 1 volt bias in voltage input.



(b) 0.5 volt bias in voltage input.

Figure 6.6: Change in heading angle due to change in bias of input voltage.

comparing the output with the heading angle of the nonlinear model as shown in Fig. 6.6(b). From Fig. 6.6(b), there is a little overshoot in the output of the linear model when compared to the output of the nonlinear model.

## 6.2 Non-interacting closed loop control

As discussed in section 6.1, there are interactions between the controlled variables,  $V_h(t)$  and  $\phi(t)$  and the control input parameters,  $A(t)$  and  $B(t)$  due to the coupled nature of the dynamic model. Using the transfer functions obtained in section 6.1, the dynamic model can be represented using transfer function matrix,  $G$  as

$$\begin{bmatrix} v_h(s) \\ \phi(s) \end{bmatrix} = \begin{bmatrix} G_{11} & G_{12} \\ 0 & G_{22} \end{bmatrix} \begin{bmatrix} A(s) \\ B(s) \end{bmatrix} \triangleq \mathbf{y}=\mathbf{G}\mathbf{u} \quad (6.6)$$

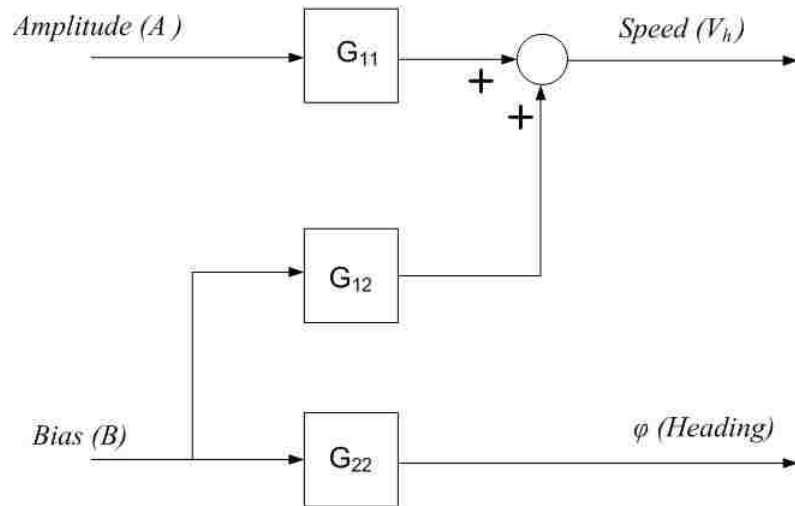


Figure 6.7: Identified plant block diagram

As shown in Fig. 6.8, the objective of the decoupling control design is to select controller transfer functions,  $d_{11}, d_{21}, d_{12}, d_{22}$  that eliminate the interaction effects and ensure that the closed loop response follow the desired relationship,  $Q$  [65]. Using

Fig. 6.8, the controller transfer function can be written as:

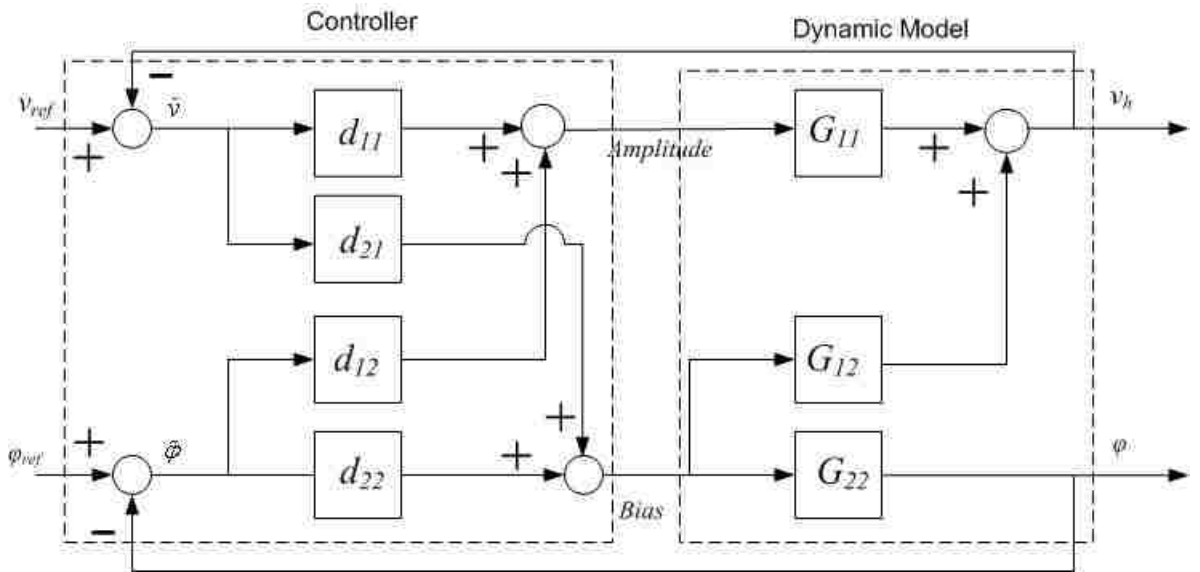


Figure 6.8: Plant with decoupling controller

$$u = De \tag{6.7}$$

where,  $u = [A(s) \ B(s)]^T$ ,  $D$  is a  $2 \times 2$  controller transfer function matrix to be determined and  $e$  is tracking error vector expressed as:

$$e = r - y \tag{6.8}$$

where,  $r = [V_{ref} \ \phi_{ref}]^T$  and  $y = [v_h \ \phi]^T$ . From equations 6.6, 6.7 and 6.8, and

solving for  $\mathbf{y}$ , we get:

$$\mathbf{y} = (1 + \mathbf{GD})^{-1}\mathbf{GD}\mathbf{r} \quad (6.9)$$

where,  $(1 + \mathbf{GD})^{-1}\mathbf{GD}$  becomes closed loop transfer function matrix. For the effective control of a vehicle speed and a heading angle, the desired closed loop transfer function matrix,  $\mathbf{Q}$ , can be defined as:

$$\mathbf{y} = \mathbf{Q}\mathbf{r} \quad (6.10)$$

where,

$$\mathbf{Q} = \begin{bmatrix} q_{11} & 0 \\ 0 & q_{22} \end{bmatrix} \quad (6.11)$$

where off diagonal terms are set to zero for the decoupled control of speed and a heading angle. Comparing Equations 6.9 and 6.10, we get:

$$\mathbf{Q} = (1 + \mathbf{GD})^{-1}\mathbf{GD} \quad (6.12)$$

Solving the Equation 6.12 for  $\mathbf{D}$ , the controller transfer function matrix can be expressed as:

$$\mathbf{D} = \mathbf{G}^{-1}\mathbf{Q}(\mathbf{I} - \mathbf{Q})^{-1} \quad (6.13)$$

The individual transfer functions of the controller transfer function matrix,  $\mathbf{D}$  can be

expressed as:

$$\begin{aligned}
 d_{11} &= \frac{G_{22}q_{11}}{\Delta(1 - q_{11})} \\
 d_{12} &= \frac{-G_{12}q_{22}}{\Delta(1 - q_{22})} \\
 d_{21} &= 0 \\
 d_{22} &= \frac{G_{11}q_{22}}{\Delta(1 - q_{22})}
 \end{aligned} \tag{6.14}$$

where  $\Delta = G_{11}G_{22}$

### 6.3 Simulation Results

To validate the designed controller, simulations are conducted by applying the designed controller to the non linear dynamic model developed in chapter 4. The closed loop block diagram of decoupling controller and the dynamic model is shown in Fig. 6.9. MATLAB/Simulink tools are used to simulate the dynamics (including decoupling control) of the system. The controller transfer functions namely,  $d_{11}, d_{12}, d_{21}, d_{22}$  are found by selecting the desired closed loop transfer functions  $q_{11}$  and  $q_{22}$ .

Using equation 6.14, after substituting the plant transfer functions given by equations 6.1, 6.4 and 6.5 and the desired closed loop transfer functions,  $q_{11}$  and  $q_{22}$ , the resulting controller transfer functions are expressed as:

$$d_{ij} = \frac{b_m s^m + \dots + b_1 s + b_0}{a_n s^n + \dots + a_1 s + a_0} \quad i, j = 1, 2 \tag{6.15}$$

Then, in order to have the output of equation 6.15 bounded at high frequencies,

the transfer functions  $d_{ij}$  need to be in the *proper* form. And the equation 6.15 is said to be in proper form when  $m \leq n$ . In equation 6.14, as the order of the plant transfer functions are known, the *minimum* order of the desired closed loop transfer functions,  $q_{11}$  and  $q_{22}$  yielding *proper* controller transfer functions is found to be 2.  $\therefore$  The desired closed loop transfer functions are selected are in the form of:

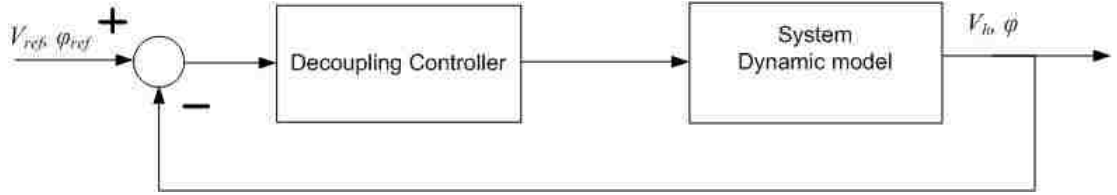


Figure 6.9: Non-linear plant with decoupling controller

$$q_{11} = q_{22} = \frac{\omega_n^2}{s^2 + 2\zeta\omega_n s + \omega_n^2} \quad (6.16)$$

where, damping ratio,  $\zeta$  and natural frequency,  $\omega_n$  are selected based on the design requirement for tracking speed and heading angle . For the desired closed loop transfer functions of:

$$q_{11} = q_{22} = \frac{\omega_{nd}^2}{s^2 + 2\zeta_d\omega_{nd}s + \omega_{nd}^2} \quad (6.17)$$

where  $\omega_{nd}^2 = 2$  and  $\zeta_d = 1$ , we can determine the controller transfer functions using

equations 6.1, 6.4, 6.5, 6.17 and 6.14 as:

$$\begin{aligned}
d_{11} &= \frac{2(12.3s^2 + 7.89s + 1)}{0.002176(s^2 + 2\sqrt{(2)}s)} \\
d_{12} &= 2 \left( \frac{0.009425}{0.002176} \right) \left( \frac{s^2 + 0.5738s + 0.08212}{s^2 + 0.5s + 0.3948} \right) \left( \frac{12.3s^2 + 7.89s + 1}{0.1098s^2 + 0.3433s + 0.9271} \right) \\
d_{21} &= 0 \\
d_{22} &= 2 \frac{s^2 + 0.5738s + 0.08212}{(0.1098s + 0.03278)(s^2 + 2\sqrt{(2)}s)}
\end{aligned} \tag{6.18}$$

Using the controller transfer function given in 6.18, simulations are conducted for the tracking reference speed of  $5e^{-03}m/sec$  and the reference heading angle of  $0^\circ$ . Figure 6.10(a) shows the simulation results for tracking  $5e^{-03}m/sec$  command speed. Because of the limit imposed on the maximum amplitude (i.e.  $\pm 4$  volts) applied to the IPMC actuator, there is an error in following the desired output for  $t = 5sec$  as shown in Fig 6.10(a). After  $t = 5sec$ , the error observed in tracking speed can be attributed to the fact that the decoupling controller is designed using identified linear model. Similarly, as shown in the Fig. 6.10(b) the initial tracking error in heading angle is also due to limit imposed on the bias applied (i.e.  $\pm 0.5$  volts). Figure 6.11 shows the simulation results for tracking  $5e^{-03}m/sec$  reference speed with  $10^\circ$  orientation change at  $t = 15sec$ . From Fig. 6.11, it is apparent that the interaction between change in bias and vehicle speed is not totally decoupled. Therefore, the performance of the decoupling controller designed using linear model is limited when applied to original non-linear plant.



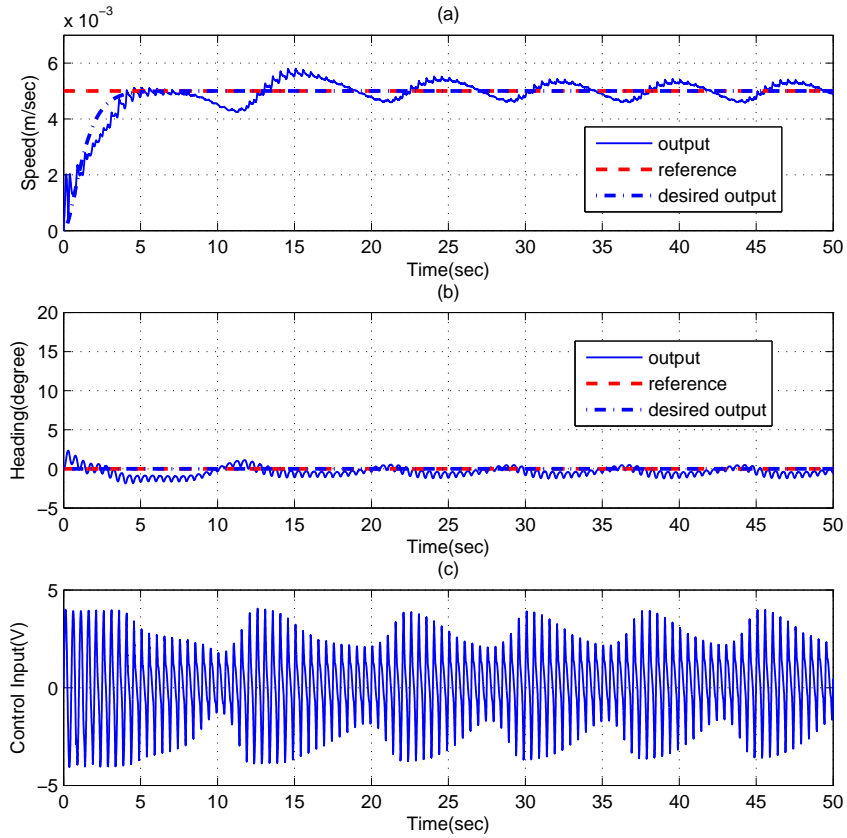


Figure 6.10: Tracking  $5e^{-3}$  m/sec speed and  $0^\circ$  heading with non-linear dynamic model

#### 6.4 Proposed experimental setup for validating the designed controller

An experiment, as shown in Fig. 6.12, is planned for tracking speed and heading angle of the vehicle using the decoupling controller. As shown in Fig. 6.12 and 6.13, a Basler digital camera is used for recording the current position the vehicle by capturing two LEDs mounted on the top of the vehicle. The image data is transferred to PC and processed for vehicle's position and orientation using MATLAB Image Acquisition toolbox. Depending on the tracking error,  $\mathbf{e}$ , the control signal generated by the

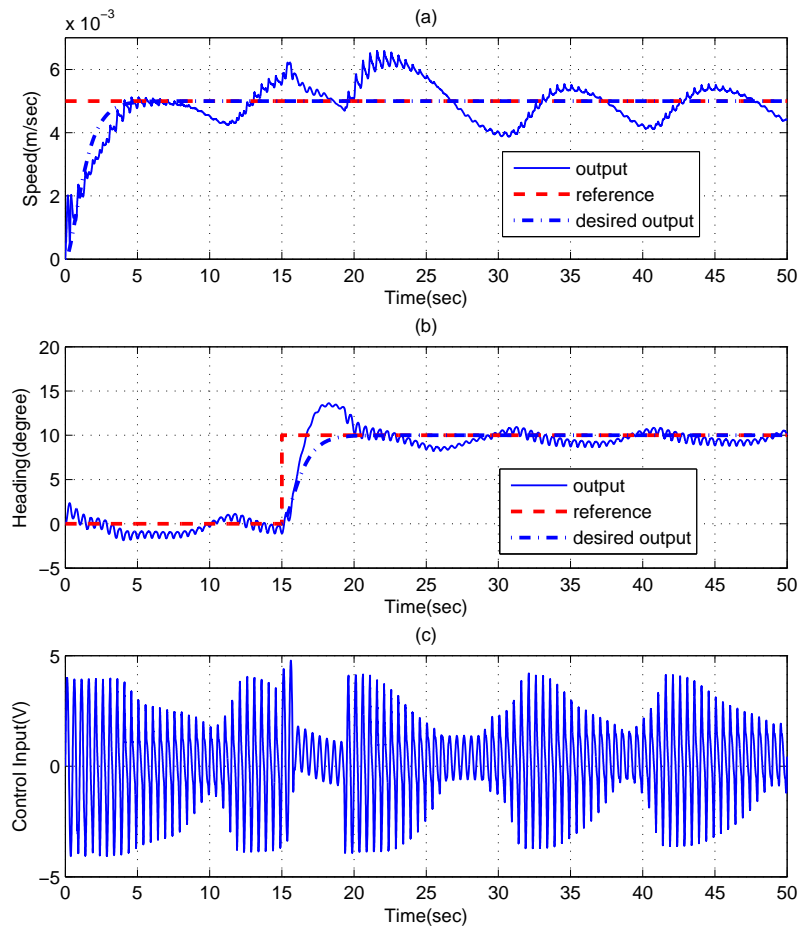


Figure 6.11: Tracking  $5e^{-3}$  m/sec speed and  $10^\circ$  heading with non-linear dynamic model

decoupling controller is transmitted to the vehicle through wireless communication.

## 6.5 Summary

In this chapter, a decoupling control algorithm was developed for controlling the speed and heading angle of the IPMC propelled vehicle. Simulation data of non-linear dynamic model was used for identifying the relation between input and output

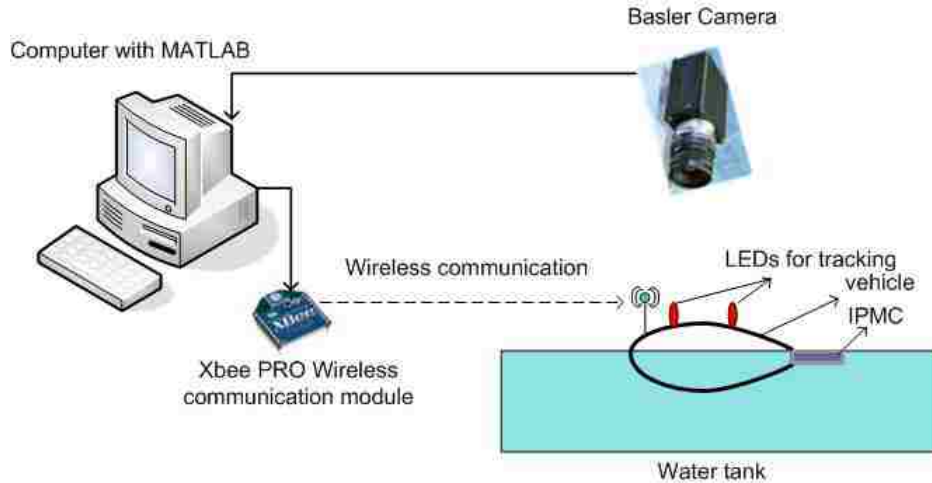


Figure 6.12: Experimental setup for closed-loop control of IPMC propelled vehicle

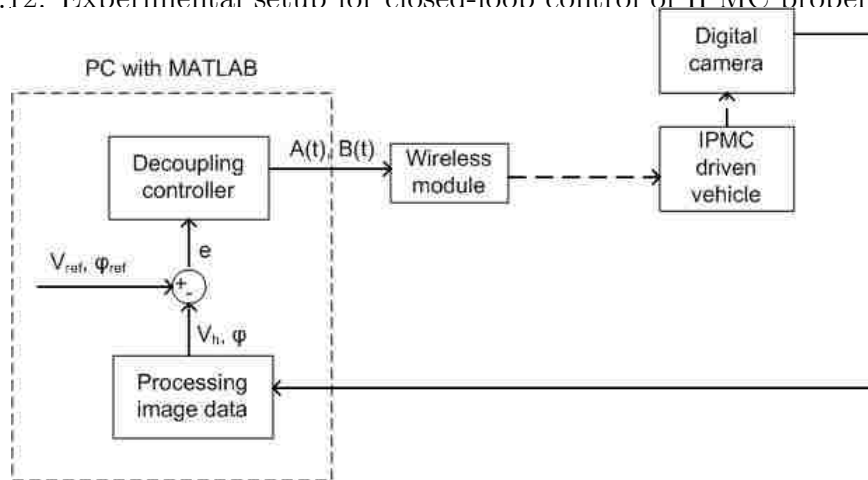


Figure 6.13: Block diagram of closed-loop control of the IPMC propelled vehicle

variables. Using the desired closed-loop transfer function eliminating interaction, decoupling controller transfer functions were obtained. To validate the desired controller, simulations were conducted using the original non-linear plant. The designed controller was able to track the reference speed and heading angle with relatively large settling time. This can be attributed to the fact that, for a non-linear plant, identified linear models were used in controller design.

## CHAPTER 7

### PATH PLANNING AND CONTROL

In this chapter, trajectory planning and control of an IPMC driven underwater vehicle within obstacles is discussed. The presented work is divided into kinematic path planning and trajectory control sections. In the kinematic path planning phase, the vehicle is approximated by a rectangle that encloses the largest deformation of the oscillating IPMC actuator. Obstacles are approximated by polygonal shapes that approximate their actual dimensions. To simplify the problem of collision detection, vehicle is shrunk to a line while obstacles are expanded by a half width of the rectangle representing the vehicle. Path planning problem is formulated as a nonlinear programming problem that minimizes the error between current and goal configurations of the vehicle. The objective function combines the distance to target and the orientation of the vehicle. A penalty term is added to the objective function to ensure that the vehicle is not colliding with obstacles. The obtained path is discretized with respect to time, and controlled simultaneously for the yaw angle and speed of the vehicle using the controllers designed in chapter 5.

## 7.1 Path Planning

The objective of path planning problem for the IPMC driven vehicle is to find an obstacle free path when the goal position and orientation is known a priori. Two factors should be considered due the type of propulsion and the size of the vehicle:

- The vehicle cannot swim back wards
- The turning radius of the vehicle is relatively large i.e. vehicle cannot make sharp turns.

In the proposed approach, a search is performed at each step to determine the orientation of the vehicle that moves it closer to the target with the desired orientation without colliding with obstacles. The vehicle is then advanced in that direction for a certain length. Penalty terms representing the relation between the path and the edges of the obstacles are added to the objective function of the optimization problem[66]. Once the obstacle-free path is obtained, it is discretized in terms of time to generate the reference speed required to follow desired trajectory.

### 7.1.1 Representation of workspace

Simplification of the path planning process can be summarized into two steps. First, the vehicle is approximated by a rectangle enclosing the head and the largest wave of the IPMC actuator. Next, vehicle is shrunk to a line while simultaneously expanding the obstacles in all directions by a distance equal to half of the vehicle's width as shown in Fig. 7.1[66, 67]. Obstacles are approximated to polygonal shapes



minimizes the objective function value. The vehicle is advanced in that direction through a limited distance,  $\Delta R$ . The process is repeated at step  $k+1$  until the target is reached. The optimization problem can be formulated as:

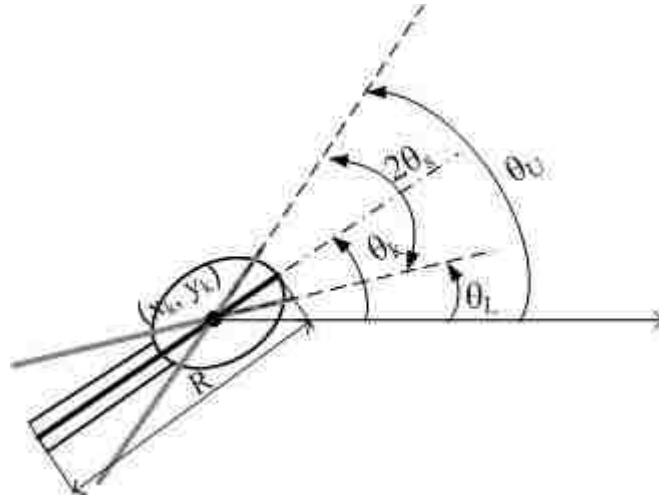


Figure 7.2: Schematics of the vehicle search in angular direction at  $k^{th}$  time step

$$\text{Find } \Delta\theta_k \text{ that minimizes } f \quad (7.1)$$

The change of orientation is subject to the constraints,  $-\theta_s \leq \Delta\theta_s \leq \theta_s$ .

The objective function is formed using a strategy similar to the one used in the car parking problem. At the beginning, the main objective is to minimize the distance between the current and goal locations,  $D$ . The relation between the orientation of the vehicle and the final orientation is not a paramount factor. Once the car is close to the parking spot, a different strategy is adopted that emphasizes aligning the vehicle

with the target orientation while simultaneously reducing the distance to it. Based on this discussion, the proposed algorithm can be described as follows:

- The vehicle is far from the goal configuration ( $D > \Delta L$ )

At this stage, the vehicle is farther than a pre-defined distance defining nearness of the vehicle,  $L$ . It is desired to find the orientation that minimizes an objective function given by

$$f(\Delta\theta_k) = w_1 \left( \frac{(x_k - x_g)^2 + (y_k - y_g)^2}{L_g^2} \right) + w_1 \left( \frac{(x_{k1} - x_g)^2 + (y_{k1} - y_g)^2}{L_g^2} \right) \quad (7.2)$$

In addition to finding the orientation of the vehicle with minimum function value, it is necessary to detect and avoid obstacles in the path of the vehicle. Because vehicle is represented as line segment and each edge of a polygon shaped object is also a line segment, intersection between the two line segments can be treated as collision. As shown in[66] intersection between two lines is defined using the parametric values,  $u$  and  $v$ , of the line representing vehicle and and edge of an obstacle respectively. Therefore, a measure for the severity of the collision between the vehicle and edge  $j$  of obstacle  $i$  is given by:

$$t_{ij} = uu.vv \quad (7.3)$$

where



$$\begin{aligned}
uu &= u + 1 & \text{if } 0 \leq u \leq 0.5 \\
uu &= 2 - u & \text{if } 0.5 \leq u \leq 1 \\
uu &= 0 & \text{if } u \leq 0 \text{ or } u \geq 1 \\
vv &= v + 1 & \text{if } 0 \leq v \leq 0.5 \\
vv &= 2 - v & \text{if } 0.5 \leq v \leq 1 \\
vv &= 0 & \text{if } v \leq 0 \text{ or } v \geq 1
\end{aligned} \tag{7.4}$$

Using Equations 7.2 and 7.3, orientation of the vehicle that minimizes the distance between current and goal configurations and avoids the collision between the obstacles is given by:

$$f(\Delta\theta_k) = w_1 \left( \frac{(x_k - x_g)^2 + (y_k - y_g)^2}{L_g^2} \right) + w_1 \left( \frac{(x_{k1} - x_g)^2 + (y_{k1} - y_g)^2}{L_g^2} \right) + w_2 \max(t_{ij}) \tag{7.5}$$

The first two terms in the above equation represent the normalized distance between the center of mass and tail of the vehicle at the  $k^{th}$  iteration and the goal position respectively. The  $G1-G$  vector determines the final orientation of the vehicle. To balance the objectives of Equation 7.5, it is recommended to select  $w_1$  and  $w_2$  such that  $w_1 \gg w_2$  to ensure that the algorithm does not terminate before the second objective function is activated.

- The vehicle is near the goal configuration ( $D < \Delta L$ )

One more term is added to Equation 7.5, to help orient the vehicle towards the goal

configuration. This term calculates the normalized error of the vehicle orientation,  $\theta_k + \Delta\theta_k$  with respect to the orientation of the vehicle at the goal configuration,  $\theta_G$ . If  $\theta_G$  is zero, a small value,  $\delta\theta$ , is added to the denominator of the last term of the objective function. If we do not consider the  $\theta_v$  term, the vehicle will try to orient itself parallel to the goal configuration rather than reaching actual target orientation.

$$\begin{aligned}
f(\Delta\theta_k) = & w_1 \left( \frac{(x_k - x_g)^2 + (y_k - y_g)^2}{L_g^2} \right) \\
& + w_1 \left( \frac{(x_{k1} - x_{g1})^2 + (y_{k1} - y_{g1})^2}{L_g^2} \right) + w_2 \max(t_{ij}) \\
& + w_3 \left( \frac{L_g - D}{L_g} \right) \left( \frac{(\theta_k + \Delta\theta_k) - \theta_G}{\theta_G} + \frac{(\theta_k + \Delta\theta_k) - \theta_v}{\theta_G} \right)
\end{aligned} \tag{7.6}$$

Using the position and orientation data obtained from the path planning algorithm, reference speed and yaw angle are calculated by discretizing the path using a suitable time scale

## 7.2 Illustrative Example

### 7.2.1 Path planning

The objective of this section is to verify the proposed algorithm. A workspace with four polygonal obstacles is selected as shown in Fig. 7.3. Parameters used in implementing the algorithm are given in Table 7.1.

The obstacle- free path generated by the algorithm of the previous section is shown in Fig. 7.4. Enlarged image shows that path is not intersecting obstacle. It can be seen that the path mostly follows the Euclidean norm except when it interferes

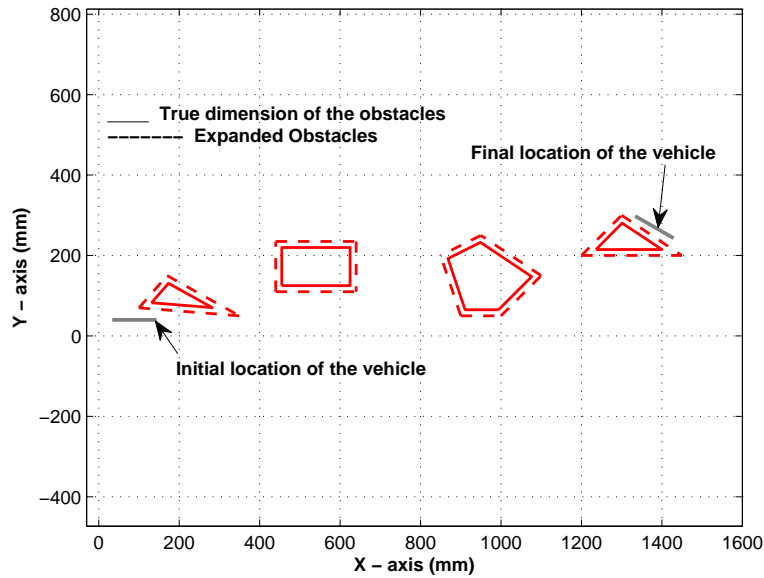


Figure 7.3: Work space used in simulation

with obstacles. In these cases the path is diverted close to vertices of the expanded obstacles. Once the second objective function is activated, the vehicle is oriented toward the target. In this example, a time span of 300 sec is used for discretizing the data. This value is selected based on the observed performance of the actuator. Figure 7.5(a) shows the reference speed and orientation (yaw) generated using the data from path planning. A steady speed is used for most of the path except at the beginning and end of the motion. Figure 7.5(b) that initially the vehicle is oriented toward the target. However, the risk of collision with the first obstacle results in switching the orientation closer to zero, which remains relatively unchanged, until the vehicle passes the first obstacle. After that, the path is oriented again toward the target except for a slight adjustment when the vehicle passes close to the second

Table 7.1: Parameters used in simulation

Variable	Value
$R(\text{m})$	0.110
$w(\text{m})$	0.014
$w_1$	100
$w_2$	10
$w_3$	1
$x_G, y_G(\text{m})$	(1.40, 0.260)
$x_1, y_1(\text{m})$	(.110, 0.040)
$\Delta L(\text{m})$	0.075
$\Delta R(\text{m})$	0.005
$\theta_1(\text{degree})$	0
$\theta_g(\text{degree})$	-30

obstacle. A sharp change of orientation is necessary to avoid collision with the third obstacle (around time = 170 s). Orientation is adjusted toward the target after this obstacle. The last major changes of the vehicle orientation are due to the need to avoid collision with the last obstacle and to orient the vehicle toward the final orientation.

### 7.2.2 Tracking control

The feedback control algorithm developed in chapter 5 is used to ensure that the oscillatory vehicle follows the path created in the last example. The dimensions of the vehicle and the parameters of the IPMC used in the simulations are given in Table 4.1 and Table 4.2 respectively. Figure 7.6 shows the path generated when controlling the vehicle using the proportional and integral gain values of chapter 5. Figure 7.7 shows the results for tracking the speed and orientation as well as the voltage signal to the IPMC actuator. The results of Fig. 7.6 and Fig. 7.7(b) show

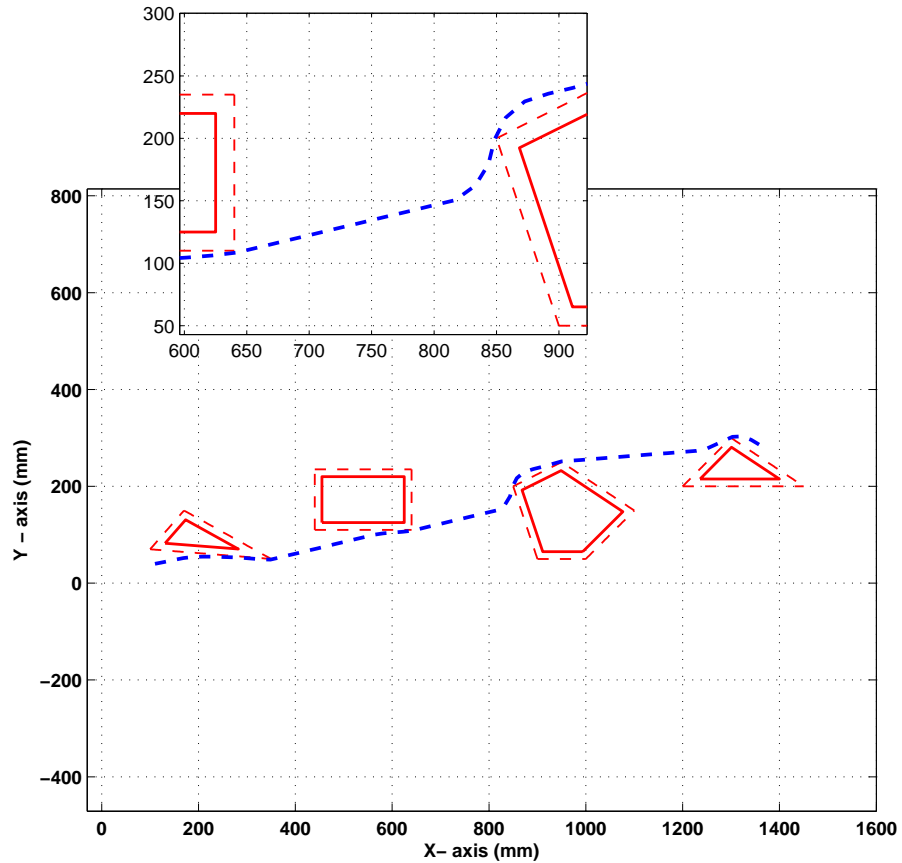


Figure 7.4: Path generated by the algorithm

that the actual path does not significantly deviate from the one obtained from the path planning algorithm. The biggest deviations from the reference path occur after passing the second obstacle. This phase, which continues until the vehicle passes the third obstacle, is associated with speed oscillations, Fig. 7.7(a). The speed increase around 170 seconds is associated with need to rapidly adjust the orientation of the vehicle to avoid collision with the third obstacle. Figure 7.7(c) indicates that the voltage magnitude to the IPMC actuator remains steady except during the maneuver

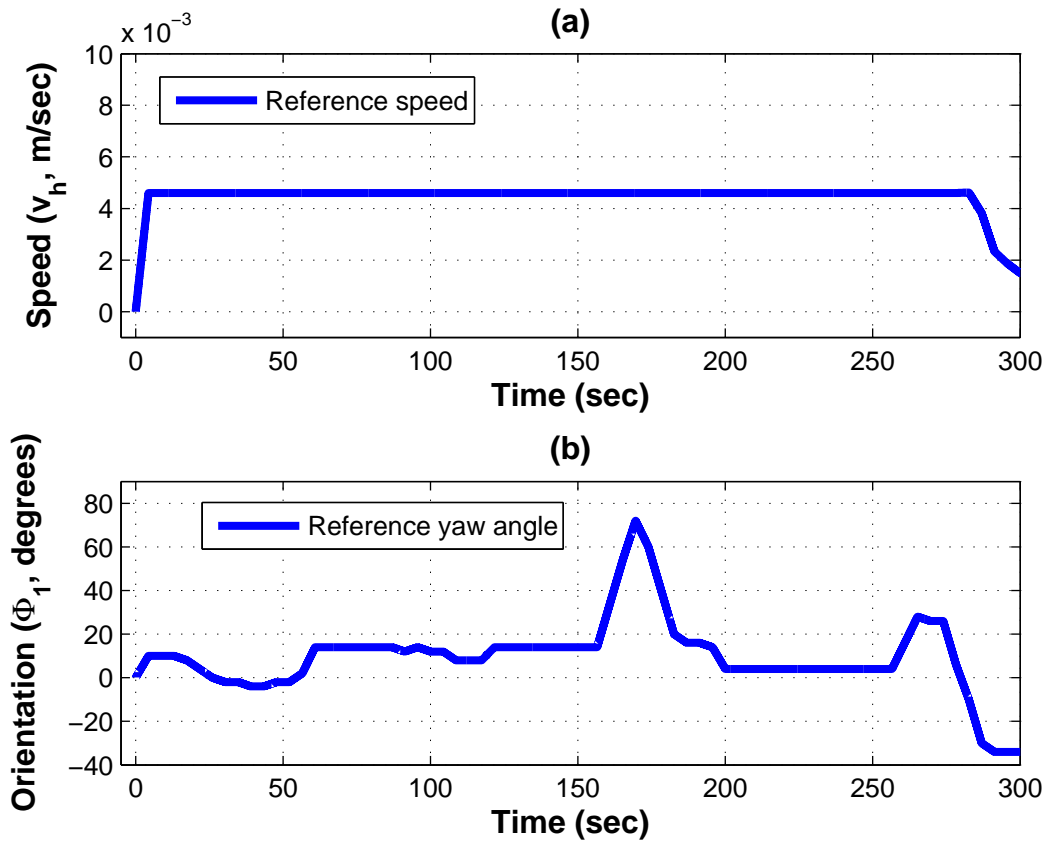


Figure 7.5: Discretized speed and orientation values for the example of Fig. 7.4

around 170 seconds.

### 7.3 Summary

This chapter presented an algorithm for path planning of underwater vehicle driven by an IPMC actuator. In the proposed control scheme, the trajectory of the vehicle is controlled by tracking the yaw angle (orientation) and speed of the vehicle, which is driven by applying a sinusoidal voltage with a bias to the IPMC actuator to induce oscillatory motion. A PI controller developed in chapter 5 is used

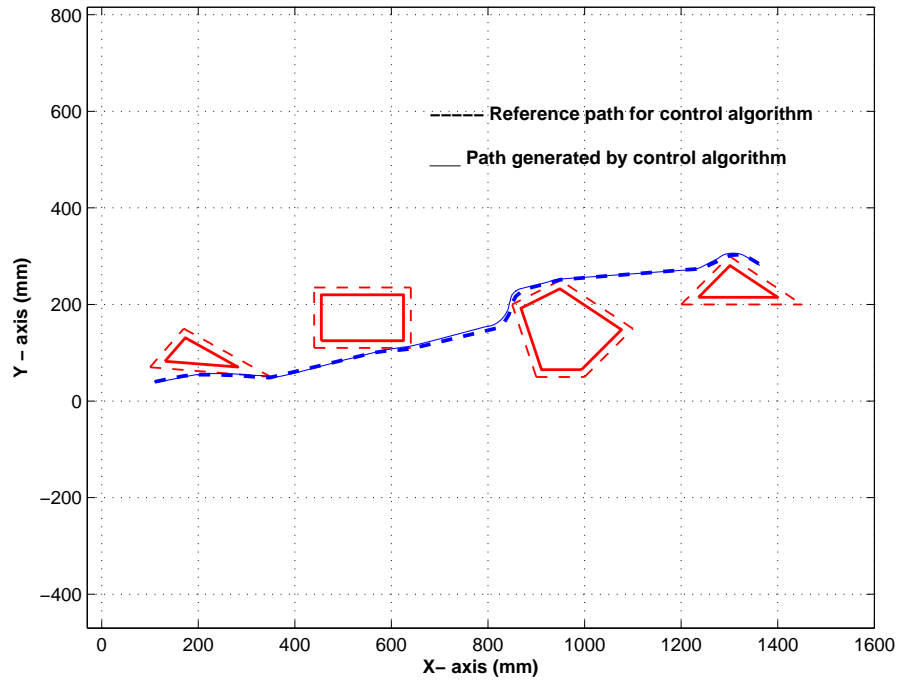


Figure 7.6: Comparison of path planning and trajectory control results for the example of Fig. 7.4

to control the speed of the vehicle. The vehicle is modeled as rectangle and obstacles are approximated by polygons approximating actual dimension. To simplify the path planning problem, vehicle is shrunk to line while obstacles are expanded by half the width of rectangle enclosing the vehicle. Path planning is formulated as nonlinear optimization problem. Depending on the distance to the target, two objective functions are used to minimize the distance between current and goal locations and the error in orientation of the vehicle with respect to the goal orientation. Penalty term is added to represent the collision with the obstacles. Simulation results are presented to validate the proposed path planning algorithm and trajectory control.

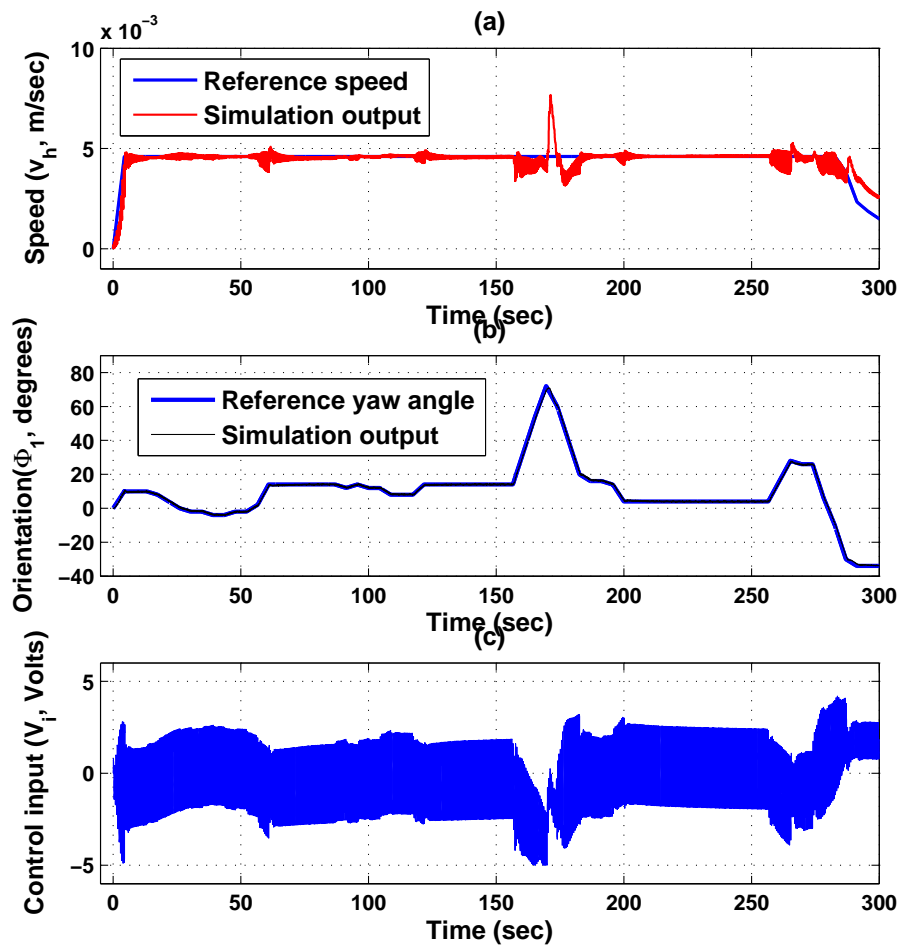


Figure 7.7: Simulation results for following the discretized speed and orientation values for the example of Fig. 7.4



## CHAPTER 8

### MODEL REFERENCE ADAPTIVE CONTROL ALGORITHM

In this chapter model reference adaptive control (MRAC) is derived for the identified underwater vehicle propelled by the Ionic polymer metal composite (IPMC) actuator. Trajectories of the vehicle are controlled by simultaneously controlling the bias and amplitude of the sinusoidal voltage applied to the IPMC actuator attached at the rear end of the vehicle. It is assumed that the system parameters as well as high frequency gain matrix are unknown. Using Lyapunov stability theory and factorization of the high frequency gain matrix, an adaptive output feedback control is designed for trajectory control of a heading angle and a speed of the vehicle. In the proposed approach, SDU (Square Diagonal and Upper triangular matrix) decomposition of the high frequency gain (HFG) matrix is used. Only signs of the leading principle minors of the HFG matrix are assumed to be known. Simulation results are presented to show that precise trajectory control of the heading and speed is achieved in spite of the coupling between controlled variables.

## 8.1 Vehicle dynamic model

From chapter 6,  $2 \times 2$  transfer function matrix relating inputs,  $\mathbf{u} = [ A(s) \quad B(s) ]^T$ , and outputs  $\mathbf{y} = [ v(s) \quad \phi(s) ]^T$  is given by the following equation:

$$\begin{bmatrix} V_h(s) \\ \phi(s) \end{bmatrix} = \begin{bmatrix} G_{11} & G_{12} \\ 0 & G_{22} \end{bmatrix} \begin{bmatrix} A(s) \\ B(s) \end{bmatrix} \triangleq \mathbf{y} = \mathbf{G}\mathbf{u} \quad (8.1)$$

where,

$$G_{11}(s) = \frac{V(s)}{A(s)} = \frac{0.002176}{12.3s^2 + 7.8955s + 1} \quad (8.2)$$

$$G_{12}(s) = \frac{V(s)}{B(s)} = \frac{-0.00094248s}{s^2 + 0.5s + 0.3948} \quad (8.3)$$

$$G_{22}(s) = \frac{\phi(s)}{B(s)} = \frac{(0.1098s + 0.03278)}{s^2 + 0.5738s + 0.08212} \quad (8.4)$$

The minimal realization (i.e. no uncontrollable and unobservable states) of the above transfer function can be expressed as:

$$\begin{aligned} \dot{X} &= A_p X + B_p \mathbf{u} \\ \mathbf{y} &= C_p X \end{aligned} \quad (8.5)$$

where,  $X \in \mathfrak{R}^6$  is state vector and  $A_p \in \mathfrak{R}^{6 \times 6}$ ,  $B_p \in \mathfrak{R}^{6 \times 2}$  and  $C_p \in \mathfrak{R}^{2 \times 6}$  are system

matrices expressed as:

$$\begin{aligned}
 A_p &= \begin{bmatrix} -1006 & -12.5 & 0 & 0 & 0 & 0 \\ 160 & 0 & 0 & 0 & 0 & 0 \\ 0 & 0 & -0.5 & -0.789 & 0 & 0 \\ 0 & 0 & 0.5 & 0 & 0 & 0 \\ 0 & 0 & 0 & 0 & -0.611 & -0.0133 \\ 0 & 0 & 0 & 0 & 0.015 & 0 \end{bmatrix} \\
 B_p &= \begin{bmatrix} 4 & 0 \\ 0 & 0 \\ 0 & 1 \\ 0 & 0 \\ 0 & 4 \\ 0 & 0 \end{bmatrix} \\
 C_p &= \begin{bmatrix} 0 & 6.8012 & -0.942 & 0 & 0 & 0 \\ 0 & 0 & 0 & 0 & 2.8332 & 3.6792 \end{bmatrix}
 \end{aligned} \tag{8.6}$$

The LTI model represented using equations 8.1 and 8.5 hold the following properties:

- Transmission zeros  $G(s)$  have negative real part.
- $G(s)$  has full rank, 6.
- The observability index [68, 69] is defined as the smallest integer,  $\nu$  ( $1 \leq \nu \leq 6$ ) such that  $O_\nu = [C_p^T \ (A_p C_p)^T \ \dots \ (A_p^{\nu-1} C_p)^T]^T$  has full rank, 6. For the given

system matrices  $A_p, C_p$ , observability matrix  $O_\nu$ ,

$$O_\nu = \begin{bmatrix} 0 & 6.8013 & -0.9424 & 0 & 0 & 0 \\ 0 & 0 & 0 & 0 & 2.833 & 3.0793 \\ 108.82 & 0 & 0.4712 & 0.7441 & 0 & 0 \\ 0 & 0 & 0 & 0 & -1.6846 & -0.0377 \\ -1.09e^5 & -1.36e^3 & 0.1364 & -0.3742 & 0 & 0 \\ 0 & 0 & 0 & 0 & -0.63 & -0.0137 \end{bmatrix} \quad (8.7)$$

has full rank for  $\nu = 4$ . Therefore the observability index of  $G(s)$  is 4.

- $\det(C_p B_p) = 0$  and  $\det(C_p A_p B_p) \neq 0$ . Therefore  $G(s)$  has relative degree 2 and  $B_o = C_p A_p B_p$  referred as high frequency gain matrix.

$$B_o = \begin{bmatrix} 435.28 & 0.4712 \\ 0 & -6.738 \end{bmatrix} \quad (8.8)$$

The objective is to derive model reference adaptive control law to achieve asymptotic tracking of speed and heading angles in the presence of parametric uncertainties:

$$e(t) = y(t) - y_m(t) \rightarrow 0 \text{ as } t \rightarrow \infty \quad (8.9)$$

where  $y_m = (v_m(s), \phi_m(s)) \in \mathfrak{R}^2$  are the reference speed and heading angle trajectories

of the reference model given by:

$$y_m(s) = W_m(s)r \quad (8.10)$$

where  $r \in \mathfrak{R}^2$  is the reference command. Since Eq.8.1 has relative degree 2, the reference model transfer function is chosen as:

$$W_m(s) = \text{diag}\left\{\frac{1}{(s+a_1)(s+\lambda)}, \frac{1}{(s+a_2)(s+\lambda)}\right\} \quad (8.11)$$

with  $a_1 = a_2 > 0$  and  $\lambda > 0$ . Thus,  $W_m(s)$  is a stable transfer function matrix. It should be noted that controller is synthesized using the output vector  $y(t)$  without the knowledge of the gain matrix.

## 8.2 Gain factorization

To derive the control law, first factorization of infinite gain matrix  $B_o$  is performed. First the unique LDU decomposition is performed followed by SDU decomposition. A positive diagonal matrix  $D^+$  is introduced as a free parameter.

### 8.2.1 LDU decomposition

The LDU decomposition of high frequency gain matrix  $B_o$  is written as[70]:

$$B_o = \begin{bmatrix} 1 & 0 \\ l_o & 1 \end{bmatrix} \begin{bmatrix} \Delta_1 & 0 \\ 0 & (\frac{\Delta_2}{\Delta_1}) \end{bmatrix} \begin{bmatrix} 1 & l_u \\ 0 & 1 \end{bmatrix} \quad (8.12)$$

where  $L_1$  is a unit lower and  $U_1$  is a unit upper triangular matrix, and  $D_1$  is a diagonal matrix. For the vehicle dynamic model given by Eqn.8.1, leading principle minors  $\Delta_1$  and  $\Delta_2$  of  $B_o$  are nonzero and the LDU decomposition exists. Let  $b_{ij}$ ,  $i, j = 1, 2$  be the elements of  $B_o$ . Solving Eqn.8.12, we get

$$\begin{aligned} l_o &= b_{21}/\Delta_1 \\ l_u &= b_{12}/\Delta_1 \end{aligned} \tag{8.13}$$

where  $\Delta_1 = b_{11}$ .

### 8.2.2 SDU decomposition

Factorizing  $D_1$  as  $D_1 = D + D_s$ , the SDU decomposition of the  $B_o$  can be written as

$$B_o = SD_sU_s \tag{8.14}$$

where  $S$  is symmetric positive definite,  $D_s$  is diagonal, and  $U_s$  is unit upper triangular matrix. The matrices  $S$  and  $U_s$  are selected as

$$\begin{aligned} S &= L_1 D^+ L_1^T \\ U_s &= D_s^{-1} (L_1^{-1})^T D_s U_1 \end{aligned} \tag{8.15}$$

It should be noted that factorization  $B_o = SD_sU_s$  is not unique because the positive diagonal matrix  $D_+$  is a free parameter. The unit upper triangular matrix has the

form

$$U = \begin{bmatrix} 1 & u_s \\ 0 & 1 \end{bmatrix} \quad (8.16)$$

We assume that the matrix  $S$  and the elements  $u_s$  are unknown. Derivation of the control law is based on the assumption that the sign of leading principle minors of  $B_o$  are unknown[45]. However, signs of  $\Delta_i$  can be obtained using the system matrices given by the Eqn.8.1.

### 8.3 Adaptive control law

The adaptive control law is derived following the approach presented in [45, 68]. First consider the existence of a control law  $u^*$  for matching closed loop transfer function,  $G(s)$ , and  $W_M(s)$ , when all the system parameters are known. That is,

$$y = G(s)u^* = W_M(s)r = y_m \quad (8.17)$$

Using [45, 68, 71], there exists a control law of the form

$$u^* = \theta_1^*\omega_1 + \theta_2^*\omega_2 + \theta_3^*y + \theta_4^*r = \theta^{*T}\omega \quad (8.18)$$

where

$$\begin{aligned}
\theta^* &= [\theta_1^* \ \theta_2^* \ \theta_3^* \ \theta_4^*] \in \mathfrak{R}^{2 \times 16} \\
\omega &= [\omega_1^T \ \omega_2^T \ y^T \ r^T] \in \mathfrak{R}^{16 \times 1} \\
\theta_1^*, \ \theta_2^* &\in \mathfrak{R}^{6 \times 2} \\
\theta_3^* &\in \mathfrak{R}^{2 \times 2} \\
\theta_4^* &= B_o^T \tag{8.19} \\
\omega_1 &= \frac{A(s)}{\Lambda(s)} u \in \mathfrak{R}^{6 \times 1} \\
\omega_2 &= \frac{A(s)}{\lambda(s)} y \in \mathfrak{R}^{6 \times 1} \\
A(s) &= [I \ Is \ Is^2]^T \in \mathfrak{R}^{2 \times 2} \\
\Lambda(s) &= \lambda_0 + \lambda_1(s) + \lambda_2 s^2 + \lambda_3 s^3
\end{aligned}$$

For the choice of  $\lambda_i > 0$ ,  $\Lambda(s)$  is a Hurwitz polynomial. The signals  $\omega_1$  and  $\omega_2$  are obtained by filtering the input and output. The matched closed-loop equation is obtained by setting  $u = u^*$ . Using equations 8.17 and 8.19, Eqn. 8.18 can be expressed as

$$u^* = \theta_1^{*T} \frac{A(s)}{\Lambda(s)} u^* + \theta_2^{*T} \frac{A(s)}{\Lambda(s)} G(s) u^* + \theta_3^{*T} G(s) u^* + \theta_4^{*T} W_M^{-1} G(s) u^* \tag{8.20}$$

Rearranging the terms in the above equation, matching equation is expressed as

$$I - \theta_1^{*T} \frac{A(s)}{\Lambda(s)} - \theta_2^{*T} \frac{A(s)}{\Lambda(s)} G(s) - \theta_3^{*T} G(s) = \theta_4^{*T} W_M^{-1} G(s) \tag{8.21}$$



Right multiplying the above equation by  $u$  we get

$$u = \theta^{*T}\omega - B_o^{-1}r + B_o^{-1}W_M^{-1}(s)G(s)u \quad (8.22)$$

Multiplying the above equation by  $W_M(s)B_o$  and rearranging the terms, the output tracking error equation is expressed as

$$e = W_M(s)B_o[u - \theta^{*T}\omega] \quad (8.23)$$

For the adaptive controller design, the  $SDU$  decomposition of  $B_o = SD_sU_s$  is substituted in the above equation and the resulting tracking error equation is expressed as

$$e = W_M(s)SD_sU_s[u - \theta^{*T}\omega] \quad (8.24)$$

Noting that  $U_s$  is upper triangular matrix, one has

$$U_s u_c = u_c - (I - U_s)u = u + \begin{pmatrix} u_s u_2 \\ 0 \end{pmatrix} \quad (8.25)$$

where,  $u_2$  is the second element of control input vector. Substituting Eqn. 8.25 in Eqn.8.24 we get

$$e = W_M(s)SD_s [u - U_s\theta^{*T}\omega + (u_s u_2, 0)^T] \quad (8.26)$$

Define

$$U_s \theta^{*T} \omega - (u_s u, 0)^T = \begin{bmatrix} (\omega, u_2) [(\theta_{(1)}^{*T} \theta_{(2)}^{*T} u_s) - u_{s1}]^T \\ \omega^T \theta_{(2)}^* \end{bmatrix} \triangleq \Omega^T \Theta^* \quad (8.27)$$

where,  $\Theta_i^T$  is the  $i_{th}$  row of  $\Theta^{*T}$  and

$$\begin{aligned} \Omega^T &= \text{diag}(\Omega_1^T, \Omega_2^T) = \text{diag} \{(\omega, u_2), \omega\}, \\ \Omega_1^T &\in \mathfrak{R}^{1 \times 17}, \quad \Omega_2^T \in \mathfrak{R}^{1 \times 16}, \\ \Theta^* &= \begin{bmatrix} \Theta_1^* \\ \Theta_2^* \end{bmatrix} = \begin{bmatrix} (\theta_{(1)}^{*T} + \theta_{(2)}^{*T} u_s - u_s)^T \\ \theta_{(2)}^{*T} \end{bmatrix} \\ \Theta_1^* &\in \mathfrak{R}^{1 \times 17}, \quad \Theta_2^* \in \mathfrak{R}^{1 \times 16} \end{aligned} \quad (8.28)$$

Using Eqn.8.27, Eqn.8.26 is expressed as

$$e = W_M(s) S D_s (u - \Omega^{*T} \Theta^*) \quad (8.29)$$

If the parameters are known, control law  $u = \Omega^{*T} \Theta^*$  can be chosen for trajectory control. In the following, a modification of this control law is considered to obtain an adaptive law.

First we introduce filtered signals

$$\zeta = L^{-1}(s) u \quad (8.30)$$

and

$$\begin{aligned}\xi &= \text{diag}\{\xi_1^T, \xi_2^T\} = L^{-1}(s)\Omega^T \\ &= \text{diag}\{L^{-1}(s)\Omega_1^T, L^{-1}(s)\Omega_2^T\}\end{aligned}\tag{8.31}$$

Where  $L(s) = s + \lambda, \lambda > 0$ . Note that for this choice of  $L(s)$ ,  $WM(s)L(s)$  is strictly positive real (SPR) transfer function. The error Eqn. 8.29 can be expressed as

$$\begin{aligned}e &= W_M(s)L(s)SD_sL^{-1}(s)[u - \Omega^T\Theta^*] \\ &= W_M(s)L(s)SD_s[\zeta - \xi^T\Theta^*]\end{aligned}\tag{8.32}$$

In view of 8.31, we select  $\zeta$  as

$$\zeta = \xi^T\Theta\tag{8.33}$$

where  $\Theta$  is an estimate of  $\Theta^*$ . Using equations 8.30 and 8.33, the control input is given by

$$\begin{aligned}u &= L(s)\zeta = (s + \lambda)[\xi^T\Theta] \\ &= \dot{\xi}^T\Theta + \lambda\xi^T\Theta + \xi^T\dot{\Theta} = \Omega^T\Theta + \xi^T\dot{\Theta}\end{aligned}\tag{8.34}$$

Substituting Eqn. 8.33 in 8.32 gives the error equation

$$e = W_M(s)L(s)SD_s\xi^T\tilde{\Theta}\tag{8.35}$$

where  $\tilde{\Theta} = \Theta - \Theta^*$  is parameter estimation error vector.

According to [68], there always exists a choice of  $D_+$  such that  $W_m(s)L(s)S$  is

SPR. Now, consider a realization of  $Wm(s)L(s)S$  of the form

$$\begin{aligned}\dot{x}_a &= A_a x_a + B_a D_s \xi^T \tilde{\Theta}, \\ e &= C_a x_a\end{aligned}\tag{8.36}$$

Since  $W_M(s)L(s)S$  is SPR, there exist matrices  $P_a > 0$  and  $Q_a > 0$  satisfying

$$\begin{aligned}A_a^T P_a + P_a A_a &= -Q_a \\ P_a B_a &= C_a^T\end{aligned}\tag{8.37}$$

For proof of stability consider a Lyapunov function

$$V = x_a^T P_a x_a + \tilde{\Theta}^T D_a \Gamma^{-1} \tilde{\Theta}\tag{8.38}$$

where  $T = \text{diag}(\Gamma_1, \Gamma_2)$ ,  $D_a = \text{diag}(|d_{s1}| I_{9 \times 9}, |d_{s2}| I_{8 \times 8})$ ,  $d_{si}$  are the diagonal elements of  $D_s$  and  $\Gamma_i > 0$ . Taking the derivative  $\dot{V}$  along the solution of Eqn. 8.36 and using Eqn. 8.37 gives

$$\begin{aligned}\dot{V} &= -x_a^T P_a x_a + 2x_a^T P_a [B_a D_s \xi^T \tilde{\Theta}] + \dot{\tilde{\Theta}}^T D_a \Gamma^{-1} \tilde{\Theta} \\ &= -x_a^T P_a x_a + 2 \sum [e_i d_{si} \xi_i^T \tilde{\Theta}_i + \dot{\tilde{\Theta}}_i^T |d_{si}| \Gamma_i^{-1} \tilde{\Theta}_i]\end{aligned}\tag{8.39}$$

where,  $e = (e_1, e_2)^T$ . In order to eliminate the unknown functions in Eqn.8.38, we choose the adaptive law as

$$\dot{\tilde{\Theta}}_i(t) = \tilde{\Theta}_i(t) = -\text{sgn}(d_{si}) \Gamma_i \xi_i e_i, i = 1, 2\tag{8.40}$$

Substituting Eqn.8.40 in Eqn.8.39 gives

$$\dot{V} = -x_a^T Q_a x_a \leq 0 \quad (8.41)$$

Since  $\dot{V} \leq 0$ , one has  $x_a, \Theta, e \in L_\infty$  (the set of bounded functions) and  $x_a, e \in L^2$  (the set of square integrable functions). Furthermore, following the arguments of [68, 71], it can be shown that all the signals in the closed loop system are bounded and  $e \rightarrow 0$  as  $t \rightarrow \infty$ . This completes the design of the adaptive law

#### 8.4 Simulation results

Simulations are conducted to verify the performance of the designed MRAC controller. It is assumed that the parameters of the system are completely unknown. The design parameters and adaptation gains are selected as

$$\begin{aligned} \Gamma_1 &= \gamma_1 I_{17 \times 17}, \Gamma_2 = \gamma_2 I_{16 \times 16} \\ \gamma_1 &= 1, \gamma_2 = 0.5 \end{aligned} \quad (8.42)$$

The closed loop system 8.1 and 8.34 with adaptive law 8.40 is simulated. The initial condition for the parameter estimates are arbitrarily set to zero; that is,  $\Theta(0)$  is a null vector. This is rather worst choice of initial estimates of the unknown parameters; but it is made to demonstrate the robustness of the designed control system. From Fig. 8.1 it is apparent that smooth trajectory control of speed and heading angle without any overshoot is achieved. Except for the transient portion, tracking error is

close to zero after 2sec. At  $t = 20\text{sec}$ , reference heading angle trajectory changes from 0 to 10 degree. However, using MRAC there is no influence of change in heading angle trajectory on tracking speed of the vehicle in contrast to open loop response shown in Fig. 6.5.

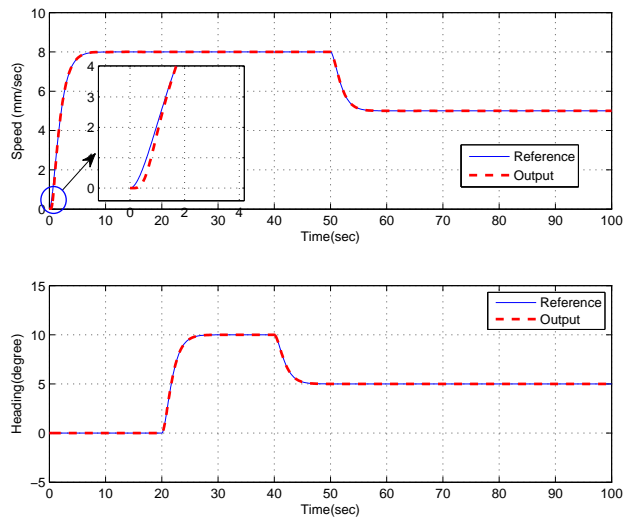


Figure 8.1: Model reference adaptive control speed (mm/sec) and heading angle (degree)

Figure 8.2 shows the control input amplitude ( $v$ ) and bias ( $v$ ) applied to the IPMC actuator. Except for the transient portion, amplitude of the sinusoidal voltage is small enough to not to damage the IPMC actuator. Figure 8.3 shows the variation in the norm of the estimated parameter vector  $\Theta$  with time. Eventually these estimates converge to some constant value, which differ from the actual valued. This is not surprising because these estimates can not converge to their true values unless certain

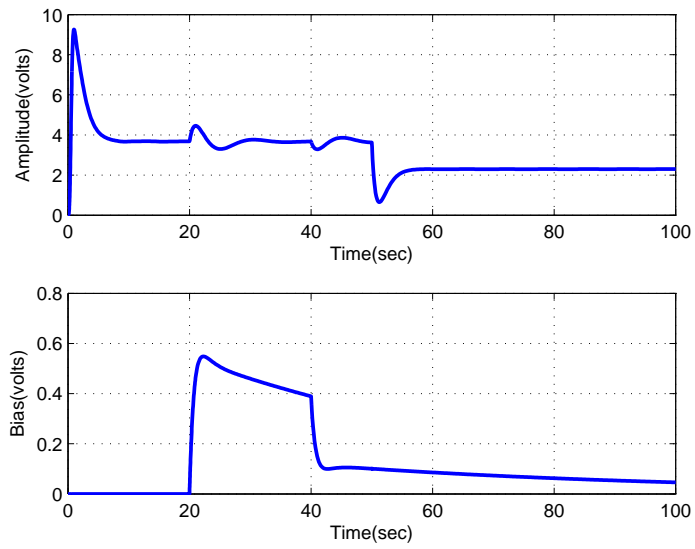


Figure 8.2: Control input amplitude (v) and bias (v)

persistent excitation condition is satisfied [71].

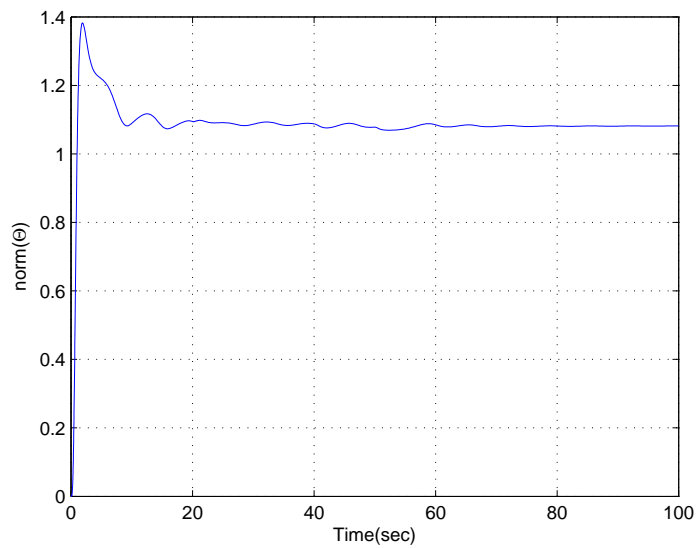


Figure 8.3: Estimated parameter norm  $\|\Theta\|$

## 8.5 Summary

In this chapter, a model reference adaptive control (MRAC) system is designed for the speed and heading control of IPMC driven vehicle. It was assumed that the system parameters as well as the high frequency gain matrix were not known. Furthermore, only the speed and heading were measured for the synthesis of the control law. For singularity free design, the SDU decomposition of the gain matrix was used. Based on the Lyapunov analysis, it was shown that in the closed loop system including the adaptive law, the speed and heading angle trajectories asymptotically converge to the reference trajectories. Numerical simulations have been presented which show that in the closed loop system, the adaptive law can accomplish precise trajectory control even in the presence of large uncertainties in the parameters.



## CHAPTER 9

### CONCLUSIONS

In this work, modeling and development of the (Ionic Polymer Metal Composite) IPMC propelled vehicle is considered. IPMC is a class of Electro-Active Polymer (EAP), and consists of a polymer membrane sandwiched between two metallic electrodes, typically made up of platinum (Pt) or Gold (Au). Due to transport of ions, IPMC undergoes a large deformation when an external voltage is applied. The advantage of these materials compared to other EAP materials is that they can be operated in a hydrated environment. Therefore, it is used as propulsor in developing small scale underwater vehicles. The complete details of the IPMC actuator including the chemical structure and the actuation principle discussed in chapter 2. Clumped RC model relating the applied voltage to the moment generated is given in this chapter. IPMC undergoes large deformation for relatively small applied voltages. In chapter 3, large deflection bending of the IPMC actuator is modeled using finite element method and energy formulation. Local coordinate frame formulation is used to accurately describe the bending of the IPMC actuator. The electrical constants used in the model are identified using the experimental data. Experiments are conducted to measure the deflection of the IPMC validate the proposed large deflection bending model.

In chapter 4, hydrodynamic model is developed for the IPMC actuated under-

water vehicle. Frictional forces due to the interaction with water are considered in modeling. Constants pertaining to tangential, form force and drag force acting on the head are identified using CFD studies and further verified using experimental data and available literature. A miniature underwater vehicle is developed using IPMC actuator and experiments are conducted to validate the hydrodynamic model. An autonomous IPMC driven vehicle is developed using on-board power supply and electronics. Wireless control of the vehicle is achieved using Xbee wireless communication modules.

A feedback control algorithm is developed in chapter 5 to control speed and yaw(orientation) of the vehicle. Simulation data is used for identifying the relation between input and output variables. Controller gains are identified using trail and error process. A more systematic approach is followed in chapter 6, where a decoupling control algorithm is designed for tracking speed and orientation of the vehicle. Control inputs are amplitude and bias of the voltage applied to IPMC actuator. Using the MATLAB system identification toolbox, a transfer function matrix is identified to relate inputs and outputs. Controller transfer functions are identified using the desired closed-loop transfer function matrix. The developed controller is successfully implemented on non-linear plant. An experimental setup for validating the controller is proposed.

In chapter 7, an algorithm for path planning of the IPMC propelled vehicle in the presence of the obstacles is proposed. Obstacles are assumed to of polygonal shape that approximate their actual dimension. To simplify the path planning approach,

vehicle is shrunk to a line and simultaneously expanding the obstacles. The path obtained by path planning algorithm is discretized with respect to time to generate reference speed and yaw angles. Feedback controller developed in chapter 5 is used for tracking the speed and orientation obtained from path planning algorithm.

## BIBLIOGRAPHY

- [1] Pugal, D., Kruusmaa, K. K. M., and Aabloo, A., 2008. “An advanced finite element model of the ipmc”. *Proceedings of SPIE - The International Society for Optical Engineering*, **6927**.
- [2] Yim, W., Renno, J., and Lee, J. “Dynamic modeling of segmented ionic polymer metal composite (ipmc) actuator”. *International Cont. on Intelligent Robots and Systems*.
- [3] Kanno, R., Kurata, A., Hattori, M., Tadokoro, S., Takamori, T., and Oguro, K., 1994. “Characteristics and modeling of icpf actuator”. *Proceedings of the Japan-USA Symposium on Flexible Automation*, **2**, pp. 691–698.
- [4] Kanno, R., Tadokoro, S., Takamori, T., and Hattori, M., 1996. “Linear approximate dynamic model of icpf actuator”. *Proceedings of the IEEE International Conference on Robotics and Automation*, pp. 219–225.
- [5] K.Newbury, and D.Leo, 2002. “Electromechanical modeling and characterization of ionic polymer benders”. *Journal of Intelligent Materials Systems and Structures*, **13**(1), pp. 51–60.
- [6] Nemat-Nasser, S., and Jiang, Y., 2000. “Electromechanical response of ionic polymer metal composites”. *Journal of Applied Physics*, **87**(7), pp. 3321–3329.

- [7] Gennes, P. D., Okumura, K., Shahinpoor, M., and Kim, K., 2000. “Mechano-electric effects in ionic gels”. *EUROPHYSICS LETTERS*, **40**, pp. 513–518.
- [8] Ogura, K., Asaka, K., Fujiwara, Nonishi, K., and Sewa, S., 2000. “Polymer electrolyte actuator driven by low voltage”. *Proceedings of Materials Research Society Symposium*, **600**, pp. 229–235.
- [9] Nemat-Nasser, S., 2002. “Micro-mechanics of actuation of ionic polymer-metal composites (ipmcs)”. *Journal of Applied Physics*, **92**(5), pp. 2899–2915.
- [10] Tadokoro, S., Yamagami, S., Takamori, T., and Oguro, K., 2000. “Modeling of nafion-pt composite actuators (icpf) by ionic motion”. *Proceedings of SPIE*, **3987**, pp. 92–102.
- [11] Parquette, J., Nam, J., and Young, S., 2003. “An equivalent circuit model for ionic polymer metal composite and their performance improvement by a clay-based polymer nano composite technique”. *J. Intell. Mater. Syst. Struct.*, **14**, pp. 633–642.
- [12] Yagasaki, K., and Tamagawa, H., 2004. “Experimental estimate of viscoelastic properties for ionic-polymer-metal composites”. *Phys. Rev*, **70**(052801).
- [13] Mart, A., Alvo, A., Andres, P., and Kruusmaa, M., 2008. “A mechanical model of a non-uniform ionomeric polymer- metal composite actuator”. *Smart Mater. Struct*, **17**(025004).

- [14] Punning, A., Johanson, U., Anton, M., and Kruusmaa, M., 2008. “A distributed model of ipmc”. *Proceedings of SPIE*, **6927**.
- [15] Z, C., and X, T., 2008. “A control-oriented physics based model for ionic polymer metal composite actuators”. *IEEE/ASME Trans. Mechatronics*, **13**, pp. 519–529.
- [16] Brunetto, P., Fortuna, L., Graziani, S., and Strazzeri, S., 2008. “A model of ionomeric polymer- metal composite in under water operations”. *Smart Mater. Struct*, **17**(025029).
- [17] Lee, S., Park, H., and Kim, K., 2005. “A model of ionomeric polymer- metal composite in under water operations”. *Smart Mater. Struct*, **14**, pp. 1363–1368.
- [18] Toi, Y., and Kang, S., 2005. “Finite element analysis of two-dimensional electrochemical-mechanical response of conducting polymer-metal composite beams”. *Comput. Struct*, **83**, pp. 2573–2583.
- [19] Pugal, D., J, K. K. J. K., Kruusmaa, M., and Aabloo, A., 2007. “Finite element simulations of the bending of the ipmc sheet”. *Proceedings of SPIE - The International Society for Optical Engineering*, **6524**.
- [20] Nguyen, T., Goo, N., Nguyen, V., Yoo, Y., and Park, S., 2008. “Design, fabrication, and experimental characterization of a flap valve ipmc micropump with a flexibly supported diaphragm”. *Sensors Actuators*, **141**, pp. 640–648.

- [21] Triantafyllou, M. S., Techet, A. H., and Hover, F. S., 2004. “Review of experimental work in biomimetic foils”. *IEEE Journal of Oceanic Engineering*, **29**(3), pp. 585–594.
- [22] Bandyopadhyay, P. R., 2005. “Review of experimental work in biomimetic foils”. *IEEE Journal of Oceanic Engineering*, **30**(1), pp. 109–139.
- [23] Sfakiotakis, M., Lane, D. M., and Davies, J. B. C., 1999. “Review of fish swimming modes for aquatic locomotion”. *IEEE Journal of Oceanic Engineering*, **24**(2), pp. 237–252.
- [24] Lighthill, M. J., 1960. “Note on the swimming of slender fish”. *Journal of Fluid Mechanics*, **9**(2), pp. 305–317.
- [25] Wu, T. Y., 1961. “Swimming of a waving plate”. *Journal of Fluid Mechanics*, **10**(3), pp. 321–344.
- [26] Harper, K. A., Berkemeier, M. D., and Grace, S., 1998. “Modeling the dynamics of spring-driven oscillating-foil propulsion”. *IEEE Journal of Oceanic Engineering*, **23**(3), pp. 285–296.
- [27] Mason, R. J., and Burdick, J. W., 2000. “Experiments in carangiform robotic fish locomotion”. *IEEE Int. Conf. on Robotics and Automation*, pp. 428–435.
- [28] Kelly, S. D., Mason, R. J., Anhalt, C. T., Murray, R. M., and Burdick, J. W., 1998. “Modelling and experimental investigation of carangiform locomotion for control”. *Proc. American Control Conference*, pp. 1271–1276.

- [29] Saimek, S., and Li, P. Y., 2001. “Modelling and experimental investigation of carangiform locomotion for control”. *Proc. American Control Conf.*, pp. 125–130.
- [30] Yim, W., Kim, K., J.Paquette, and Kim, D., 2005. “Operation of ionic polymer metal composite in water”. *Proceedings of SPIE - The International Society for Optical Engineering*, **5759**, pp. 22–23.
- [31] Paquette, J., and Kim, J., 2004. “Ionomeric electroactive polymer artificial muscle for naval applications”. *IEEE J. Oceanic Engineering*, **29**(3), pp. 729–737.
- [32] Nakabo, Y., T.Mukai, and Asaka, K., 2004. “A multi-dof robot manipulator with a patterned artificial muscle”. *The 2nd Conf. on Artificial Muscle (Asaka)*.
- [33] Liu, J., Dukes, I., and Hu, H., 2005. “Novel mechatronics design for a robotic fish”. *IEEE/RSJ International Conference on Intelligent Robots and Systems*, pp. 2077–2082.
- [34] Triantafyllou, M., and Triantafyllou, G., 1995. “An efficient swimming machine”. *Scientific American*, **272**, p. 64.
- [35] Leonard, N., and Graver, J. “Model-based feedback control of autonomous underwater gliders”. *IEEE Journal of Oceanic Engineering*, **26**(4).
- [36] Fukuda, T., A.Kawamoto, Arai, F., and H.Matsuma, 1995. “Steering mechanism of underwater micro mobile robot”. *IEEE Conference on Robotics and Automation*, pp. 363–368.



- [37] Zhang, W., Guo, S., and Asaka, K., 2006. “A new type of hybrid fish-like microrobot”. *International Journal of Automation and Computing*, **4**, pp. 358–365.
- [38] Domenici, P., and Blake, W., 1997. “The kinematics and performance of fish fast-start swimming”. *The Journal of Experimental Biology*, **200**, pp. 1165–1178.
- [39] Shin, D., Na, S., Kim, J., and Baek, S., 2008. “Fuzzy neural networks for obstacle pattern recognition and collision avoidance of fish robots”. *Soft Computing*, **12**, pp. 715–720.
- [40] Chao, Z., Zhiqiang, C., Shuo, W., Xiang, D., and Min, T., 2008. “A miniature biomimetic robotic fish and its realtime path planning”. *Field and Service Robots*, **42**, pp. 147–156.
- [41] Yu, J., Liu, L., Wang, L., Tan, M., and Xu, D., 2008. “Turning control of a multilink biomimetic robotic fish”. *IEEE Transactions on Robotics*, **24**, pp. 201–206.
- [42] Yu, J., Wang, L., Tan, M., and Li, Y., 2009. “Step function based turning maneuvers in biomimetic robotic fish”. *IEEE International Conference on Robotics and Automation*, pp. 3432–34366.
- [43] Brijesh, C., Marco, P., and Mahadevan, A. “Adaptive intelligent control of ionic polymer metal composites”. *Smart. Mater. Struct.*, **14**.

- [44] Brufau-Penella J, Tsiakmakis K, L. T., and Vidal M., P., 2008. “Model reference adaptive control of ionic polymer metal composite in underwater application”. *Smart Mater. Struct.*, **17**(045020).
- [45] Nambisan, P. R., and Singh, S. N., 2009. “Adaptive output feedback control of mimo auv with unknown gain matrix”. *Systems Science*, **35**(2).
- [46] Shahinpoor, M., Bar-Cohen, Y., Simpson, J., and Smith, J., 1998. “Ionic polymer-metal composites (ipmcs) as biomimetic sensors, actuators and artificial muscles - a review”. *Smart Mater. Struct.*, **7**(6), pp. 15–30.
- [47] Bao, X., Bar-Cohen, Y., and Lih, S., 2002. “Measurements and macro models of ionomeric metal composites (ipmc)”. *Proceedings of SPIE*, **5062**(1), pp. 220–227.
- [48] Yim, W., Praquette, J., Heo, S., and Kim, J., 2005. “Characterization of the electromechanical properties of eap materials”. *Proceedings of SPIE - The International Society for Optical Engineering*, **5062**(1), pp. 297–304.
- [49] Logan, D. L. “A first course in the finite element method using algor”. *PES Publications*.
- [50] Paola, B., Luigi, F., Salvatore, G., and Salvatore, S. “A model of ionic polymer metal composite in underwater operations”. *Smart Mater. Struct.*, **17**(025029).
- [51] Wunderlich, W., and Pilkey, W., 2003. *Mechanics of Structures: Variational and Computational Methods*. CRC Press.
- [52] <http://www.mathworks.com/access/helpdesk/help/toolbox/ident>.

- [53] <http://www.matweb.com/>.
- [54] Kambe, T., 1978. “The dynamics of carangiform swimming motions”. *J. Fluid Mech*, **87**(3), pp. 533–560.
- [55] Gursel, A., Geoffrey, S., Nam, N., Laleh, S., and Rick, M. “Establishment of a bio-mimetic device based on tri-layer polymer actuators-propulsion fins”. *J. Bioinspi. Biomim*, **2**.
- [56] Earnest, M., Zheng, C., Stephen, S., and Xiaobo, T. “Modeling of bio-mimetic robotic fish propelled by an ionic polymer metal composite actuator”. *IEEE International Conf. on Robotics and Automation*.
- [57] FLUENT 6.3.26, Ansys Inc 2007.
- [58] Alexander, D. E. “Drag coefficients of swimming animals: Effect of using different reference areas”. *Biol. Bull*, **179**.
- [59] Patric, J. F., 2004. “Unsteady Navier-Stokes simulation of Rainbow trout trout swimming Hydrodynamics”. MS Thesis, Washington State University, Seattle, WA.
- [60] GAMBIT 2.4.6, Ansys Inc 2007.
- [61] <http://courses.cit.cornell.edu/fluent/>.

- [62] Kunihico, T., William, B. D., Tim, C., Micheal, H. D., and Clarence, W. R. “Unsteadiness in flow over a flat plate at angle of attack at low Reynolds numbers”. *AIAA Aerospace Scientist Meeting and Exhibit*.
- [63] Gutta, S. K., Trabia, M. B., and Yim, W. “Modeling dynamics of ionic polymer metal composite (ipmc) actuator dynamics using large deflection beam model”. *International Mechanical Engineering Congress and Exposition*.
- [64] <http://www.pololu.com/catalog/category/8>.
- [65] Bollinger, J. G., and Duffie, N. A., 1988. *Computer Control of Machines and Processes*. Addison-Wesley, Reading, MA.
- [66] Li, J., and Trabia, M., 1996. “Adaptive path planning and obstacle avoidance for a robot with a large degree of redundancy”. *Journal of Robotic Systems*, pp. 163–176.
- [67] Trabia, M., 1993. “Planning near minimum-collision-free paths for robots”. *IEEE Transactions on Systems, Man, and Cybernetics*, pp. 1481–1488.
- [68] A. K. Imai, R. R. Costa, L. H., and G. Tao, 2007. “Multivariable adaptive control using high frequency gain matrix factorization”. *IEEE Transactions on Automatic Control*, **52**, pp. 1152–1156.
- [69] R. R. Costa, L. Hsu, A. K. I., and Kokotovic, P., 2003. “Lyapunov-based adaptive control of mimo systems”. *Automatica*, **30**, pp. 1251–1257.

- [70] Tao, G., ed., 2003. *Adaptive Control Design and Analysis*. Wiley-IEEE Press.  
ch. 5, p. 239.
- [71] K.S. Narendra, A. M. A., ed., 1989. *Stable adaptive systems*. Prentice-Hall, Inc.

## VITA

Graduate College  
University of Nevada, Las Vegas

Shivakanth Gutta

### Home Address:

2 Honeysuckle Lane  
Ridgefield, Connecticut 06877

### Degrees:

Bachelor of Technology, 2002  
Kakatiya University, Warangal, India

Master of Science, 2004  
Osmania University, Hyderabad, India

### Publications:

S. Gutta, W. Yim and S. N. Singh, "Adaptive output feedback control of the IPMC propelled vehicle with unknown high frequency gain matrix" SMASIS 2011, Phoenix, AZ.

S. Gutta, W. Yim, and M. Trabia, "Path planning and control for underwater vehicle driven by IPMC actuator," IMECE 2010, Vancouver, CA.

J. Lee, S. Gutta, W. Yim and K. Kim, "Preliminary Study of Wireless Actuation and Control of IPMC Actuator," IEEE/ASME International Conference on Advanced Intelligent Mechatronics, July 2010.

S. Gutta, M. Trabia, and W. Yim, "Modeling dynamics of ionic-polymer metal composites actuator using large deflection beam model," Journal of Smart Materials and Structures, Volume 18, 2009, pp. 1-9.

S. Gutta and S. N. Singh, "Output feedback control of smart projectile fin based on internal model principle," ASME Early Career Technical Journal, 2009

S. Gutta, W. Yim and M. Trabia, "Yaw angle and speed control of underwater vehicle propelled by IPMC actuator," ASME SMASIS 2009, Oxnard, California.

S. Gutta, S. Singh and W. Yim, "Feedback control of smart projectile fin based on internal model principle," ASME ECTC 2009, Tuscaloosa, Alabama.

S. Gutta, W. Yim and M. Trabia, "Modeling dynamics of underwater vehicles actuated by ionic polymer metal composite actuators," SPIE Smart Structures and Ma-

materials and Nondestructive Evaluation and Health Monitoring, Mar. 8-12, 2009, San Diego, California

S. Gutta, M. Trabia and W. Yim, "Modeling dynamics of ionic polymer metal composite using large deflection beam model," ASME International Mechanical Engineering Congress and Exposition, Nov. 11-15, 2007, Seattle, Washington.

J. Lee, S. Gutta and W. Yim, "Open-loop control of ionic polymer metal composite (IPMC) based underwater actuator using a network of neural oscillator," Proceedings of 2007 IEEE International Conference on Robotics and Systems (IROS), WeC3.1, Oct. 29-Nov. 2, 2007, San Diego, CA., USA.

Dissertation Title: Modeling and Control of a Flexible Ionic Polymer Metal Composite(IPMC) Actuator for Underwater Propulsion

Dissertation Examination Committee:

Chairperson, Dr. Woosoon Yim, Ph.D.

Committee Member, Dr. Mohamed B. Trabia, Ph.D.

Committee Member, Dr. Brenden O'Toole, Ph.D.

Committee Member, Dr. Yitung Chen, Ph.D.

Graduate Faculty Representative, Dr. Sahjendra N. Singh, Ph.D.

